Multiple Compartment Modelling and Estimation in Magnetic Resonance Imaging

Syeda Warda Taqdees

ORCID: 0000-0001-6294-622X

Submitted in total fulfilment of the requirements of the degree of Doctor of Philosophy

Department of Biomedical Engineering
The University of Melbourne

May 2018

Abstract

THE magnetic resonance (MR) signal encapsulates invaluable information about the structural and functional organization of an object of interest. In body imaging applications, parametric models of the MR signal are designed to infer tissue structure by performing parameter estimation. Given a signal model, a typical parameter estimation algorithm solves an optimization problem to identify model parameter values that best describe the measured MR signal. A commonly employed modelling technique, known as multicompartment modelling, compartmentalizes the tissue into two or more discrete compartments, describing the MR signal as a composite sum of the signals arising from each compartment. This thesis is concerned with the utility and limitations of multicompartment modelling in sodium and diffusion-weighted imaging.

The output of an analysis of MRI data is often spatial maps of parameter estimates, the result of having applied a model to the measured signal. Commonly employed bi-exponential models of T_2^*-weighted sodium data are susceptible to uncertainty in parameter estimates, resulting in noisy parameter maps with low contrast between brain tissue types. This thesis develops a continuum model of sodium T_2^*- decay, applied to in vivo human multi-echo 7T data, which leads to high quality, high contrast parameter maps. In diffusion-weighted imaging, two component models of diffusion-weighted signal decay have been advocated for use in the estimation of axon diameter distributions. This thesis demonstrates that axon diameters are not distinguishable under the commonly assumed short pulse approximation, even at high gradient strengths available on pre-clinical MRI systems. Instead, the long pulse regime theoretically provides a stronger diffusion weighting under which axon diameters are maximally separated, as are the hindered and restricted diffusion compartments. Through experimental MRI, it is shown that even under long gradient pulses, a simplistic two-compartment model is incapable of capturing experimental decay behaviour, calling into question the utility of these models for axon diameter density estimation.

Prior to performing parameter estimation, it is desirable to improve the quality of the MR signal, either by increasing the signal strength or reducing the noise level. Echo averaging is commonly employed for SNR improvement and contrast enhancement in multiecho MRI data. The number of echoes used in the averaging operation is an important factor in determining the overall SNR gain in the averaged image. This thesis studies the impact of the number of echoes on the averaging process and derives an analytical expression that predicts the optimum number of echoes for achieving maximum SNR gain. This technique is demonstrated to be applicable to the mono-exponential, bi-exponential and gamma distribution models of T_2-weighted MRI signal. Experimental results demonstrate the ability to predict the optimal echo averaging conditions, both globally or locally in a voxelwise procedure.

The assessment of the parameter estimation framework is a crucial step in determining the veracity of the resultant parameter estimates. The Cramer Rao lower bound (CRLB), a lower bound on the variance of parameter estimates, is frequently employed as a metric of precision and a method for experimental design. CRLB is valid only under the assumptions of model correctness and has the potential to provide misleading estimates of parameter precision when such assumptions are not met. This thesis exposes the limitations of CRLB analyses of the MRI models, and instead, proposes the use of the observed Fisher Information (OFI) as an empirical metric of precision, which is not constrained by an assumption of model correctness. Further, the maximum likelihood (ML) value provides an empirical measure of accuracy. Hence, a joint ML-OFI analysis of the parameter estimates is proposed to provide a robust assessment of estimation performance, applied to the multicompartment models of diffusion as an example.

Declaration

This is to certify that

- the thesis comprises only my original work towards the PhD,
- due acknowledgement has been made in the text to all other material used,
- the thesis is fewer than 100,000 words in length, exclusive of tables, maps, bibliographies and appendices.

Warda Syeda

Date

Publications

The work presented in this thesis has produced the following publications and conference papers/ presentations.

Journal papers

- Syeda, W., Wright, D., Ng, A., and Johnston, L. A. Model comparison in Quantitative MRI: Application to ADC estimation. *In preparation for submission to Magn Reson Med.*
- Syeda, W., Blunck, Y., Ng, A., Cleary, J., and Johnston, L. A. A Continuum of T_2^* Components: Flexible Fast Fraction Mapping in Sodium MRI. *In preparation for submission to Magn Reson Med.*
- Syeda, W., Blunck, Y., Brodtmann, A., Cleary, J., and Johnston, L. A. SNR Improvement in Low Intensity MRI Images Through Optimized Multiple Echo Averaging. *In preparation for submission to Magn Reson Med.*

Refereed conference papers

- Syeda, W., Ng, A., Wright, D. K., Tolcos, M., and Johnston, L. A. (2017, April). Analysis of ADC model robustness in diffusion-weighted MRI. *IEEE 14th International Symposium on Biomedical Imaging* pp. 966-969. (Poster Presentation).
- Syeda, W., Moore, S. M., Wright, D. K., Tolcos, M., and Johnston, L. A. (2015, April). Limitations of two-component diffusion models for axon diameter density estimation. *IEEE 12th International Symposium on Biomedical Imaging* pp. 1176-1179. (Oral Presentation).

Conference Abstracts

- Syeda, W., Ng, A., Wright, D. K., and Johnston, L. A. (2017, December). Assessment of model fit in experimental MRI data: Application to ADC estimation. *The Australian and New Zealand Magnetic Resonance Society*, Gold Coast, Australia, 2017 (Oral Presentation)
- Syeda, W., Blunck, Y., Ng, A., Cleary, J., and Johnston, L. A. (2018, June). A Continuum of Components: Robust Parameter Mapping in Sodium MRI. *Joint Annual Meeting ISMRM-ESMRMB, Paris, France*, 2018 (Oral Presentation).

Acknowledgements

At the start of the PhD, I lost my mother after over a decade long battle with the chronic kidney disease. During this incredibly difficult time of my life, my wonderful supervisor Leigh Johnston not just guided me patiently in academic activities, but also helped me to stand back on my feet and see through my grief. For this, I am eternally grateful to her. I express my deepest gratitude for listening to my random ideas and guiding my thinking towards more realistic research scenarios, a gift I am sure will always help me in carving my future research paths. Special thanks goes to my co-supervisors, Amanda Ng for her helpful mathematical genius and Jon Cleary for supporting me in expanding the scope of my research to the other areas of MRI. I am indebted to my advisory committee, Peter Farrell, Bahaman Tayori, Mohammad Aldeen and Tony Burkitt for keeping my candidature on track with timely feedback.

Special thanks goes to my friends and colleagues from the Biomedical Engineering department, the Electrical and Electronic Engineering department and the Melbourne Brain Centre Imaging Unit: David Wright, Scott Kolbe, Yasmeen Blunck, James Korte, Ed Green, Asif Iqbal, Ali Qadar, Akhil Kottaram, Yasmeen George, Rui Li, Parvin Zarei, Yamni Mohan, Camille Shanahan, Sonal Josan, Sanuji Gajamange, Frederique Boonstra, Myrte Strik, Annie Shelton and Milad Faizollah. In particular, a massive thanks to Yasmin Blunck for being a wonderful friend, for always listening to my worries and troubles, and for cheerful discussions on our eccentric research aspirations. Also, to Ali and Asif for providing meaningful insights into my research. Special thanks to my colleagues at the Research Platforms: David Flanders, Nicole La Mela, Dejan Jotanovic, Kerry Halupka, Philippa Karoly, Ewan Nurse, Tim Rice, Nikki Rubinstein and Errol Lloyd.

To my friends, for making the tough times in research bearable and actually enjoyable. Suzan Maleki for endless encouragement and support, Michelle Pablo for a continuous supply of internet memes, Omera Shahnawaz for gossip, Maria Ayaz for joyful conversations, Ambreen Sharif for making sure I am well-fed during the thesis writing phase, and my *MCS kay Jhallay* Amna, Hamna, Aimon and Hunniya for believing in me.

To my husband and life partner, Najamuddin Sahito, for sacrificing his career and the last six years of his life to support me in fulfilling my dream of completing a doctorate, for loving and caring for me unconditionally, for instilling in me the passion to pursue my dreams and for celebrating my successes and bearing with me in the moments of distress. To my parents, Syed Saleem Raza and Naheed Saleem, for their countless sacrifices to ensure I receive quality education. To my siblings, Uzman, Faria, Hira and their families for always being there for me. Especially, heartfelt thanks to Hira and her husband Hesham Bhai for the constant supply of motivation. Last but not least, to my cats, Sydney and Caramel for endless cuddles during thesis writing and for making my life sweet and purrrrfect!

Contents

List of Figures

List of Tables

List of Abbreviations

^{1}H	Hydrogen
^{23}Na	Sodium
3D-MERINA	3D Multiecho Radial Imaing of ^{23}Na
ADC	Apparent Diffusion Coefficient
ADD	Axon Diameter Density
BE	Bi-exponential
BEM	Bi-exponential Mixture Model
BOLD	Blood Oxygen Level Dependent
cADC	Continuum of Apparent Diffusion Coefficients
CB-GM	Cerebral Gray Matter
CB-WM	Cerebral White Matter
CC	Corpus Callosum
CEST	Chemical Exchange Saturation Transfer imaging
CHARMED	Composite Hindered and Restricted Model of Diffusion
CNR	Contrast-to-Noise Ratio
CNS	Central Nervous System
CRLB	Cramer Rao Lower Bound
CSF	Cerebrospinal Fluid
CT	Computed Tomography
DK	Diffusion Kurtosis
DKI	Diffusion Kurtosis Imaging
DWI	Diffusion Weighed Imaging
DW-MRI	Diffusion-Weighted MRI
EFG	Electric Field Gradient
EPI	Echo Planar Imaging
FID	Free Induction Decay
FIM	Fisher Information Matrix
fMRI	Functional MRI

FOV	Field of View
GA	Gamma Model
GM	Gray Matter
LL	Log Likelihood
ME	Mono-exponential Model
MGE	Multi Gradient Echo
ML	Maximum Likelihood
MLE	Maximum Likelihood Estimation
MLOFI	Maximum Likelihood and Observed Fisher Information
MR	Magnetic Resonance
MRI	Magnetic Resonance Imaging
MS	Multiple Sclerosis
MSE	Mean Square Error
NMR	Nuclear Magnetic Resonance
OFI	Observed Fisher Information
OB	Olefactory Bulb
PGSE	Pulsed Gradient Spin Echo
QSM	Quantitative Susceptibility Mapping
RBM	Reflected Brownian Motion
ROI	Region of Interest
SGP	Short Gradient Pulse
SNR	Signal-to-Noise Ratio
SWI	Susceptibility Weighted Imaging
WM	White Matter

CHAPTER
ONE

Introduction

MAGNETIC resonance imaging (MRI) is a non-invasive imaging technique capable of providing highly detailed images without the use of ionizing radiations. Over the years, MRI has proven to be an invaluable tool for diagnostic and research applications. The ability of MRI in discerning soft tissue has led to its widespread utility in body imaging applications. MRI is routinely used for assessment, diagnosis and prognosis of a large number of diseases and pathologies such as cancer (Damadian, 1971; Fass, 2008), multiple sclerosis (MS) (Ceccarelli et al., 2012; Rovira et al., 2015), Alzheimer's disease (Jack et al., 2008; Frisoni et al., 2010; Greicius et al., 2004), cardiovascular disease (Lee et al., 2018), renal disease (Takahashi et al., 2015) and neurological disorders (Shenton et al., 2001). Unlike the signals of other commonly employed imaging modalities, such as x-ray and CT, the MRI signal arises from within the body, thus providing richer information about physical and chemical composition of soft tissue. MRI provides superior tissue contrast and can distinguish between water, fat, muscle and soft tissue structures. Advanced MRI-based techniques such as functional MRI and diffusion MRI are known to provide complementary information about the function and microscopic structure of the body.

A magnetic resonance (MR) signal is jointly characterized by the experimental parameters and the physical and chemical composition of the underlying tissue, as expressed in (Bloch, 1946). Through careful selection of experimental parameters, the NMR signal is sensitized to various contrast mechanisms, such as proton density weighting (Mansfield et al., 1976), longitudinal recovery based T_1-weighting, transverse relaxation based T_2-weighting (Lauterbur et al., 1973) or diffusion (Torrey, 1956). Mathematical modelling techniques are employed to relate the MR signal to the tissue. For MRI applications, a class of biophysical models jointly parametrizes tissue properties, experimental parameters and the noise characteristics of the received signal. The subject of this thesis is development, optimization and assessment of the multicompartment models of transverse relaxation and diffusion decay processes in tissue.

A model can be purely deterministic or statistical in nature or a mixture of both approaches, depending upon the assumptions made about the signal characteristics. MR models can further be classified into two main classes, non-parametric models (e.g. Andersson and Sotiropoulos, 2015; Sled et al., 1998; Song et al., 2007), and parametric (e.g. Levesque and Pike, 2009; Zheng and Xia, 2010; Weiskopf et al., 2013; Mosher and Dardzinski, 2004; Basser et al., 1994b; Wenjin et al., 2010; Komlosh et al., 2013; Stanisz et al., 1997; Behrens et al., 2003; Assaf et al., 2004, 2008; Zhang et al., 2011; Assaf and Basser, 2005), according to the dimensionality of the parameter space. A parametric model employs a finite number of parameters that capture all information about the signal of interest (Sheskin, 2003). We will be concerned only with the parametric models in this thesis. Given a set of values assumed by model parameters, $\boldsymbol{\theta}$, parametric MR models describe generative processes that give rise to an MR signal, denoted $\boldsymbol{x}(\boldsymbol{\theta})$ (Figure 1.1). The measured signal, $\boldsymbol{y}$, contains contributions from both the MR signal and the

measurement noise.

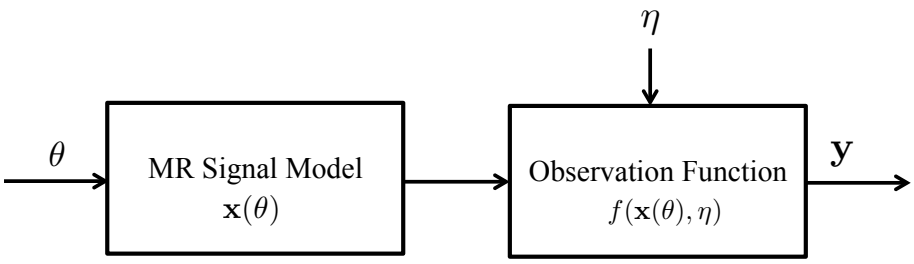

Figure 1.1: Conceptual diagram of a generative signal model.

A typical inference framework consists of two main components, a signal model and an estimation algorithm. Parameter estimation methods are inverse mathematical problems (Beck and Woodbury, 1998), i.e. a set of MR signal observations is used to relate the model parameters to the causal factors, such as the diffusion processes in tissue. Parameter mapping is desirable to gain useful insights into tissue organization and function. In order to produce robust parameter mapping, multiple reconstructed images are often required, for instance, T_2-weighted images at multiple echo times for transverse relaxation mapping. A class of parametrized MRI models encompasses both exponential and non-exponential models of the MRI signal that describe its decay characteristics.

Parameter estimation is challenging due to ill-posedness of the majority of MR models (Laule and MacKay, 2014). The solution of a well-posed problem exists, is unique and changes continuously with changes in the initial conditions of the system (Tikhonov et al., 2013). In this work, we develop signal models for MRI applications and utilize appropriate estimation procedures to mitigate the adverse effects of ill-posed problem formulation on model inference. The strength and utility of parameter mapping strategies is strongly dependent on the signal model and robustness of the estimation algorithm. An ideal signal model provides a complete description of the physical system or process it represents whilst retaining the desirable mathematical properties, such as small number of parameters, well-posedness etc. An estimation algorithm plays a fundamental role in determining robust and accurate parameter values that describe the physical system at hand as completely as possible.

1.1 Multicompartment MRI models

Multicompartment modelling in MRI is an exciting modelling paradigm that has found diverse applications in a wide range of MRI-based imaging modalities, such as T_2-weighted imaging (Whittall and MacKay, 1989; Layton et al., 2013), myelin water imaging (Wu et al., 2012; Sati et al., 2013; Nam et al., 2015; Li et al., 2015; Wu et al., 2017), quantitative susceptibility mapping (Sood et al., 2017),

diffusion-weighted MRI (DW-MRI) (Niendorf et al., 1996; Clark and Bihan, 2000; Assaf et al., 2004, 2008; Alexander, 2008; Behrens et al., 2003; Yablonskiy et al., 2003) and sodium imaging (Hubbard, 1970; Blunck et al., 2018). Biophysical parameters derived from the multicompartment models have contributed significantly towards increasing our knowledge of the complex physiological processes present in the body. The main focus of this thesis is the utility, development and assessment of multicompartment models in the fields of sodium and diffusion MRI.

Multicompartment models of MR signal form a parametric class of models. In this class, the MR signal is assumed to be composed of the weighted sum of two or more distinct MR signals arising from separate compartments or components. These compartments are conceptualized representations of the effects of environmental inhomogeneities on NMR-related processes in a spin system. The definition and attributes of a compartment are set by the nature of weighting on the MR signal, such as T_2 components of transverse relaxation. Compartments representing geometrical properties of tissue, such as restricted diffusion are regions with distinct physical boundaries in tissue which could be spatially distributed. On the other hand, transverse relaxation based components are abstract compartments to help explain the MR signal. Compartments can exist in isolation or they can be in state of exchange. This thesis is primarily concerned with multicompartment modelling of T_2 and T_2^* relaxation and diffusion weighted MR signals, however, a description of susceptibility weighted compartments is provided for completeness. In the following text, the terms compartment and component are used interchangeably.

Compartmentalized Transverse Relaxation in Spin-1/2 Systems

Transverse relaxation in a one compartment spin-1/2 system is an exponentially decaying signal, described by the time constant, T_2 (Bloch, 1946). The value assumed by T_2 depends upon the spin-spin interactions between neighbouring spins. Local tissue inhomogeneities have the potential to alter the distribution of T_2 in a voxel, leading to multiple compartments each described by a distinct T_2 value (MacKay et al., 2006). The number of T_2 components depends on the chosen signal model and can range from 1 to infinity. Multiple T_2 components can exist in isolation or in the form of exchanging pools (Mulkern et al., 1989).

Compartmentalized Transverse Relaxation in Spin-3/2 Systems

Nuclei of a spin-3/2 system possess both magnetic and electric quadrupole moments (Slichter, 2013). Complex electromagnetic interactions between magnetized nuclei and surrounding molecular structure is known to give rise to bi-exponential transverse decay in a single homogeneous compartment (Hubbard, 1970). Similar to spin-1/2 systems, multiple T_2 compartments form depending on the structure and chemical composition of tissue. In the presence of multiple relaxation pools, a multi-component distribution of T_2 arises (Bull, 1972).

Diffusion Compartments

Spins diffusing in complex cellular environments undergo restricted or hindered self-diffusion due to the presence of physical barriers (Beaulieu, 2002). Differences in underlying diffusion mechanisms in tissue lead to differential attenuation of MR signal. Therefore, multi-compartment models of diffusion are employed to gain insights into microstructural organization of tissue (Beaulieu, 2002). Two-component models of diffusion consider two discrete compartments, often assigned to intra-cellular restricted and extra-cellular hindered diffusion (Niendorf et al., 1996; Clark and Bihan, 2000; Assaf et al., 2004, 2008; Behrens et al., 2003). The two pool model of Kärger (1985) permits exchange between compartments. Multicompartment diffusion models assume the presence of three (Barazany et al., 2009), four (Alexander, 2008) or a continuum of compartments (Yablonskiy et al., 2003). Geometric models of diffusion in white matter have also been parameterised by axon diameter, with the aim of inferring Axon Diameter Distribution (ADD) non-invasively (Assaf et al., 2008; Alexander et al., 2010). Compartmentalized diffusion models have been used extensively to characterize neurite orientation dispersion and density (Zhang et al., 2011), diffusion changes associated with axonal injury (Granziera et al., 2009) and tissue microstructure (Kaden et al., 2016).

Compartments in Quantitative Susceptibility Mapping

Quantitative susceptibility mapping (QSM) measures the concentration of certain chemical biomarkers, such as iron, gadolinium and calcium, by sensitizing the MR signal to the changes in the magnetic susceptibility properties of the underlying tissue (Acosta-Cabronero et al., 2013; Chen et al., 2014). In QSM, a two-compartment model of water and fat pools (Hernando et al., 2008, 2010) expresses each compartment as a complex plane wave characterized by an amplitude, a frequency shift due to susceptibility changes and a T_2 value. A three compartment model takes into account the frequency shifts in WM structures attributed to the myelin water fraction, intra-axonal restricted and extra-axonal mobile water pools (Sati et al., 2013; Van Gelderen et al., 2012; Li et al., 2015; Sood et al., 2017). Similarly, the three-compartment model of Sukstanskii and Yablonskiy (2014) incorporates the effects of WM orientation on the signal by replacing the myelin water fraction compartment with an orientation dependent myelinated axon compartment.

1.2 Thesis Overview

This thesis presents a statistical signal processing framework (Figure 1.2). The measured MR signal, $\boldsymbol{y}$, is input to an estimation framework which solves an optimization problem for the identification of best possible parameter estimates. The optimization problem is expressed in the form of a cost function, $c(\boldsymbol{\theta}, \boldsymbol{y})$. The aim of optimization is to find the parameter vector, $\hat{\boldsymbol{\theta}}$, that minimizes the cost function given a signal model, $\boldsymbol{x}(\boldsymbol{\theta})$. In chapters 3 & 4, we develop statistical signal models

that describe the MR signal in sodium and diffusion weighted MRI applications. Chapter 5 explores the potential of averaging mulitecho MRI data into a composite image for signal-to-noise (SNR) improvement and construct an optimization problem for the identification of optimal number of echoes. Assessment of an estimation framework is curial for establishing the veracity of parameter estimates, therefore, in chapter 6 we develop a data-dependent assessment framework for MR signal decay models.

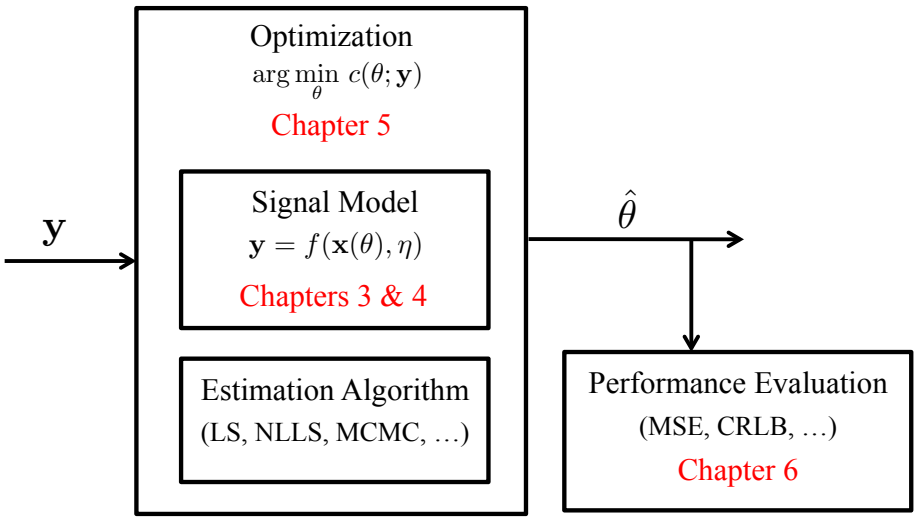

Figure 1.2: A typical parameter estimation framework.

1.2.1 Thesis Outline

Development and application of accurate MRI signal models requires an understanding of biophysical organization and function of tissue, physical origin of the NMR signal and the fundamentals of estimation theory. Therefore, the work presented in this thesis is divided into five main chapters, including a theoretical background chapter that provides the basic concepts of NMR physics relevant to the work presented in the later chapters. The final concluding chapter provides a summary of the main contributions of this work and suggests future research directions.

In Chapter 2, we introduce the concepts of nuclear spin from a pseudo-quantum mechanics perspective, necessary conditions for nuclear magnetic resonance, and temporal characteristics of an MR signal. We describe theoretical basis of transverse relaxation in spin-1/3 and spin-3/2 systems. Further, spin dynamics in the presence of self-diffusion of water molecules is described, along with the description of a pulse sequence commonly employed for sensitizing MR signal decay to diffusion.

In Chapter 3, we develop a continuum distribution model of T_2^* transverse relaxation decay for sodium MRI applications. We introduce two novel tissue parameters that relate the sodium MR signal to the underlying tissue microstructure. The first parameter, the mean T_2^* time constant, is derived from the mean of a gamma distribution of T_2^* values and describes the average transverse relaxation profile of the tissue. The second parameter, the fast fraction, calculated from the area under the curve of the gamma distribution, provides the volume fraction of the fast decaying T_2^* component and is an important biomarker of tissue organization and structure. A complete modelling and estimation framework for MR signal decay is presented.

In Chapter 4, we shift our focus to multicompartment modelling in DW-MRI. Specifically, we develop a novel statistical modelling framework for inferring Axon Diameter Density (ADD) under long diffusion gradient pulse regime. We demonstrate that, theoretically, in the presence of long diffusion gradients, maximum separation is achievable between the DW-MRI signals arising from axons with differing radii. We assume that the ADD in white matter structures conforms to a generalized gamma probability distribution and develop a closed-form analytical signal model. In order to validate our signal model, we perform simulation and experimental studies on an ovine optic nerve. Under simulated conditions, our model successfully provides meaningful estimates of ADD distribution in the simulated optic nerve with a known ADD. However, the model fails to predict the ADD in real DW-MRI experimental data, exposing the limitations of multicompartment modelling approach in describing tissue microstructure. This chapter provides a motivating example for the importance of estimation performance metrics, and the fact that assessment of model-fit is a crucial component of parameter estimation in MRI analyses. A second contribution of this work is to expose the limitations of Cramer Rao lower bound analyses of diffusion-weighted MRI models. The Cramer Rao lower bound has been frequently employed in MRI as a metric of precision and a method for experimental design. While it is understood that the CRLB is valid only under assumptions of model correctness, we demonstrate how misleading the CRLB can be in ADC estimation.

In Chapter 5, we capitalize on the potential of combining multiecho MRI data to achieve improvement in the SNR of low-intensity and high-noise MRI images, such as the sodium MRI data Chapter 3. We investigate the impact of the number of echoes used in the averaging process on the overall SNR gain and develop voxelwise model-based optimization strategies for maximum SNR improvement. As the main contribution, we provide a practical way of weighting and combining multiecho data that can be utilized for two separate purposes. First, for producing high-contrast structural images with enhanced visual quality and regional differentiation. Second, for increasing sensitivity to a number of tissue contrast mechanisms through sensitivity-optimized SNR improvement. A secondary contribution of this work is in establishing the equivalence in optimized SNR gain under either Gaussian- or Rician-distributed receiver noise model.

The assessment of model fit in MRI applications is a crucial step in determining the veracity of the resultant parameter maps. In Chapter 6, we propose a framework for assessment of model fit based on a decomposition of the model likelihood function into a term that encapsulates accuracy and a second term that summarises the precision of the parameter estimates. We apply our framework to the estimation of apparent diffusion coefficients (ADCs) from DW-MRI data, and demonstrate that while the bi-exponential model can achieve a high level of accuracy, it lacks the precision that arises from a continuum compartment model of ADC based on a gamma distribution. This lack of precision correlates with increased regional heterogeneity in the ADC maps. We show that the kurtosis parameters estimated from application of the diffusion kurtosis model are similarly lacking precision and correlate with higher spatial heterogeneity. We propose the use of the Observed Fisher Information as an empirical metric of precision that is not constrained by an assumption of model correctness. Thus robust assessment of model fit in quantitative MRI can be achieved using a joint Maximum Likelihood and Obseved Fisher Information (MLOFI) analysis of the data.

CHAPTER
TWO

Background

This chapter presents the fundamental concepts in MR physics and signal detection. MR images are formed through the application of complicated stationary and oscillating magnetic fields, along with a sophisticated reception and signal processing setup. An MRI scanner generates a strong static magnetic field that causes the sub-atomic nuclear spins present in the body to align and to produce a net magnetization in equilibrium. Applying a short-lived low-power oscillating magnetic field to the object of interest disturbs its equilibrium giving rise to an NMR signal (Bloch, 1946). As the magnetization regains equilibrium, a decaying MR signal induces a measurable voltage in a receiver coil. Mathematical models relate the measured MR signal to the underlying tissue characteristics, making MRI an invaluable imaging and diagnostic tool.

Signal localization is achieved by superimposing the static magnetic field by a weak spatially varying field, known as the gradient field (Lauterbur et al., 1973). The gradient field produces a spatial frequency dependent magnetization. In a typical MRI acquisition, successive excitation is done, each time with a slightly different gradient field, thus allowing to populate the spatial frequency space called the k-space (Ljunggren, 1983; Twieg, 1983). The image is reconstructed by linearly transforming the k-space data into the image space using a Fourier transform.

In this chapter, we focus on the theory of MR signal formation and modelling which provides the foundation for the experimental chapters.

2.1 Fundamentals of MRI

Spin is an intrinsic property of atomic nuclei and other sub-atomic particles. Spin systems are composed of ensembles of spins and give rise to detectable signals under resonance conditions. Therefore, an understanding of the physical mechanisms describing the behaviour of a spin system is desirable for constructing accurate models of an MR signal. A basic description of spin dynamics from a semi-classical point of view is presented in this chapter. Fundamental concepts pertaining to spin-1/2 systems are presented. A brief introduction to higher order spin systems is provided later in the chapter.

Spin in an Atomic Particle

Atomic particles possess four fundamental physical properties: mass, electric charge, angular momentum and magnetic moment. The angular momentum combines orbital angular momentum possessed by orbiting particles, such as an electron orbiting a nucleus, and the spin angular momentum, conceived as the rotation of a particle around an axis, such as a nucleus rotating about its axis. Spin angular momentum is a vector quantity and is directly proportional to the magnetic moment, $\boldsymbol{\mu}$, through a fundamental symmetry theorem (Levitt, 2001):

$$\boldsymbol{\mu} = \gamma \boldsymbol{S} \tag{2.1}$$

where γ is the constant of proportionality known as the gyromagnetic ratio, usually expressed in MHz/T. The magnitude of $\boldsymbol{\mu}$ is given by

$$|\boldsymbol{\mu}| = \gamma \hbar \sqrt{I(I+1)}, \tag{2.2}$$

where $\hbar = h/2\pi$ is the reduced Plank's constant and I is the spin quantum number. I is a fixed quantity that describes a nucleus in its stable ground state and can be an integer or a half-integer, $I = 0, \frac{1}{2}, 1, \frac{3}{2}, 2, \ldots$ (Callaghan, 1993). The value of I for a particular nucleus is determined by its mass and charge number (Liang and Lauterbur, 2000). The direction of $\boldsymbol{\mu}$ is completely random in the absence of an external magnetic field.

A spin placed in a spatially homogeneous external magnetic field, $\boldsymbol{B}$, experiences a torque which is equal to the rate of change of spin angular momentum:

$$\frac{d\boldsymbol{S}}{dt} = \boldsymbol{\mu} \times \boldsymbol{B}. \tag{2.3}$$

Since $\boldsymbol{\mu} = \gamma \boldsymbol{S}$, it follows that:

$$\frac{d\boldsymbol{\mu}}{dt} = \gamma \boldsymbol{\mu} \times \boldsymbol{B}. \tag{2.4}$$

The motion of an isolated spin in $\boldsymbol{B}$ is described by the solution of (2.4). We assume that $\boldsymbol{B} = B_0 \hat{k}$ is the applied magnetic field with strength B_0 along the z-direction of the laboratory frame of reference. Then, $\boldsymbol{\mu}$ is expressed as

$$\boldsymbol{\mu} = \mu_x \hat{i} + \mu_y \hat{j} + \mu_z \hat{k}, \tag{2.5}$$

where μ_x, μ_y and μ_z are the components of $\boldsymbol{\mu}$ along x-, y- and z- directions of the laboratory frame. The solution to (2.4) is given by

$$\mu_{xy}(t) = \mu_{xy}(0) e^{-i\gamma B_0 t} \tag{2.6}$$

$$\mu_z(t) = \mu_z(0), \tag{2.7}$$

where $\boldsymbol{\mu}_{xy} = \mu_x \hat{i} + \mu_y \hat{j}$ is the magnetization vector in the transverse plane and $\mu_{xy}(0)$ and $\mu_z(0)$ are the initial values. Hence, the magnetic moment, $\boldsymbol{\mu}$, precesses about the B_0 field in the xy-plane with a time-independent component along z-axis. The angular frequency of precession is

$$\omega_0 = \gamma B_0. \tag{2.8}$$

The angular frequency ω_0 is known as the Larmor frequency.

Ensemble behaviour of Spins

An ensemble of spins gives rise to the bulk magnetization, $\boldsymbol{M}$, which is the vector sum of the constituent nuclear magnetic dipoles.

$$\boldsymbol{M} = \sum_{i=1}^{N_s} \boldsymbol{\mu}_i \tag{2.9}$$

where N_s is the total number of spins in the spin system. In the absence of an external magnetic field, the magnetic moments are randomly oriented and cancel each other, which leads to zero bulk magnetization.

Recall that a single magnetic moment, $\boldsymbol{\mu}$, precesses about an external magnetic field, $\boldsymbol{B}$. The spin quantum model states that the z-component of $\boldsymbol{\mu}$ in (2.2) is discretized and is given by

$$\mu_z = \gamma \hbar m_I, \tag{2.10}$$

where m_I is the magnetic quantum number, defined by a set of $(2I+1)$ values:

$$m_I = -I, -I+1, \ldots, I. \tag{2.11}$$

Hence, for spin-1/2 nuclei, there are two possible orientations between μ_z and B_0, with angle $\theta = acos(\frac{m_I}{\sqrt{(I(I+1))}})$ between them. The direction of the transverse component, $\boldsymbol{\mu}_{xy}$, is random as it can be oriented towards any point in the transverse plane. Therefore, $\boldsymbol{M}$ is decomposed into its components,

$$\boldsymbol{M} = \sum_{i=1}^{N_s} \mu_z \hat{k} + \sum_{i=1}^{N_s} \mu_x \hat{i} + \sum_{i=1}^{N_s} \mu_y \hat{j}. \tag{2.12}$$

In this equation, the last two terms are zero, as $\boldsymbol{\mu}_{xy}$ is randomly oriented, leading to zero bulk magnetization in the transverse plane. The value of μ_z is given by (2.10).

In the presence of an external magnetic field, the spins possess magnetic energy due to interactions between the magnetic moment, $\boldsymbol{\mu}$, and the applied field, $\boldsymbol{B}$:

$$E_{mag} = -\boldsymbol{\mu} \,.\, \boldsymbol{B} \tag{2.13}$$

$$= -\gamma \hbar m_I B_0. \tag{2.14}$$

Hence, for a spin-1/2 system, magnetic moments with z-component aligned parallel (pointing up) or anti-parallel (pointing down) to $\boldsymbol{B}$ are in low or high energy states,

respectively. This phenomenon is known as the Zeeman splitting. Let $N_\uparrow$ and $N_\downarrow$ be the number of spins in low and high energy states. The spins prefer to reside in the low energy state (pointing up), which is more stable, and consequently, the $N_\uparrow$ is slightly larger than $N_\downarrow$, at a given temperature, T_s. The ratio $\frac{N_\uparrow}{N_\downarrow}$ is defined by the Boltzmann relationship:

$$\frac{N_\uparrow}{N_\downarrow} = \exp\left(\frac{\Delta E}{KT_s}\right) \approx 1 + \frac{\gamma\hbar B_0}{KT_s}, \tag{2.15}$$

where ΔE is the energy difference between low and high energy levels and K is the Boltzmann constant (1.38×10^{-23}J/K). Please note that the unconventional symbol for the Boltzmann constant has been used to avoid misunderstanding with the notation for the unit vector along z direction, $\hat{k}$. The difference $N_\uparrow - N_\downarrow$ is approximated as:

$$N_\uparrow - N_\downarrow = N_s \frac{\gamma\hbar B_0}{2KT_s}. \tag{2.16}$$

Therefore, the bulk magnetization,

$$\boldsymbol{M} = \left(\sum_{m=1}^{N_\uparrow} \mu_z - \sum_{i=1}^{N_\downarrow} \mu_z\right)\hat{k} \tag{2.17}$$

$$= \frac{1}{2}(N_\uparrow - N_\downarrow)\gamma\hbar\hat{k} \tag{2.18}$$

$$= \frac{\gamma^2\hbar^2 B_0 N_s}{4KT_s}\hat{k}. \tag{2.19}$$

At equilibrium, the bulk magnetization vector, $\boldsymbol{M}$, is aligned parallel to the direction of the applied magnetic filed, which is denoted as M_z^0 in the later text.

The Bloch Equation

In the previous section, we described the formation of observable bulk magnetization, $\boldsymbol{M}$, along the direction of a static magnetic field, $\boldsymbol{B}_0$. The transverse component of $\boldsymbol{M}$ is zero due to random phase distribution of magnetic moments. Application of a short-lived oscillating magnetic field, $\boldsymbol{B}_1(t)$, disturbs $\boldsymbol{M}$ from the state of equilibrium. The $\boldsymbol{B}_1(t)$ field is commonly referred to as an r.f. pulse as it oscillates in the r.f. frequency range. $\boldsymbol{B}_1(t)$ field oscillating at the Larmor frequency of the spin systems establishes phase coherence in precessing spins, giving rise to nuclear magnetic resonance. The macroscopic effects of the application of $\boldsymbol{B}_1(t)$ field manifest as the tipping of $\boldsymbol{M}$ away from the z-axis at an angle α, known as the flip angle, as it starts to precess about the $\boldsymbol{B}_1$ field. A 90^o r.f. pulse tips $\boldsymbol{M}$ completely into the transverse plane ($\alpha = 90^o$).

Immediately after the application of an r.f. pulse, the spin system tries to regain thermal equilibrium which is achieved through two separate relaxation process: spin-lattice relaxation and spin-spin relaxation. The dynamic behaviour of the bulk magnetization, $\boldsymbol{M}$, in the presence of an external magnetic field, $\boldsymbol{B}$, after it has been disturbed from equilibrium, is governed by a phenomenological differential equation, known as the Bloch equation (Bloch, 1946):

$$\frac{d}{dt}\boldsymbol{M}(t) = \gamma \boldsymbol{M}(t) \times \boldsymbol{B}(t) - \frac{(M_z - M_z^0)\hat{k}}{T_1} - \frac{M_x \boldsymbol{i} + M_y \boldsymbol{j}}{T_2} \tag{2.20}$$

where M_x, M_y, M_z are the components of the bulk magnetization in x, y and z direction and M_z^0 is the initial magnetization at equilibrium. $\boldsymbol{B}(t)$ is the sum of both static and oscillating magnetic fields. The parameters T_1 and T_2 describe the spin-lattice and spin-spin relaxation processes, respectively.

The first term in the Bloch equation characterizes the behaviour of $\boldsymbol{M}$ in the presence of the $\boldsymbol{B}(t)$ and is similar to the motion of an isolated spin in $\boldsymbol{B}$ as given in (2.4). The process of the recovery of the longitudinal magnetization, called longitudinal relaxation, is characterized by the second term in the Bloch equation. The third term describes the destruction of transverse magnetization: this process is known as transverse relaxation.

Spin-Lattice Relaxation

Nuclei of a spin system undergo complex magnetic interactions with the microscopic magnetic fields arising from the random thermal motion of surrounding molecular structures, collectively referred to as the lattice.

Prior to application of an r.f. pulse, the nuclei of a spin system exist in thermal equilibrium with the lattice. After an r.f. pulse is applied, the excess energy absorbed by the spins is dissipated into the lattice in the form of increased rotational and vibrational motion. This transitory relaxation phenomenon is known as spin-lattice relaxation and is responsible for the recovery of longitudinal bulk magnetization. Mathematically, spin-lattice relaxation is a first order process:

$$\frac{dM_z}{dt} = -\frac{M_z - M_z^0}{T_1}, \tag{2.21}$$

with solution,

$$M_z(t) = M_z^0(1 - e^{-t/T_1}) + M_z(0)e^{-t/T_1}, \tag{2.22}$$

where $Mz(0)$ is the longitudinal magnetization immediately after the application of r.f. pulse. The time constant, T_1, is the time taken by the longitudinal component to regain 63% of its thermal equilibrium value. i.e.

$$M_z(T_1) \approx 0.63 M_z^0. \tag{2.23}$$

Spin-Spin Relaxation

Establishment of phase coherence in the transverse components of magnetic moments through application of an r.f. pulse leads to the emergence of non-zero transverse magnetization. In the absence of an r.f. pulse, the spins start to dephase due to complex spin-spin magnetic interactions. As a result, the transverse component decays, leading to the its complete destruction as spins regain thermal equilibrium. This process, known as transverse relaxation, is mathematically characterized by a first order differential equation:

$$\frac{dM_{xy}}{dt} = -\frac{M_{xy}}{T_2}, \tag{2.24}$$

with solution

$$M_{xy}(t) = M_{xy}(0)e^{-t/T_2}, \tag{2.25}$$

where $M_{xy} = M_x + iM_y$, and $M_{xy}(0)$ is the initial transverse magnetization after the r.f. pulse. At time T_2, 63% of transverse magnetization is destroyed due to spin dephasing, i.e.,

$$M_{xy}(T_2) \approx 0.37M_{xy}(0). \tag{2.26}$$

The decay constant, T_2, describes the transverse decay of MR signal in a homogeneous volume of spins in the absence of spatial variations present in the strength of the applied field, $\boldsymbol{B}_0$. In reality, both sample and magnetic field inhomogeneities exist due to the complex physiochemical composition of tissue and chemical shift artefacts, i.e. variations in the local magnetic field experienced by nuclei due to the chemical nature of the molecules they reside in. Consequently, the transverse decay happens at a faster rate than that characterized by T_2. The frequency distribution in a heterogeneous spin system is described by the spectral density function, $J(\omega)$. In the presence of field inhomogeneity, ΔB_0, and under the assumption of a Lorentzian spectral density function, the faster transverse decay is characterized by another time constant, T_2^*, where

$$\frac{1}{T_2^*} = \frac{1}{T_2} + \gamma\Delta B_0. \tag{2.27}$$

2.2 Multiecho MRI

During relaxation, an observable voltage signal is induced in the receiver coil due to the time-varying behaviour of bulk magnetization, $\boldsymbol{M}$. The induced voltage, according to the Faraday's law of electromagnetic induction, is directly proportional to the rate of change in the magnetic flux through the receiver coil. Slowly

varying z-component induces negligible voltage, and the measured signal is predominantly produced by the transverse magnetization, $\boldsymbol{M}_{xy}$. Therefore, the time-varying NMR signal in the transverse plane is the only observable signal.

Free induction decay

The transient signal induced in a receiver coil after the application of an α° r.f. pulse is known as the free induction decay (FID) (Liang and Lauterbur, 2000). Given a spectral density function, $J(\omega)$, FID is described as:

$$S(t) = \sin(\alpha) \int_{-\infty}^{\infty} J(\omega) e^{-t/T_2(\omega)} e^{-i\omega t} d\omega,\ t \geq 0. \tag{2.28}$$

The FID in a homogeneous spin system, with a single spectral component precessing at ω_0 is expressed as

$$S(t) = M_z^0 \sin(\alpha)\, e^{-t/T_2}\, e^{-i\omega_0 t}. \tag{2.29}$$

An exemplar FID signal is shown in Figure 2.1. The magnitude of an FID signal depends on the initial bulk magnetization value along z-axis and the flip angle, α. The decay rate of FID is determined by the underlying spectral density distribution. In homogeneous spin systems, the decay rate of an FID signal is purely characterized by the T_2 time constant. However, in the presence of heterogeneous environments, the time constant, T_2^* determines the effective decay rate of an FID signal.

Echo formation

Recall that the application of an r.f. pulse establishes phase coherence in the transverse components of the magnetic moments. The FID signal is formed as the spins dephase due to spin-spin relaxation processes after the r.f. pulse. Re-establishment of phase coherence in the transverse magnetization is achievable either through reapplying a 180° r.f. pulse, resulting in the formation of a *spin echo*, or by applying magnetic field gradients for the *gradient echo* formation. As spins regain phase coherence, an emerging MR signal is induced in the receiver coil, followed by a decaying MR signal due to repeat dephasing of the spins. Hence, a two-sided echo signal is formed (Figure 2.2). The multiecho data employed in Chapter 5 was acquired using a gradient echo acquisition sequence, therefore, we will focus only on the formation of gradient echoes.

Gradient echoes

A gradient field, $\boldsymbol{B}_g$, is an inhomogeneous field whose z-component, $B_{g,z}$, varies along a particular direction (Liang and Lauterbur, 2000). Presence of a linear

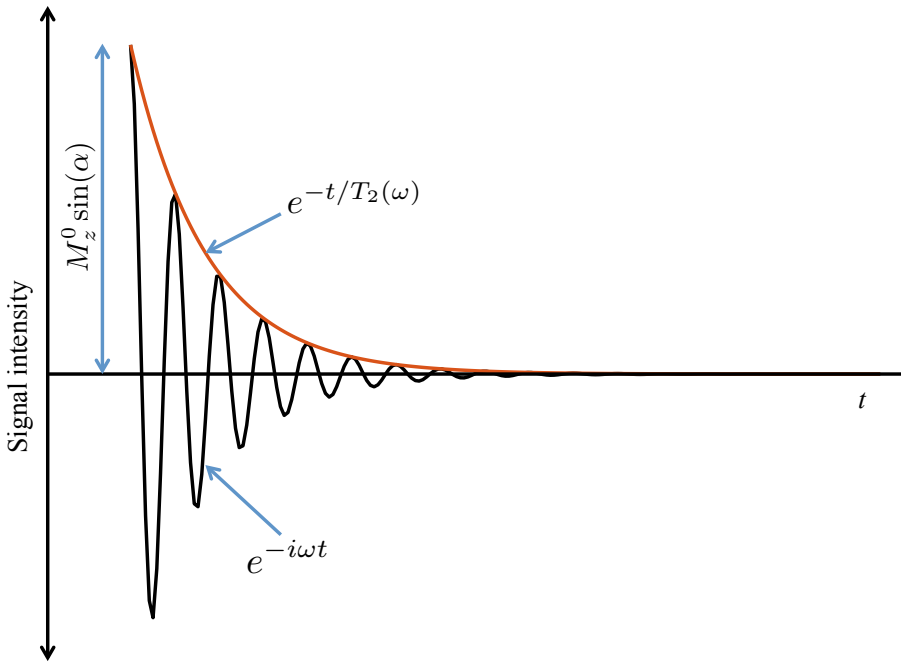

Figure 2.1: An exemplar FID.

gradient field introduces a linearly varying magnetic field. The overall magnetic field is given as

$$\boldsymbol{B}(r) = (B_0 + B_{g,z})\hat{k}, \tag{2.30}$$

where $r = x\hat{i} + y\hat{j} + z\hat{k}$ is the position vector, and

$$B_{g,z} = \boldsymbol{g}.\boldsymbol{r} = g_x x + g_y y + g_z z. \tag{2.31}$$

g_x, g_y, g_z describe the strength of gradient field along x-, y- and z-axis.

A gradient echo is formed through the application of a gradient waveform immediately after an r.f. pulse excitation. Consider the sequence diagram presented in Figure 2.3. After an α^o pulse, the gradient in negative x direction is turned on for time, τ. As a result, the spins start to dephase at a much faster rate than that described by T_2^*. The net phase accumulated by the spins during time τ that greatly exceeds the time constant of this faster transverse decay, is expressed as

$$\begin{aligned} \phi(x,t) &= \gamma \int_0^t -g_x\, x\, dt',\ 0 \le t \le \tau \\ &= -\gamma g_x\, x\, \tau. \end{aligned} \tag{2.32}$$

At time, τ, the transverse magnetization component has vanished completely. At this point, application of a positive x gradient of equal strength causes the spins to rephase, and a transverse magnetization component begins to emerge.

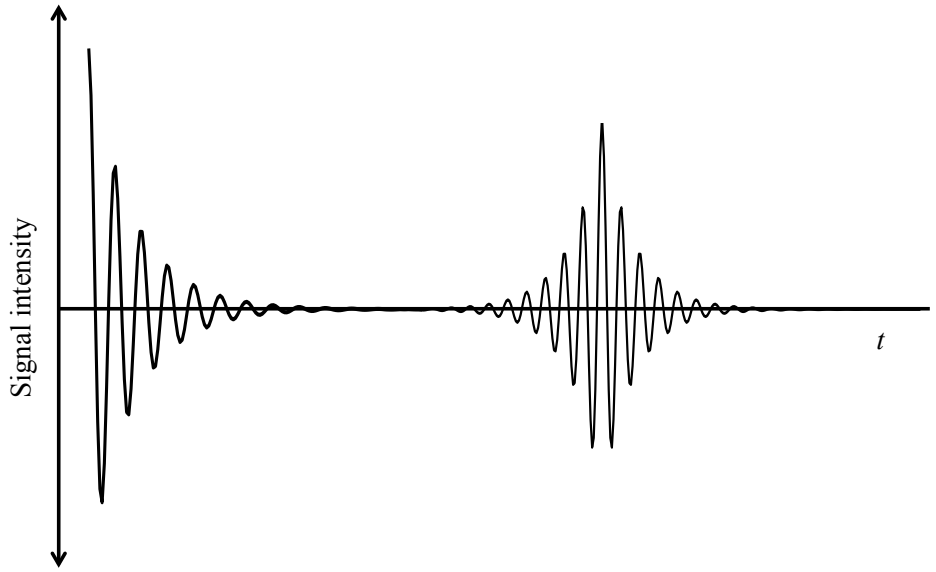

Figure 2.2: Formation of two-sided echo signal.

$$\phi(x,t) = -\gamma g_x\, x\, \tau + \gamma \int_{\tau}^{t} g_x\, x\, dt',\ \tau \leq t \leq 2\tau \tag{2.33}$$

$$= -\gamma g_x\, x + \gamma g_x\, x\, (t-\tau). \tag{2.34}$$

In the absence of field inhomogeneities, complete phase coherence is achieved at time 2τ (i.e. $\phi(x, 2\tau) = 0$). However, in reality, the maximum gradient amplitude carries a T_2^* weighting due to field inhomogeneity effects. After time 2τ, transverse relaxation decay is observed as a result of accelerated spin depahsing under positive gradient, g_x. Multiple gradient echoes are generated through repetitive switching of the gradient g_x between positive and negative polarities.

2.3 Diffusing Spins - Bloch-Torrey Equation

The Diffusion Process

Diffusion is a transport phenomenon which is related to random walks of molecules in a medium. Diffusion involves random motion of particles from one place to another without requiring bulk motion of the molecules. Self diffusion is a process in which molecules randomly travel in the same medium due to thermal agitation in the absence of any concentration gradient. Self diffusion is described mathematically as the displacement probability of molecules $P(s,t)$, where s is the relative displacement of the molecule during time t. Mathematically, self diffusion is described by Fick's second law of diffusion (Jones, 2010):

$$\frac{\partial P}{\partial t} = D\nabla^2 P, \tag{2.35}$$

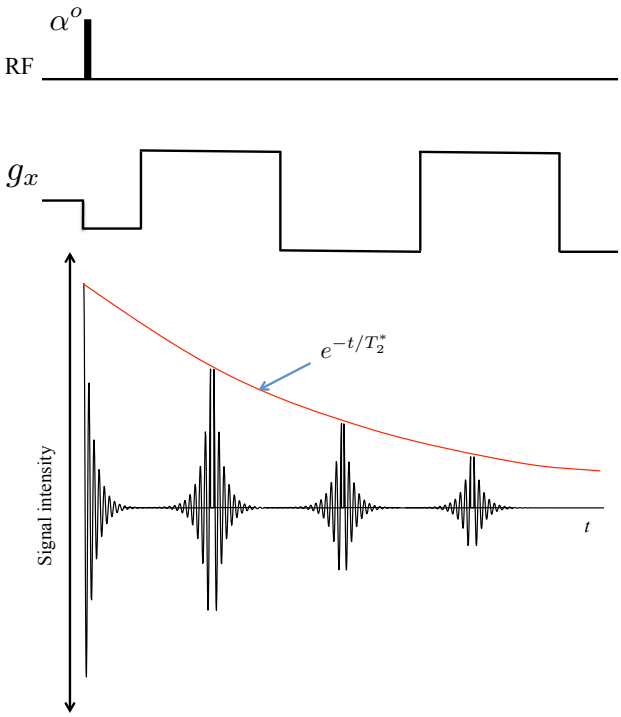

Figure 2.3: Formation of multiple gradient echoes after an r.f. pulse.

where D is the diffusion coefficient of the medium in $\mu m^2/s$ and ∇ is the gradient operator.

Diffusion of Bulk Magnetization

Self-diffusion of magnetized nuclei has a direct influence on the relaxation behaviour of spin systems. Torrey (1956) suggested a generalized Bloch equation that takes into account the effect of diffusing spins on the dynamics of a spin system. The Bloch-Torrey equation is a differential equation, given as:

$$\frac{d}{dt}\boldsymbol{M}(t) = \gamma \boldsymbol{M}(t) \times \boldsymbol{B}(t) - \frac{M_z - M_z^0}{T_1} - \frac{M_x \boldsymbol{i} + M_y \boldsymbol{j}}{T_2} + \nabla . \boldsymbol{D} \nabla M. \tag{2.36}$$

where $\nabla . \boldsymbol{v}$ is the divergence of a vector field $\boldsymbol{v}$, and $\boldsymbol{D}$ is the diffusion tensor:

$$\boldsymbol{D} = \begin{pmatrix} D_{xx} & D_{xy} & D_{xz} \\ D_{yx} & D_{yy} & D_{yz} \\ D_{zx} & D_{zy} & D_{zz} \end{pmatrix}, \tag{2.37}$$

where D_{xx}, D_{yy}, D_{zz}, is the diffusion coefficient in the x, y and z direction, respectively.

Diffusion of molecules is affected by the geometry of the confining space. Free diffusion is a phenomenon in which molecules diffuse freely in space without encountering any boundary along their path or any restriction on their motion. Presence of obstacles or reflecting objects in the confining space can alter the diffusion path of the particles and thus gives rise to hindered diffusion. In some structures, like cylinders, motion of particles may be restricted along some directions. Since the water molecules present inside biological tissues are mostly confined to spaces with boundaries, only restricted and anisotropic diffusion of water molecules is observed.

In isotropic self diffusion, molecules diffuse in all direction equally (i.e. $D_{xx} = D_{yy} = D_{zz} = D$), and the probability density function is a Gaussian distribution (Jones, 2010). However, when the molecules of a specific medium like water are trapped in a confined space with reflecting boundaries, the diffusion process becomes anisotropic and the Gaussian probability density function may no longer be able to predict the movement of these molecules. Anisotropic diffusion generally depends on the shape and properties of the confining medium (Assaf and Basser, 2005).

Random motion of water molecules within tissue micro-structures has the potential to provide important information about the geometrical structure of the tissue. For example, in case of long cylindrical structures like axons, the diffusion of water molecules is dominant along the principle axis of the fibre. Diffusion MRI is an indirect method of inferring geometric properties of tissues by observing random motion of locally present water molecules in the tissues (Grebenkov, 2007).

Restricted Diffusion

Restricted diffusion can mathematically be understood as Reflected Brownian Motion (RBM) (Grebenkov, 2007). RBM describes the random motion of a particle in a confined space with geometrical restrictions placed at the boundary. When a randomly moving particle encounters a boundary, it either gets reflected or absorbed by it. If we consider a smooth boundary, then the particle will primarily be reflected by it. A particle may undergo various reflections on the domain boundary. Mathematically, Reflected Brownian Motion of a diffusing particle is a stochastic process described as a Wiener process in a space with reflecting boundaries (Veestraeten, 2004).

2.3.1 Diffusion Weighted Imaging

In Diffusion Weighted Imaging (DWI), the diffusion properties of water trapped in the tissues are utilised to improve the contrast of the image (Jones, 2010). To make the MR signal sensitive to the presence of self diffusing water molecules present in the tissues, spatial inhomogeneities are introduced in the $\boldsymbol{B}_0$ through application of specialized diffusion gradients, $\boldsymbol{g}$ (see (2.31)). These diffusion gradients cause the Larmor frequency of the precessing moments to change depending on their

position. The most commonly used gradient pulse sequence for diffusion encoding is called Pulsed Gradient Spin Echo (PGSE) sequence proposed by Stejskal and Tanner in 1965 (Jones, 2010). This pulse sequence consists of a 90° B_1 pulse, followed by diffusion gradient pulses of strength, g (mT/m) and duration δ (ms) centred at around a 180° pulse. The time between these two gradient pulses is given by Δ(ms) (Figure 2.4).

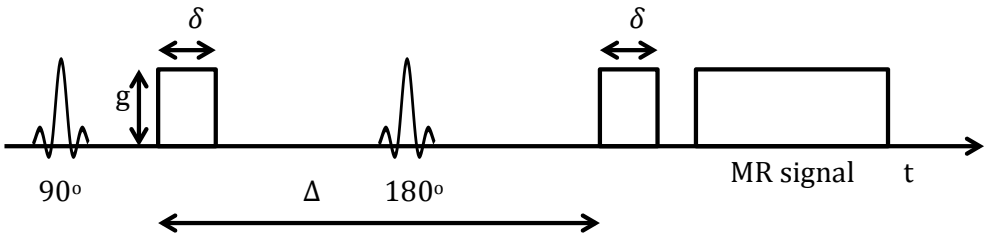

Figure 2.4: Stejskal-Tanner PGSE sequence for acquiring DW-MR images.

In the case of stationary protons, the first gradient pulse dephases the spins in the transverse plane and the second gradient pulse rephrases them without accumulation of any net phase during the process.

When the protons are not stationary, the first gradient pulse will dephase their spins, but due to their continuous motion, the second gradient pulse will not be able to rephase them perfectly. Net phase will be accumulated by these spins and this phase will in general depend on the diffusion coefficient and the paths travelled by the particles.

During time t, the net phase accumulated by precessing spins $\varphi(t)$ is given by

$$\varphi(t) = \int_0^t \gamma\, \mathbf{g}(t') \cdot \mathbf{r}(t') dt' \tag{2.38}$$

Dephasing causes a reduction in the signal amplitude and this signal attenuation is responsible for producing diffusion dependent contrast in the reconstructed MR images. In a uniform medium with a single diffusivity, D, this signal attenuation is modelled by the well known Stesjskal-Tanner equation (Stejskal and Tanner, 1965).

$$E/E_0 = \exp[-\gamma^2 g^2 \delta^2 (\Delta - \delta/3) D] = \exp(-bD) \tag{2.39}$$

The b-value or the b-factor given in the above equation is defined as

$$b = (\gamma g \delta)^2 \left(\Delta - \frac{\delta}{3}\right) \tag{2.40}$$

In the above equation, the term $\left(\Delta - \frac{\delta}{3}\right)$ quantifies the effective diffusion time. The b-value is the indicator of overall strength of diffusion labelling of the spins.

The signal acquired from DWI experiment can then be represented as

$$E = E_0 \exp^{-\frac{TE}{T_2}} . \exp^{-bD} \tag{2.41}$$

where E_0 is the signal intensity in the absence of any diffusion weighting, TE is the echo time and D is the apparent diffusivity. It should be noted that the diffusion constant D is influenced by tissue structure, cell viscosity and permeability. Therefore, in MRI the term Apparent Diffusion Coefficient (ADC) is used to describe this difference (Horsefield and Jones, 2002; Stejskal and Tanner, 1965).

2.4 Relaxation processes in Spin-3/2 Systems

In the presence of an external magnetic field, $\boldsymbol{B}_0$, the nuclei of spin-3/2 systems can exist in four discrete energy states, described by the four possible values assumed by the magnetic quantum number, $m_{3/2} \in \{-3/2, -1/2, 1/2, 3/2\}$, as given by (2.11). The electric quadrupole moment describes the elliptical shape of the nuclear charge distribution (Slichter, 2013). The electric quadrupole moment is zero in nuclei with spherically symmetric charge distribution, such as hydrogen nuclei. Departure from spherical symmetry is observed in higher order spin-3/2 systems due to an asymmetrical charge distribution. Hence, spin-3/2 nuclei, such as sodium nuclei, possess non-zero electric quadrupole moment. The magnetic energy possessed by the nuclei in the absence of quadrupole moments is given by (2.14). However, a shift in the discretized energy levels is observed due to electric coupling between the quadrupole moments and local electric field gradients present at the nucleus. This energy shift, to a first order approximation, is given by

$$E_{mag} = -\gamma\hbar B_0 m_I + \frac{e^2qQ}{4I(2I-1)}\left(\frac{3\cos^2\theta - 1}{2}\right)[3m^2 - I(I-1)], \tag{2.42}$$

where e = elementary charge, Q = electric quadrupole moment, q = electric field gradient and θ is the angle between $\boldsymbol{B}_0$ and the principle axis of the magnetic moment, $\boldsymbol{\mu}$. Hence, the energy shifts are identical when $m = \pm 1/2$ or $m = \pm 3/2$. The corresponding shift in Larmor frequency is

$$\Delta\omega = \frac{e^2qQ}{2}(3\cos^2\theta - 1). \tag{2.43}$$

As evident from eqns (2.42) and (2.43), the strength of quadrupole coupling depends on the electric field gradient present at the nucleus. Fluctuations in the electric field gradient, caused by the changes in the local nuclear charge distribution due to random molecular motion and variations in temperature, lead to variations in the quadrupole interactions.

Random molecular motion, such as vibration, rotation and collision, is usually expressed in terms of the correlation time, τ_c, which characterizes the average time spend by a molecule in a particular state (Abragam, 1961). For example, the

average time taken by a molecule to rotate by 1 radian in known as the rotational correlation time. The correlation function that describes the average molecular motion is related to the spectral density function, $J(\omega)$, through a Fourier transform. $J(\omega)$ describes the effects of surrounding molecular environment on the transverse and longitudinal relaxation processes (Abragam, 1961).

Spin transitions between adjacent energy levels are detectable through application of a single α° r.f. pulse. This acquisition scheme is known as single quantum filtering, as opposed to triple quantum filtered MRI that employs advanced filtering techniques to measure higher-order transitions. The sodium MRI presented in this work is from single quantum filtering techniques. In extreme narrowing conditions, i.e. when τ_c is shorter than the Larmor period of spins, random fluctuations in the electric field gradient average out to zero. Extreme narrowing conditions are present when the nuclei residing in rapid motion regimes, such as fluid media, undergo rapid changes in their position and orientation.

Hubbard (1970) studied the relaxation processes in uniform ordered spin-3/2 structures, such as tissue, where τ_c is not short compared to the Larmor frequency of the system and predicted bi-exponential signal decay, attributed to the non-vanishing electric field gradients. The bi-exponential transverse decay in a homogeneous ordered medium is given as:

$$M_{xy}(t) = 0.6e^{-t/T_{2\,\text{short}}} + 0.4e^{-t/T_{2\,\text{long}}}, \tag{2.44}$$

where

$$\frac{1}{T_{2\,\text{short}}} = \left(\frac{eQ}{\hbar}\right)^2 [J(0) + J(\omega_0)] \tag{2.45}$$

$$\frac{1}{T_{2\,\text{long}}} = \left(\frac{eQ}{\hbar}\right)^2 [J(\omega_0) + J(2\omega_0)], \tag{2.46}$$

and

$$J(\omega) = \frac{(eq)^2}{20} \frac{\tau_c}{1 + (\omega\tau_c)^2}. \tag{2.47}$$

Here the faster transverse relaxation characterised by the time constant, $T_{2\,\text{short}}$, describes the signal contributions due to faster satellite transitions (i.e. from 3/2 to 1/2 and -1/2 to -3/2). The slow component, $T_{2\,\text{long}}$, is predominantly arising from slower central transitions (from 1/2 to -1/2).

Under extreme narrowing condition, i.e. when $(\omega\tau_c)^2 << 1$,

$$\frac{1}{T_{2\,\text{short}}} = \frac{1}{T_{2\,\text{long}}} = \frac{1}{10}\left(\frac{e^2qQ}{\hbar}\right)^2 \tau_c, \tag{2.48}$$

which results in a mono-exponential transverse relaxation decay.

CHAPTER
THREE

Multiple Compartment Mapping in Sodium MRI

3.1 Introduction

Sodium (^{23}Na) is an important electrolyte present in living organisms, vital for cell integrity, cohesion and function (Isom, 2002; Dean, 1941). Neuronal transmission via action potentials is carried out through opening and closing of ^{23}Na and potassium gated ion channels (Horisberger, 2004), commonly known as the sodium pump. Pathological conditions such as cardiovascular disease(Smith et al., 1993; Schmidt et al., 1993), hypertension (Rüegg, 1992), impaired renal function (Graves et al., 1983), neurological disorders (Christo and El-Mallakh, 1993; El-Mallakh et al., 1993), pulmonary conditions (Smith et al., 1992), fetal abnormalities (Biver et al., 1990), diabetes and other metabolic disorders (Clerico and Giampietro, 1990; Rose and Valdes, 1994) have been associated with alterations in the sodium pump activity. With a nuclear moment of 3/2, ^{23}Na is the second most abundant NMR observable nucleus in the human body. The MR signal from ^{23}Na nuclei is three to four orders of magnitude weaker than that of the ^{1}H MR signal (Madelin and Regatte, 2013), making it challenging to obtain a viable ^{23}Na MR signal at low field strengths. Recent advances in high field MR imaging and hardware design have led to acquisition protocols and analysis techniques tailored for imaging ^{23}Na. Thus to date there have been a wide variety of sodium MRI studies assessing developmental and pathophysiological processes including, but not limited to, neurogenerative diseases (Hilal et al., 1985; Grodd and Klose, 1988; Hancu et al., 1999; Rosen and Lenkinski, 2009), tumors (Hashimoto et al., 1991; Ouwerkerk et al., 2003; Nagel et al., 2011; Fiege et al., 2013), stroke (Tsang et al., 2011), multiple sclerosis (Inglese et al., 2010; Zaaraoui et al., 2012), Alzheimer's disease (Mellon et al., 2009), Huntington's disease (Reetz et al., 2012), breast cancer (Ouwerkerk et al., 2007), acute myocardial infraction (Jerecic et al., 2002; Parish et al., 1997; Ouwerkerk et al., 2005, 2008), diabetes (Chang et al., 2010), osteoarthritis (Wheaton et al., 2004), and nephropathy (Maril et al., 2006).

The dominant relaxation mechanism in spin 1/2 systems such as protons is the magnetic dipole interaction between spins and magnetic moments present in the surrounding environment. Spin-spin relaxation is described by a single exponential characterized by time constant, T_2. Practically, the presence of local field inhomogeneities leads to much faster transverse magnetization decay, governed by the time constant T_2^* that describes the envelope of the FID. In addition to magnetic dipole moments, nuclei with spin greater than 1/2, such as ^{23}Na nuclei, possess electric quadrupole moments, arising due to asymmetrical electric charge distribution (Slichter, 2013). The interactions of electric quadrupole moments with local electric field gradients results in accelerated spin relaxation (Hubbard, 1970). Therefore, transverse relaxation of ^{23}Na nuclei is produced by a combination of magnetic dipole-dipole and electric quadrupole coupling with the local electric field gradients.

The quadrupole interactions are influenced by constant molecular motion, such as translation and rotation. The correlation time, describing the fluctuations in the electric field gradient (EFG) at the nucleus, is the average time taken by a spin

to rotate by one radian (Abragam, 1961). Under extreme narrowing conditions, rapid isotropic molecular motion causes EFG at the nucleus to fluctuate more rapidly than the Larmor frequency, producing mono-exponential transverse spin relaxation (Hubbard, 1970). Without extreme narrowing conditions and under no chemical exchange, the quadrupole interactions have longer correlation time than the Larmor period, giving rise to rapid bi-exponential transverse relaxation, with 40% signal from central dipole interactions and 60% signal from satellite quadrupole interactions (Hubbard, 1970). Multi-exponential transverse relaxation is predicted in the case of exchanging nuclei without extreme narrowing conditions in the two pool spin system studied in (Bull, 1972; Goldberg and Gilboa, 1978).

Given the objective for sodium MRI to produce robust biomarkers of disease and disorder, accurate quantification of ^{23}Na concentration and relaxation properties is essential. The estimation of the transverse relaxation rate from multi-echo sodium MRI data is challenging, both due to the low SNR of sodium images, and the complex magnetic dipole and electric quadrupole coupling in tissue micro-environment. In ordered biological structures, ^{23}Na exists in various heterogeneous states such as free ^{23}Na ions, ^{23}Na under varying degree of influence from macromolecules, diffusing, and exchanging ^{23}Na ions in restricted anisotropic motion regimes (Berendsen and Edzes, 1973; Freed, 1968; Eliav and Navon, 1994). Typically, a bi-exponential model is fit to the data, with the fast and slow fractions constrained to a 60/40 ratio corresponding to satellite and central spin transitions (Hubbard, 1970; Madelin et al., 2014).

Fixing the component fractions removes the flexibility to model relative contributions of local motion regimes in the ^{23}Na MR signal. It is well known that in the case of proton MRI, multi-compartment T_2 distributions arise in tissue due to local field interactions between proton nuclei and the microscopic environment (Layton et al., 2013). Similarly, Berendsen and Edzes (1973) observed a strong influence of molecular order present in the tissue sample and the diffusion of sodium ions between different compartments of the averaged quadrupolar interactions. Further, it is incorrect to attribute two components obtained from bi-exponentially relaxing spins in a single ^{23}Na compartment to 'free' and 'bound' components of ^{23}Na ions (Berendsen and Edzes, 1973).

Recently, our group presented the 3D-MERINA sequence for efficient multi-echo acquisition, and proposed a bi-exponential mixture (BEM) approach to fitting the decay model (Blunck et al., 2018). The BEM approach is a two-step procedure, firstly fitting a BE model, again constrained to the 60/40 ratio in brain tissue, and secondly replacing the BE with a mono-exponential (ME) fit in regions found to be implausible for a two-component BE fit, namely CSF. Both the BE and BEM approaches result in parameter maps that fail to clearly differentiate between white matter (WM) and gray matter (GM), and suffer from a low contrast, noisy, speckled appearance.

In this thesis, rather than constraining the bi-exponential decay model to maintain the 60/40 ratio between fast and slow decay components, we employ a continuum model of T_2 decay, based on the premise that sodium exists in the brain in heterogeneous states within localised environments. Our approach makes three key contributions to ^{23}Na-MRI parameter mapping: 1) The continuum model produces T_2 maps with vastly superior tissue contrast; 2) Parameter estimation is a robust one-step procedure that avoids the use of mixture models; 3) Estimates of the fast and slow component fractions are emergent from the inferred continuum model. Indeed, our in vivo human experimental results support the 60/40 split on average in brain tissue, while permitting localised variation that offers richer information than the constrained alternative.

3.2 Theory and Methods

3.2.1 Models for Transverse ^{23}Na Decay Signal

Bi-exponential Mixture Model

The Bi-exponential Mixture (BEM) model employed in (Blunck et al., 2018) to obtain two-compartment parameter mapping from multi-echo ^{23}Na decay signal is presented here for the sake of comparison and reference.

The BEM model assumes a two-component exponential decay signal, attributed to quadrupole and central dipole interactions (Hubbard, 1970).

$$M^{BE}(TE;\boldsymbol{\theta}^{\mathrm{BE}}) = M_0 \left[0.6 \exp\left(-\frac{TE}{T^*_{2_{\mathrm{short}}}}\right) + 0.4 \exp\left(-\frac{TE}{T^*_{2_{\mathrm{long}}}}\right)\right], \tag{3.1}$$

where, TE is the echo time, $\boldsymbol{\theta}^{\mathrm{BE}} = \{M_0,\ T^*_{2_{\mathrm{short}}},\ T^*_{2_{\mathrm{long}}}\}$ is the parameter set containing the short and long T_2^* decay parameters and M_0 is the signal at the first echo, TE_0.

In liquid media, short correlation time results in mono-exponential transverse decay, with signal contributions dominated by the central dipole interactions (Hubbard, 1970).

$$M^{ME}(TE;\boldsymbol{\theta}^{\mathrm{ME}}) = M_0 \exp\left(-\frac{TE}{T^*_{2_{\mathrm{long}}}}\right), \tag{3.2}$$
$$\boldsymbol{\theta}^{\mathrm{ME}} = \{M_0,\ T^*_{2_{\mathrm{long}}}\}.$$

The procedure employed in (Blunck et al., 2018) to apply the BEM model is to first fit a voxelwise BE model, followed by a plausibility check to ensure that both $T^*_{2_{\mathrm{short}}}$ and $T^*_{2_{\mathrm{long}}}$ lie in an acceptable region determined by previously reported values in literature. Voxels that fail the plausibility check are classified as CSF

and a ME model is fit in order to estimate $T^*_{2_{\text{long}}}$.

Proposed Continuum Model

We posit that the voxelwise observation of the T_2^*-weighted sodium signal decay is well described by a weighted continuum of components described by a gamma (GA) distribution, modelling inhomogeneity in the molecular environment. The measured signal at the echo time, TE, is given by the integration of the signal components,

$$M^{GA}(TE, R_2^*) = M_0 \int e^{-TE/R_2^*}\, p(R_2^*)\, dR_2^* \tag{3.3}$$

where $p(R_2^*)$ is the distribution of the relaxation rates. Our continuous distribution model assumes that the random variable, R_2^*, admits a gamma distribution with shape parameter, k, and scale parameter, ζ.

$$p(R_2^*, k, \zeta) = \frac{1}{\zeta^k \Gamma(k)} R_2^{*k-1} e^{-R_2^*/\zeta}. \tag{3.4}$$

Conveniently, T_2^* is characterized by an equivalent inverse gamma distribution, $T_2^* \sim \text{Inv-Gamma}(k, \zeta)$. The gamma distribution is selected for its ability to describe a wide range of relaxation rate profiles, positive support (defined only for $R_2^* > 0$), a simple analytic expression for the mean value, and the important fact that it makes the integration in (3.3) tractable, leading to a closed-form expression for the R_2^* distribution model:

$$M^{GA}(TE; \boldsymbol{\theta}^{\text{GA}}) = (1 + \zeta\, TE)^{-k}, \tag{3.5}$$

where $\boldsymbol{\theta}^{\text{GA}} = \{M_0,\ \zeta, ; k\}$. The mean, $R^*_{2_{GA}} = k\zeta$ and variance, $\nu = k\zeta^2$, of the gamma distribution provide estimates of the location and spread of the relaxation rates. The parameter, $T^*_{2_{GA}}$, defined as the reciprocal of the mean rate, $R^*_{2_{GA}}$, is indicative of the mean T_2^* value in each voxel.

Fast Fraction: We define the fast component fraction, f_{fast}, to be the area under the T_2^* probability density function (pdf) up to a threshold value, $T^*_{2\,\text{th}}$.

$$f_{\text{fast}} = \int_0^{T^*_{2\,\text{th}}} p(T_2^*)\, dT_2^*. \tag{3.6}$$

Here, we select $T^*_{2\,\text{th}} = 15$ ms based on the range of fast T_2^* component values in tissue previously reported in the literature (Madelin et al., 2014). In contrast to fixed 60/40 split of T_2^* fast and slow components in the BEM model, the parameter, f_{fast} varies in the range (0-1), conflating the relative contribution of the continuum of fast components below 15ms.

3.2.2 MRI Experiments

All imaging was performed on a research 7T MRI scanner (Siemens Healthcare, Erlangen, Germany) equipped with a transmit/receive dual-tuned ^{1}H-^{23}Na head coil

(QED, USA), using the 3D-MERINA acquisition protocol (Blunck et al., 2018), which is a 3D radial multiecho acquisition scheme for acquiring sodium MRI signal. To study ^{23}Na relaxation times across different media and ^{23}Na concentrations, a sodium phantom, as described in (Blunck et al., 2018), was imaged using the 3D-MERINA with a total acquisition time of 26 min 40 s. Briefly, the phantom consisted for 16 tightly packed glass tubes, each having a 3cm diameter, and filled with a mixture of saline (30, 70, 110, and 150 mM concentration) and agar (0%, 1%, 3%, and 6%). ^{23}Na MRI was also performed on four healthy volunteers using the 3D-MERINA protocol. All human imaging was conducted with the approval of the University of Melbourne Human Research Ethics Committee, and volunteers gave an informed consent prior to the experiment. For both phantom and in vivo experiments, parameters were set to repetition time $TR = 160$ ms, initial echo time, $TE_1 = 400\mu$s, sampling duration, $T_{RO} = 2$ms, 38 echoes, FOV = 20cm, 3.1 mm isotropic resolution with N=10,000 projections.

Additional proton MRI images were acquired for each human subject. A ^{1}H-FLASH image was obtained with TR = 11 ms, TE=3.06 ms, 14^o flip angle, 1mm isotropic resolution. Brain tissue segmentation was based on a 1H-MP2RAGE image acquired at inversion times 700 and 2700 ms, with 5^o and 6^o flip angles, TR=4900 ms, TE=2.94 ms, GRAPPA factor 4, 0.9mm isotropic resolution and acquisition time 6 min. ^{1}H-MP2RAGE were imaged using a 32- channel head coil (Nova Medical Inc., Wilmington MA, USA) in a separate imaging session. Tissue segmentation was carried out on ^{1}H-weighted acquisitions. The processing pipeline was done in FMRIB Software Library v.5.x (Oxford, U.K.) (Jenkinson et al., 2012) and involved three main steps: 1) Brain extraction on the FLASH image, 2) registration of brain mask onto MP2RAGE image and tissue segmentation (CSF, gray matter, white matter) of masked MP2RAGE, and 3) registration of segmented brain regions via the FLASH image onto the ^{23}Na image.

3.2.3 Parameter Estimation

The estimation of gamma distribution parameters was performed on magnitude images. It is well known that noise in real and imaginary parts of the complex MRI data is described by zero-mean Gaussian distribution. However, application of the nonlinear transformation on complex data to obtain magnitude images alters the noise distribution, leading to Rician distributed noise in the foreground (signal) region and Rayleigh distributed noise in the background (no signal) region.

The Rician probability distribution is defined as

$$p_{Rice}(x; M^i, \sigma) = \frac{x}{\sigma^2} e^{-(x^2 + M^{i\,2})/2\sigma^2} I_0\left(\frac{xM^i}{\sigma^2}\right), \tag{3.7}$$

where I_0 is the Bessel function of the first kind, M^i is the signal model, $i \in \{\text{ME, BE, GA}\}$ and σ^2 is the variance of the Gaussian noise in complex data. In

the absence of signal, $M^i = 0$, resulting in the Rayleigh noise distribution,

$$p_{Rayleigh}(x;\sigma) = \frac{x}{\sigma^2} e^{-x^2/2\sigma^2}, \tag{3.8}$$

with mean, $\mu = \sigma\sqrt{\pi/2}$. The mean of the Rayleigh noise in the background was used to estimate the noise variance, σ^2.

In order to perform parameter estimation, a likelihood function for Rician distribution was constructed for Maximum Likelihood (ML) estimation. Specifically, given the measurements, $\mathbf{y} = [y_1, y_2, ..., y_n]^T$, the likelihood function is

$$f(\mathbf{y}|\boldsymbol{\theta}^i) = \prod_{k=1}^{n} p_{Rice}(y_k|M^i(TE_k;\boldsymbol{\theta}^i), \sigma_n^2), \tag{3.9}$$

where $\boldsymbol{\theta}^i$ is the parameter vector corresponding to the model, M^i, σ_n^2 is the noise variance, n is the total number of echoes, and TE_k, y_k are the k^{th} echo time and measured signal, respectively.

For computational convenience, it is preferable to use the log-likelihood function, defined as

$$\ell\left(\boldsymbol{\theta}^i;\mathbf{y}\right) = \sum_{k=1}^{n} \ln p_{Rice}(y_k|M(TE_k,\boldsymbol{\theta}^i), \sigma_n^2), \tag{3.10}$$

The maximum likelihood estimate of the unknown parameter vector, $\boldsymbol{\theta}^i$, is calculated by maximizing the log-likelihood objective function.

$$\hat{\boldsymbol{\theta}}^i_{MLE} = \arg\max_{\boldsymbol{\theta}^i} \ell\left(\boldsymbol{\theta}^i;\mathbf{y}\right). \tag{3.11}$$

The ML parameter estimation is a non-linear optimization problem. The complete estimation algorithm was implemented in MATLAB and a constrained nonlinear multivariate solver was used to carry out the optimization. The solver was initialized with suitable fixed values to ensure convergence.

3.3 Results

Phantom Data

The ability of the GA model to discriminate between tissues with varying sodium concentration and structural properties was validated by the results of mean T2* estimation in the phantom data (Figure 3.1). The parameters maps obtained through voxel-wise fitting are displayed in (Figure 3.1a). The $T^*_{2_{\mathrm{GA}}}$ map shows clear contrast across vials with varying agarose concentration whilst maintaining constancy along sodium concentration, except at the low concentration of 30mM where the map is more speckled. The noisy estimates at low sodium concentration

indicates the detrimental effects of low SNR on MLE estimation. In comparison, the $T^*_{2_{\text{short}}}$ and $T^*_{2_{\text{long}}}$ maps from the BEM model are more noisy with inferior contrast across vials.

For each phantom vial, the mean estimated $T^*_{2_{\text{GA}}}$ along with the standard deviation showed a clear decreasing trend with increasing agarose concentration (Figure 3.1b). At low sodium concentration of 30mM/I, the $T^*_{2_{\text{GA}}}$ estimates were consistently lower whilst maintaining the decreasing trend observed at higher sodium concentrations. Similarly, the fast fraction was zero in liquid but increased steadily with increasing agarose content, as expected. On the contrary, $T^*_{2_{\text{short}}}$ failed to produce a clear increasing trend across agarose concentration with a higher value at 3% agar than at 6% agar, showing the difficulty of the BEM model in correctly discerning the subtle variations in physical and chemical composition of vial samples.

In liquid vials, the mean $T^*_{2_{\text{GA}}}$ ranged between $36 - 42$ ms across sodium concentration with zero fast fraction, indicating the absence of short T^*_2 components in fluid environments (Figure 3.1b). The decrease in mean $T^*_{2_{\text{GA}}}$ with emerging fast fraction in more solid environments (3-6% agarose) showed a predominantly short T^*_2 component population. Instead of fixed 60/40 split employed in the BEM model, the GA model allowed the fast fraction to vary, thus capturing the effects of localised heterogeneous micro-environments on the sodium decay signal.

In vivo Data

For each subject, voxel-wise data from each slice was well fit by the GA model, with distinct T^*_2 inverse gamma pdfs obtained in WM, GM and CSF regions of the brain (see Figure 3.2 for an example of single voxel fits in axial slice 36 of subject 1). For these voxels, the mean T^*_2 values estimated in WM and GM voxels were 1ms and 8.5ms, respectively. However, a higher mean T^*_2 value of 27ms was estimated in the CSF voxel, as expected. Similarly, the fast fraction in these voxels was estimated at 0.83, 0.61 and 0 in WM, GM and CSF, respectively, indicating differing structural composition in different tissue types.

For all four subjects, the parameter maps generated from the application of BEM and GA models to the experimental sodium MRI data demonstrated the ability of the GA model to provide better contrast in brain tissue regions, as follows. Along with distinguishing CSF regions from soft tissue, the $T^*_{2_{\text{GA}}}$ map discerns WM and GM structures, leading to superior contrast with enhanced SNR (Figure 3.3). Generally, the WM appears darker than the GM, with slightly lower $T^*_{2_{\text{GA}}}$ values. The fast fraction maps (Figure 3.4) provide contrast with enhanced boundaries between different tissue types. In WM regions, the fast fraction was generally higher than GM regions, while it was zero in CSF region, as expected. In comparison, $T^*_{2_{\text{short}}}$ and $T^*_{2_{\text{long}}}$ maps (Figures 3.5-3.6) show clear boundaries between CSF and tissue, but fail to provide meaningful inter-tissue contrast. Specifically, the $T^*_{2_{\text{short}}}$ map (Figure 3.6) is extremely noisy in tissue with $T^*_{2\,\text{long}}$ varying randomly

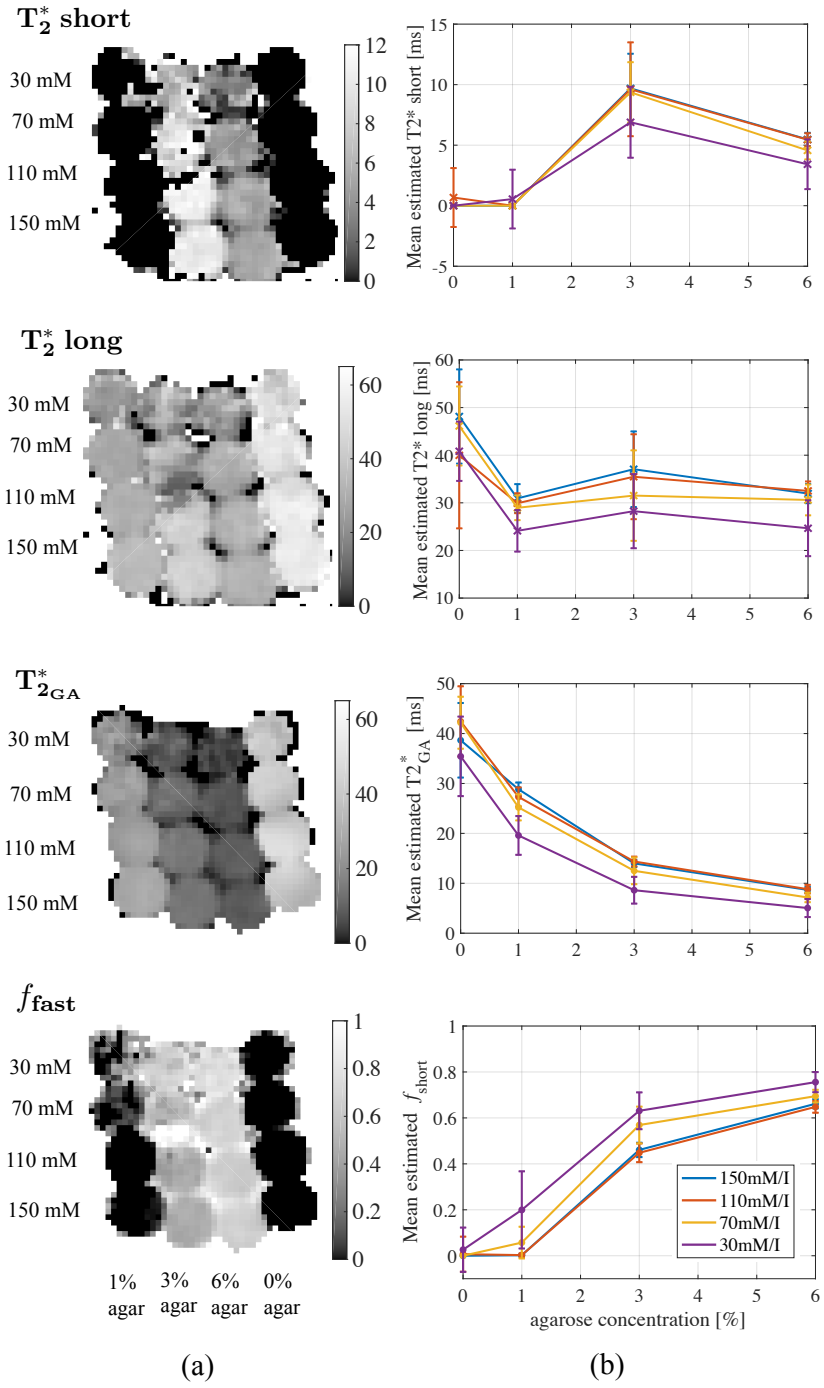

Figure 3.1: (a) Parameter maps of BEM and GA models in phantom vials. (b) Parameter estimates (mean ± s.d.) across agar concentration for different ^{23}Na concentrations. $T^*_{2_{\mathrm{GA}}}$ maps clearly delineate different media. Unlike BEM relaxation parameters, mean $T^*_{2_{\mathrm{GA}}}$ monotonically decreases with increasing agar concentration.

from voxel to voxel.

Information in continuum model parameters

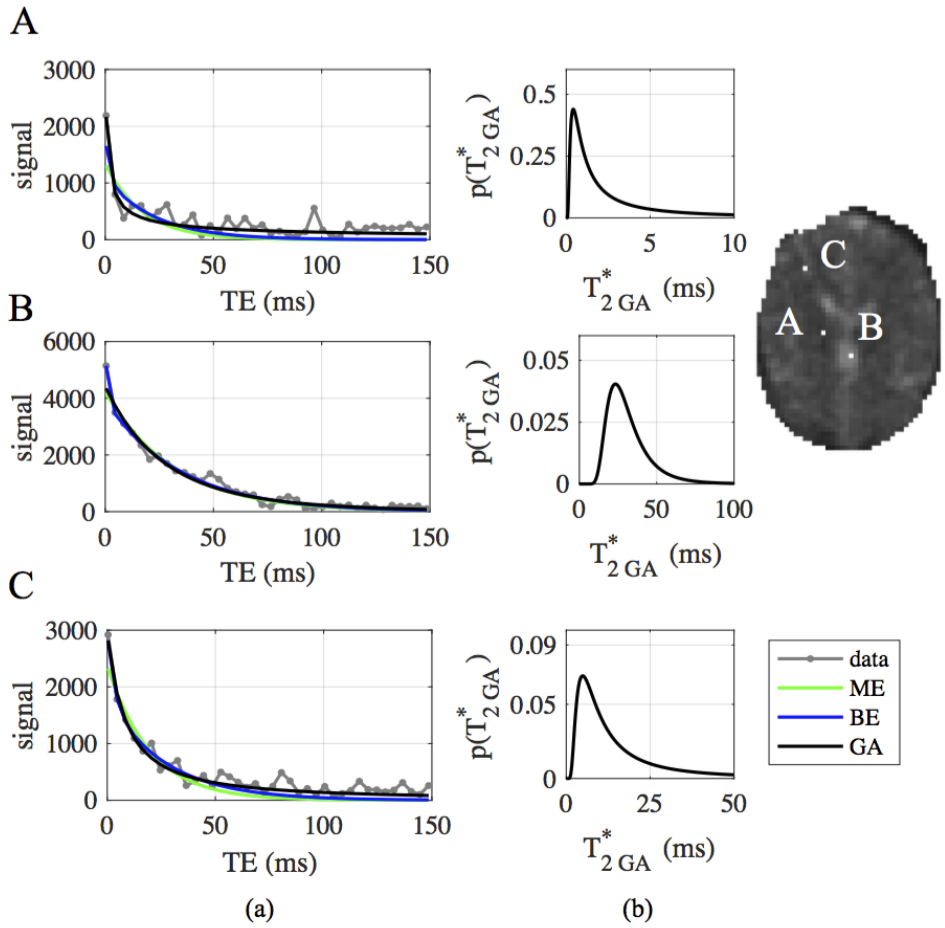

Figure 3.2: (a) Single voxel data (gray), overlaid with curve-fits from ME (green), BE (blue) and GA(black) models, and (b) corresponding gamma pdfs in A) WM, B) CSF and C) GM.

ML estimation results were used to empirically obtain the probability distributions of $T^*_{2\,\mathrm{GA}}$ in WM, GM and CSF through histogram normalization. Figure 3.7a displays the resulting $T^*_{2\,\mathrm{GA}}$ distributions for subject 1. $T^*_{2\,\mathrm{GA}}$ in CSF showed a flat distribution ranging between 20-60 ms, with a few voxels below 20 ms due to partial volume effects in low resolution sodium MRI data. In comparison, $T^*_{2\,\mathrm{GA}}$ in WM and GM regions demonstrated peaked distributions with WM having a lower peak (5ms) than GM (7ms), indicating the efficacy of the GA model in discerning subtle T^*_2 variations across different tissue types.

The empirical probability distributions of fast fraction, f_{fast}, estimated from the GA model estimates provide evidence of the ability of the GA model to capture variations in the volume fractions of short and long T2* components in tissue micro-environments (Figure 3.7b). The absence of $T^*_{2\,\mathrm{short}}$ component in CSF was revealed by zero f_{fast}, except in voxels with partial volume effects. The mean value of f_{fast} was 0.02 ± 0.07 in CSF, 0.41 ± 0.22 in GM and 0.53 ± 0.21 in WM.

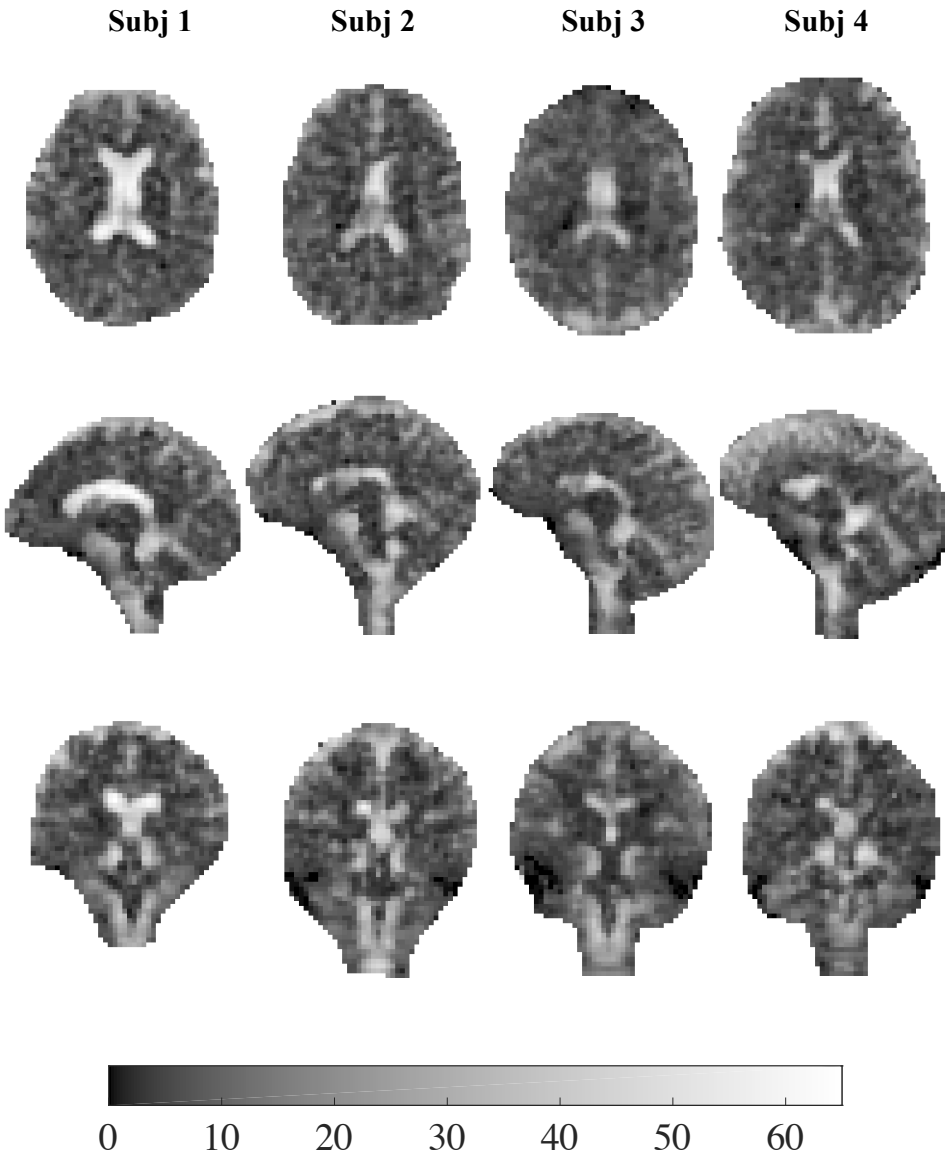

Figure 3.3: Parameter maps of $T^*_{2_{\mathrm{GA}}}$, estimated from the GA model.

Even though the empirical pdfs in WM and GM overlapped, the utility of f_{fast} in discriminating WM and GM regions was demonstrated by separated peaks (0.68 in GM and 0.73 in WM).

Probabilistic masks of the white matter, computed from the proton MP2RAGE images and processed using FSL FAST, are shown in Figure 3.8. For comparison, the white matter masks computed from the sodium MRI data via thresholding of f_{fast} are shown in the bottom row. While there is overall agreement between the modalities, the low SNR of sodium obscures the detail in the f_{fast} maps.

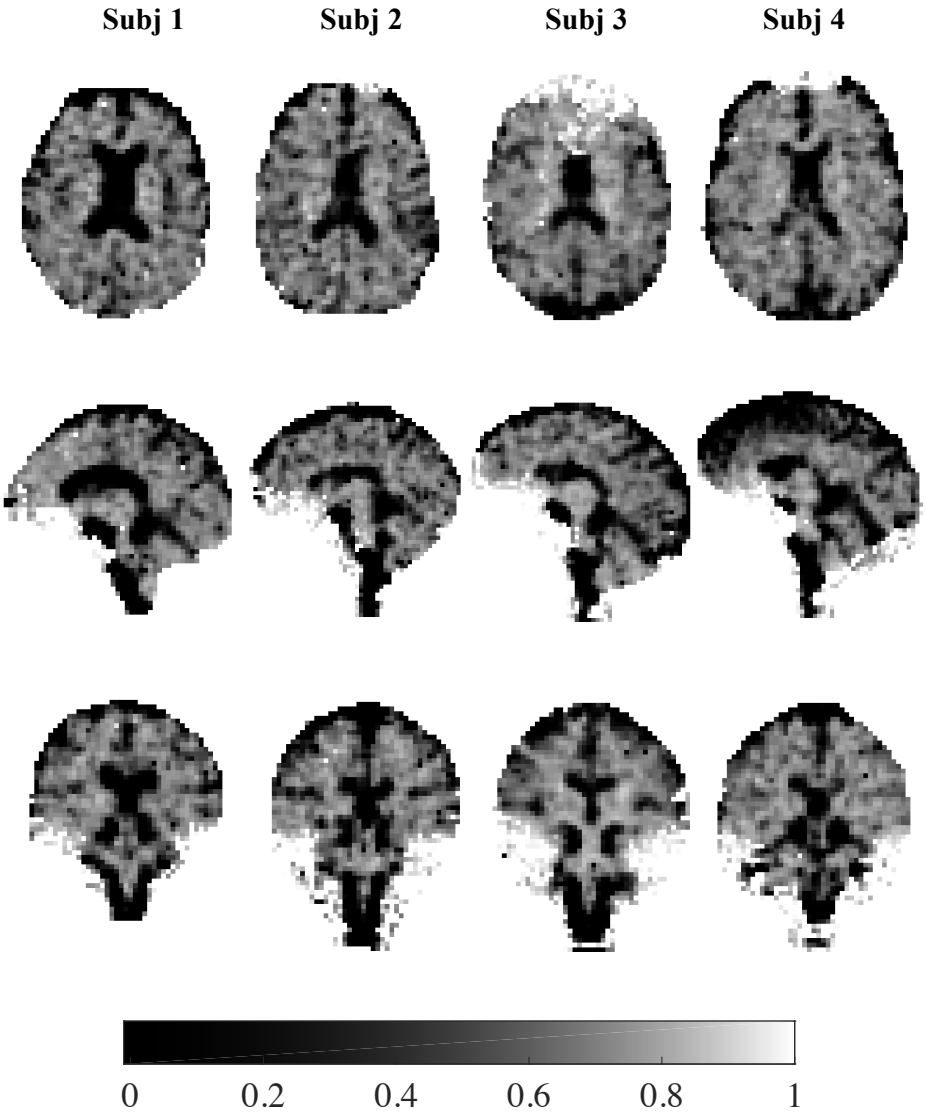

Figure 3.4: Parameter maps of fast fraction, f_{fast}, calculated from the GA model.

3.4 Discussion

We have demonstrated that the continuum distribution gamma model is able to account for the effects of tissue complexity on the transverse decay of quadrupolar ^{23}Na spins. The gamma model provides parameter maps with superior contrast than the commonly employed bi-exponential model. Further, the fast T_2^* fraction provides additional insight into the underlying tissue environment, and offers potential for better quantification of the intra- and extra-cellular ^{23}Na contributions to the decay signal.

Parameter mapping in sodium MRI data is challenging due to inherently low SNR and spatial resolution, prompting the need to employ robust models and estimation techniques. Existing approaches typically use a bi-exponential model or a

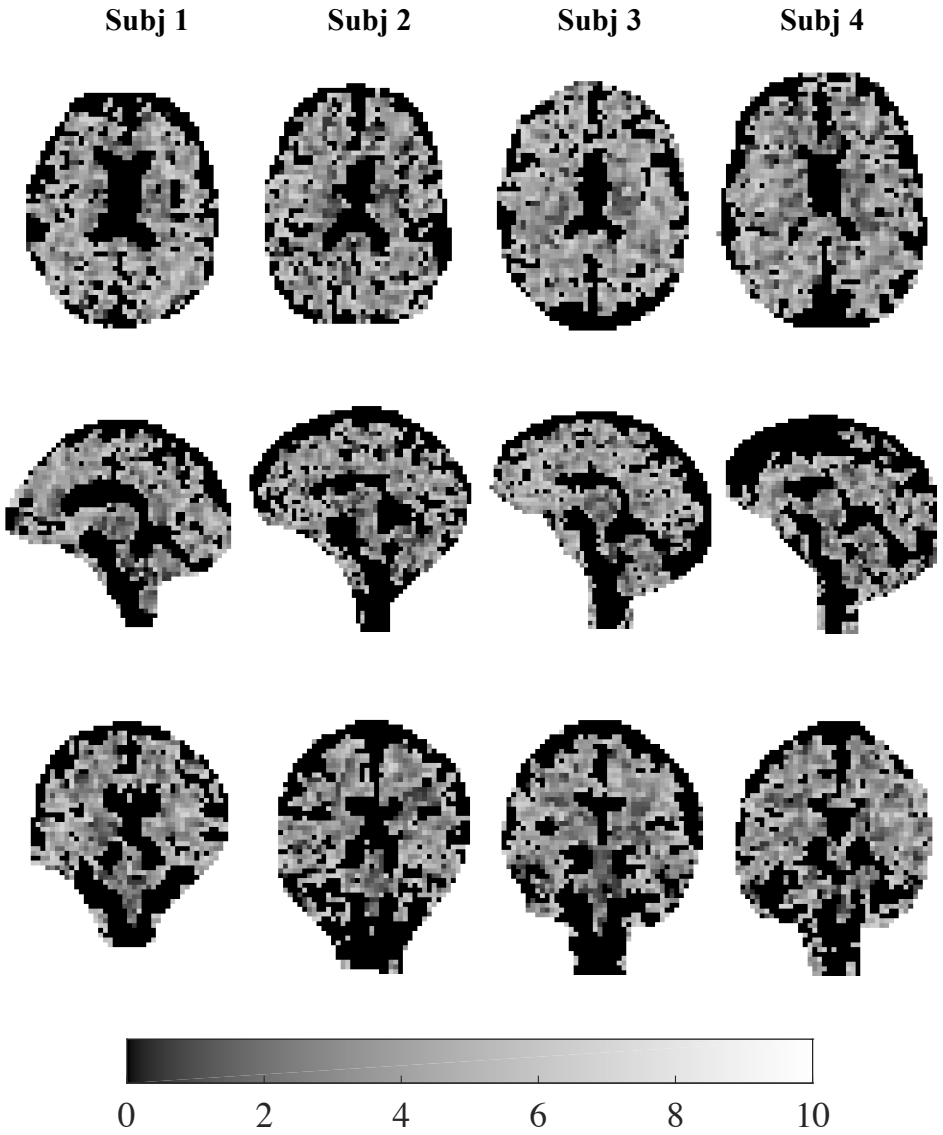

Figure 3.5: Parameter maps of $T^*_{2_{\text{short}}}$, estimated from the BEM model.

variant thereof to characterise two-component transverse relaxation sodium decay signal. Parameter estimation from bi-exponential models is well-known to be difficult (Celik et al., 2013), and when coupled with the low SNR and poor spatial resolution of sodium MRI data, the application of bi-exponential models become problematic, producing noisier and less informative parameter maps in tissue regions. We have proposed a continuous distribution model, under the assumption that local interactions of the quadrupolar ^{23}Na spins with surrounding cellular structures lead to a continuum of components, each characterised by a distinct T_2^*. Assuming a gamma distribution of T_2^* components, we have derived a closed-form model that gives rise to intuitively meaningful parameters, the mean T_2^* arising from the mean of the gamma distribution, and the fast T_2^* component fraction obtained through integrating the contributions of all T_2^* components be-

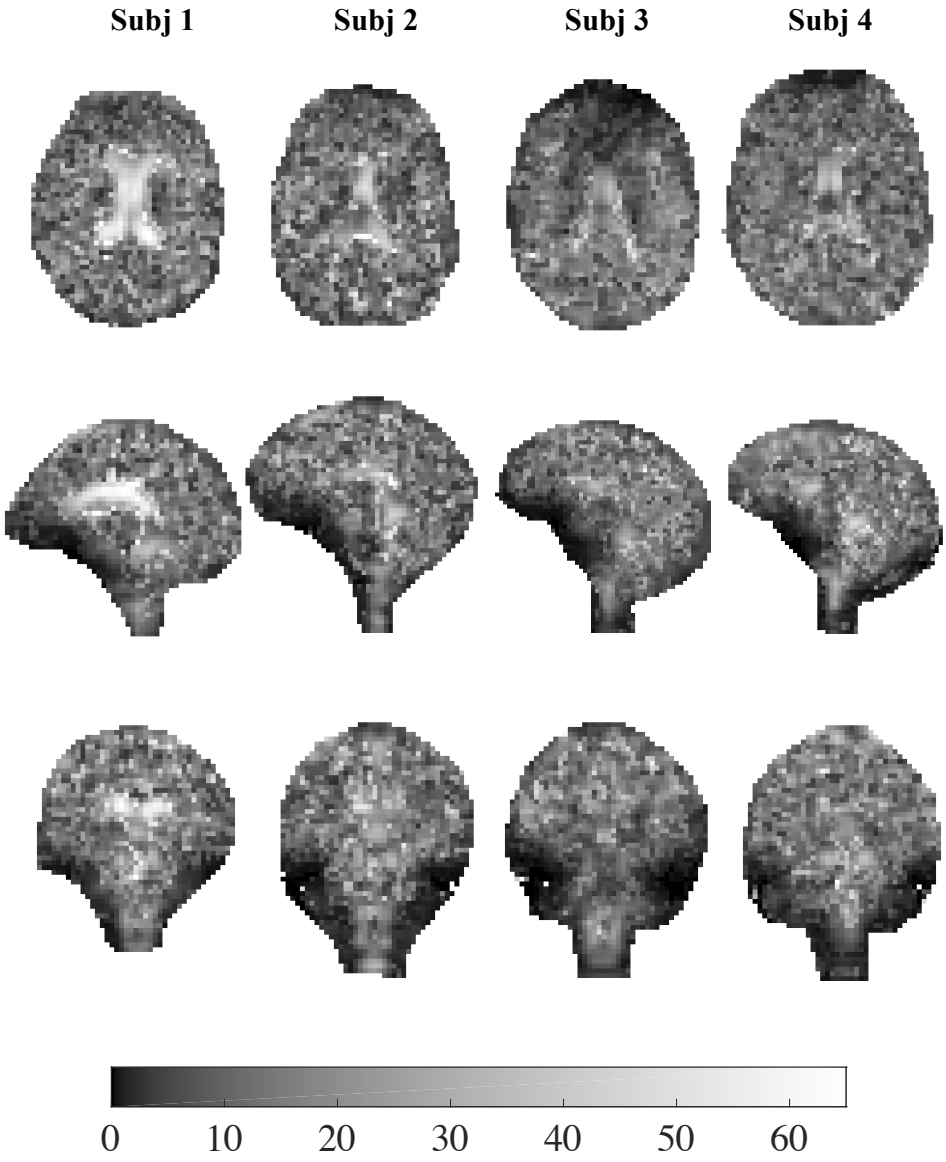

Figure 3.6: Parameter maps of $T^*_{2_{\text{long}}}$, estimated from the BEM model.

low the threshold value of 15 ms.

In liquid media, such as CSF, the ^{23}Na signal is known to comprise of only a long T_2^* component, giving rise to mono-exponential transverse relaxation decay. Bi-exponential models, such as the one employed in the MERINA protocol, assume definite presence of two separate T_2^* components, thereby failing to provide plausible parameter estimates in CSF and necessitating the a two-step estimation technique (Blunck et al., 2018). The continuum distribution model overcomes this drawback by replacing the rigid two-component assumption with the presence of a continuum of components described by a probability distribution. The additional flexibility offered by the gamma distribution in characterising a wide range of T_2^*

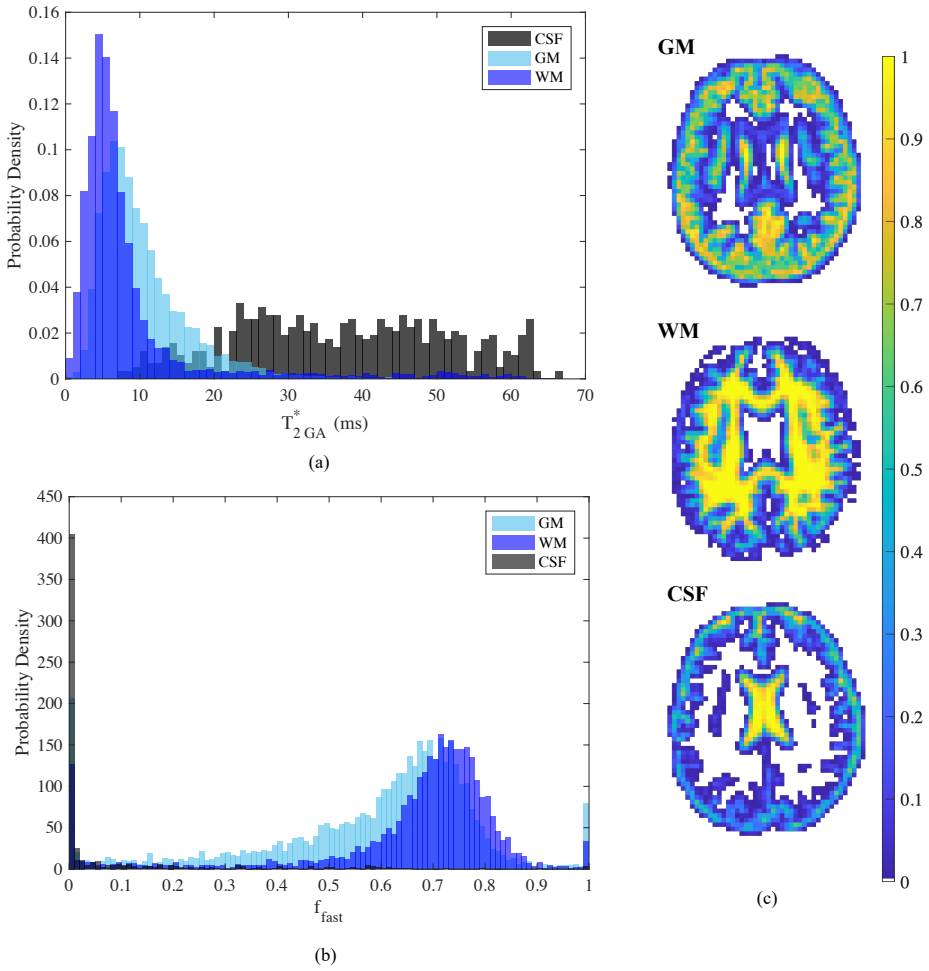

Figure 3.7: (a) Empirical pdf of $T^*_{2_{GA}}$ from voxelwise estimation of the gamma distribution in CSF (black), GM (cyan) and WM (blue). (b) Empirical pdfs of fast decay fraction, f_{fast}, in CSF (black), GM (cyan) and WM (blue). (c) Exemplar probabilistic GM, WM and CSF masks transformed from proton MP2RAGE data onto sodium MRI data (subject 1.)

distributions allows for a straightforward one-step estimation of the gamma model parameters both in CSF and tissue, alleviating the need to apply any plausibility check, and resulting in quantitative parameter maps with enhanced contrast and visual information.

The continuum of components concept has previously been explored in the interpretation of proton MRI data. For instance, the NNLS method (Whittall and MacKay, 1989) divides the T_2 parameter space into a pseudo-continuous grid and employs a regularised non-negative linear least squares algorithm to estimate a discretised T_2 distribution. On the same principle, Layton et al. (2013) proposed an inverse gamma mixture model to estimate the width of T_2 modes in multi-echo T^2-weighted proton MRI data. Similarly, continuous gamma distribution models have been used to describe the distributions of Apparent Diffusion Coefficient

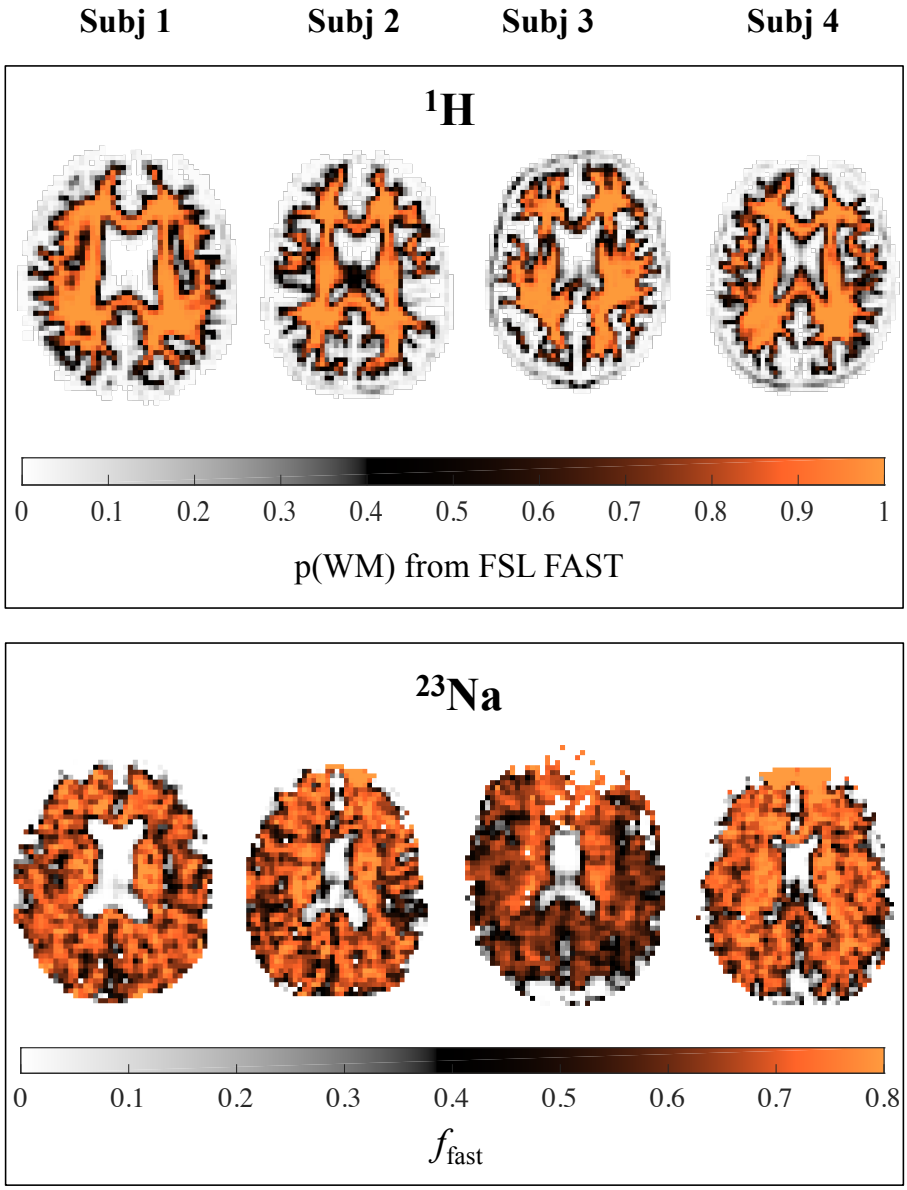

Figure 3.8: White matter masks computed from proton MRI images and FSL FAST (top row) and f_{fast} map in sodium MRI data.

(ADC) (Yablonskiy et al., 2003; Scherrer et al., 2016) and Axon Diameter (Assaf et al., 2008) in diffusion MRI data. (See Chapter 4 for a description of ADC and axon diameter density models).

3.5 Conclusion

We have proposed a continuous distribution model for characterizing transverse relaxation decay in ^{23}Na MRI signal. We have demonstrated that the gamma distribution model outperforms the bi-exponential mixture model in terms of ease

of implementation, visual information and contrast. Furthermore, the gamma model provides robust parameter mapping with more pronounced structural details. Given the flexibility offered by the gamma distribution model in characterizing a wide range of T_2^* component distributions and superior estimation performance under low SNR and large partial volume effects, we recommend use of the gamma distribution model for the interpretation of ^{23}Na-MRI data.

CHAPTER
FOUR

Compartment Modelling in Diffusion Weighted Imaging

4.1 Introduction

Free diffusion of water in diffusion-weighted MRI (DW-MRI) is characterized by a single diffusion coefficient and gives rise to an exponential signal decay across b-values, equivalent to a Gaussian decay process across q-space. In biological tissue, complex intra- and extra-cellular spaces present barriers to the movement of water molecules, causing hindered or restricted water diffusion, which is well-known to lead to non-exponential signal decay (Beaulieu, 2002). The apparent diffusion coefficient (ADC) is a measure of diffusivity that takes into account the effects of interactions with surrounding cellular environment while still employing a Gaussian decay model of the DW-MRI signal.

It is widely accepted that there is a need for accurate models of non-exponentially decaying DW-MRI data. The commonly used bi-exponential model (Niendorf et al., 1996) contains two discrete ADC values, often attributed to hindered and restricted compartments. Beyond the linear combination of discrete ADC values, the general statistical model proposed by Yablonskiy et al. considers a continuous distribution of ADC values, attributed to complex tissue microarchitecture that results in a continuum of diffusion compartments each with a distinct ADC (Yablonskiy et al., 2003). This continuum idea was exploited in a gamma distribution model of the ADC (Johnston et al., 2011), used to describe restricted diffusion in white matter. Most recently, the gamma distribution model was applied to model the diffusion profiles of normal and cancerous prostate tissues (Oshio et al., 2014). The gamma distribution model is advantageous as an ADC distribution, as it integrates to an analytic signal decay model.

Geometric properties of the cellular microenvironment have a direct influence on ADC. Spins diffusing inside confined spaces, such as axons, experience restricted motion which leads to decreased diffusivity. This phenomenon suggests the potential of sensitizing DW-MRI signal for morphometric inference of underlying microstructure. The axon diameter distribution (ADD) of fibre bundles within the white matter of the central nervous system (CNS) is an important biomarker of nerve function (Ritchie, 1982), providing useful insight into its structural and functional aspects. Neuronal pathways with faster response time tend to have axons of larger radii while slower response time pathways are known to possess axons with smaller radii (Hursh, 1939; Waxman, 1980; Tasaki et al., 1943). The nerve conduction velocity, determined by its axon diameter, impacts the process of temporal summation in neurons. Further, the ADD plays a crucial role in determining the extent of downstream synaptic branching and current magnitude in neuronal pathways (Salinas, 2005). Hence, ADD inference is a potential tool for gaining insights into normal and abnormal development in the central and peripheral nervous systems. Highly localised ADD estimates have the potential to guide WM tractography and segmentation algorithms for brain connectivity analysis applications. It has been shown that certain neuronal pathologies cause axonal damage, such as shrinkage or swelling and alter the shape and size of the ADD: morphometric studies of sensory nerve biopsies of patients with amyotrophic lat-

eral sclerosis showed evidence of preferential damage to larger myelinated axons (Heads et al., 1991), while smaller axons are underdeveloped in autism (Piven et al., 1997).

At a microscopic level, brain white matter is a complex heterogeneous structure with axons ordered in fascicles surrounded by an extra-axonal region consisting of various glial cells such as astrocytes and oligodendrocytes (Assaf et al., 2008). The structure of white matter suggests multi-compartment models of the diffusion signal (Stanisz et al., 1997). In recent years, this has been simplified to two- or three-component models in which intra-axonal diffusion follows a parametric decay governed by axonal cylindrical geometry, tortuous extra-cellular diffusion follows a Gaussian decay defined by an ADC, and signal decay in cerebrospinal fluid is freely Gaussian. Assaf et al. (2004) termed the two former components 'restricted' and 'hindered', respectively, and proposed the model's use in multi-gradient direction, single b-value acquisitions for inference of 3-d white matter structure (CHARMED). The ball-and-stick model (Behrens et al., 2003) considers unidirectional diffusion within zero radius axons along the principle axis and isotropic diffusion in extra-axonal space to resolve multi fibre orientation within a single voxel. In later work, Assaf et al. (2008) exploited the fact that nerve fibre ADD's can be well-modelled by gamma distributions to derive AxCaliber, a method for inferring ADD's from experimental data. AxCaliber applies a single diffusion gradient and imaging plane perpendicular to the desired fibre bundle direction, and acquires data over multiple gradient and timing parameters, under the short gradient pulse (SGP) approximation (i.e. diffusion gradients are turned on for a very short duration) (Assaf et al., 2008). The initial ex-vivo demonstration of AxCaliber was followed by in-vivo rat brain application with the addition of a CSF compartment in the model (Barazany et al., 2009).

The three compartment model introduced by Stanisz et al. (1997) models prolate ellipsoidal axons and spherical glial cells, each with partially permeable membranes. Water exchange through these membranes is permitted. In an attempt to recover mean axon radius in brain white matter in vivo, Alexander (2008) suggests a simplification of CHARMED that considers cylindrical axons with a single radius aligned with extra-axonal principle axis. To develop a method for orientationally invariant estimation of axon diameter and density, Alexander et al. (2010) created ActiveAx, a four-compartment model with the two compartments from (Alexander, 2008), a CSF compartment with isotropic diffusion and a compartment composed of almost stationary water molecules representing subcellular structures such as the glial cells. These studies demonstrate that experimental set-up and pulse gradient magnitudes, durations and timings significantly impact ADD inference. Wenjin et al. (2010) used low-q angular double pulsed gradient spin echo (double-PGSE) MRI for estimating microstructural tissue properties without prior knowledge of axon orientation. A technique employing 3-d double-PGSE MRI was used to perform axon diameter mapping in porcine spinal cord (Komlosh et al., 2013). The majority of these methods acquire data under SGP

approximation to prevent phase accumulation during the application of the gradients (see Section 2.3 for details), with the exception of CHARMED that includes both acquisition classes (i.e. with and without SGP approximation).

It remains an open question as to how robustly these models can be fit to experimental DW-MRI data and how close to reality the parameter estimates are. Robustness of model parameter estimates can be quantified by carrying out Crámer Rao lower bound (CRLB) analysis, a well-used statistical tool in signal processing (Thomas and Cover, 1991) that has previously been applied in a number of DW-MRI studies (Jones et al., 1996; Brihuega-Moreno et al., 2003). The CRLB provides a lower bound on the variance of an estimator and thus provides uncertainty levels for model parameter estimates. We compare the robustness of ADC models by performing a CRLB analysis to determine the lower bound on the variance incurred by the model estimators, followed by application to experimental DW-MRI data of ovine optic nerve and rat brain. We demonstrate that both the bi-exponential and gamma distribution models are highly susceptible to variations in parameter estimates at the typical gradient strengths of clinical scanners, and must be treated with caution even at the gradient strengths of pre-clinical scanners. Further, variations in estimated ADC potentially lead to variations in the geometrical description of the tissue provided by the ADD models, which may result in ADD estimates that are far from reality. Therefore, the need for a validation framework for ADD model estimates arises.

An advantageous aspect of ADD estimation is the ability independently validate by means of bright-field microscopy. Using ground-truth information from electron microscopy data, we demonstrate that two-component models fail to correctly infer ADD from DW-MRI data. We do this by first showing that diffusion signals from axons of varying radii are indistinguishable under the SGP, in agreement with recent work that showed the high variance incurred by ADD estimators using a Cramer Rao lower bound analysis (Mesri et al., 2014). In order to achieve maximal information spread over axon diameters, we employ long gradient pulses, one of the categories in the original CHARMED framework Assaf and Basser (2005). Long gradient pulses achieve a secondary purpose of nulling the hindered extra-cellular component for even small gradient values, as used in the derivation of the Apparent Fibre Density statistical method (Raffelt et al., 2012) for the analysis of human diffusion MRI data. We compare the estimated ADD of an ovine optic nerve to the empirical ADD obtained through bright-field microscopy, and demonstrate significant differences between the two ADDs, indicating the model is not rich enough to encapsulate all the information contained in the observed measurements.

4.2 Models of the Diffusion Weighted Signal

Our theoretical analysis assumes that the data is acquired using the standard pulsed gradient spin echo (PGSE) diffusion weighted imaging sequence, as is em-

ployed in acquisition of the experimental results. Let $E(q)$ be the normalised diffusion signal attenuation from a tissue component with a characteristic ADC, D ($\mu m^2/ms$). The q-value, $q = \gamma g \delta/(2\pi)$ (μm^{-1}), γ is the gyromagnetic ratio, g (mT/m) is the diffusion gradient magnitude and δ (ms) is the gradient pulse duration. The b-value, $b = 4\pi^2 q^2 (\Delta - \delta/3)$, is in $ms/\mu m^2$, where Δ (ms) is the duration between the two gradient pulses.

Exponential Model: Under free diffusion, the diffusion signal is Gaussian in q (exponential in b),

$$E(q, D) = \exp(-4\pi^2 q^2 (\Delta - \delta/3) D). \tag{4.1}$$

The Bi-Exponential Model assumes the signal to be composed of two separate components, often attributed to fast and slow components, or restricted and hindered diffusion in geometrically complex cellular structures,

$$E(q) = f E_r(q) + (1 - f) E_h(q), \quad 0 \leq f \leq 1, \tag{4.2}$$

where f is restricted volume fraction, E_r is the normalised restricted signal decay, and E_h is the normalised hindered signal decay (Niendorf et al., 1996). Each component follows the Gaussian ADC model in (4.1).

The Gamma Distribution Model assumes that the ADC follows a gamma distribution, $p(D)$, with rate parameter, k, and scale parameter, θ,

$$p(D) = \frac{1}{\theta^k \Gamma(k)} D^{k-1} \exp\left(-\frac{D}{\theta}\right), \tag{4.3}$$

where Γ is the gamma function (Abramowitz and Stegun, 1964). The continuum decay model can be analytically derived by integration of the signal decay over $p(D)$,

$$\begin{aligned} E(q) &= \int \Big(- 4\pi^2 q^2 (\Delta - \delta/3) D \Big) p(D) \, dD \\ &= \big(1 + 4\pi^2 q^2 (\Delta - \delta/3) \theta\big)^{-k}. \end{aligned} \tag{4.4}$$

4.2.1 Two-Compartment Models of ADD

The restricted diffusion component of the bi-exponential ADC model (6.2) suggests the presence of physical boundaries restricting the motions of diffusion spins. The two-compartment ADD model attributes the restricted component to the diffusion of spins inside cellular structures, such as axons and relates the restricted compartment to the geometry of the underlying tissue. In this section, we describe two such existing models and develop a novel model of ADD distribution under the assumption of long gradient pulses.

4.2.2 Composite Hindered and Restricted Model of Diffusion (CHARMED)

CHARMED describes anisotropic water diffusion in brain white matter (Assaf et al., 2004). This model divides the brain white matter into two isolated compartments (Figure 4.1); a hindered extra-axonal compartment consisting of astrocytes, glia, and extracellular matrix, and a restricted intra-axonal compartment. Diffusion in the hindered compartment is characterised by a 2D Gaussian displacement distribution, while the geometry of the restricted compartment characterizes the intra-axonal restricted diffusion. The hindered compartment contributes towards signal attenuation at low b-values, while the effects of non-Gaussian restricted diffusion in the restricted components become more apparent at high b-values.

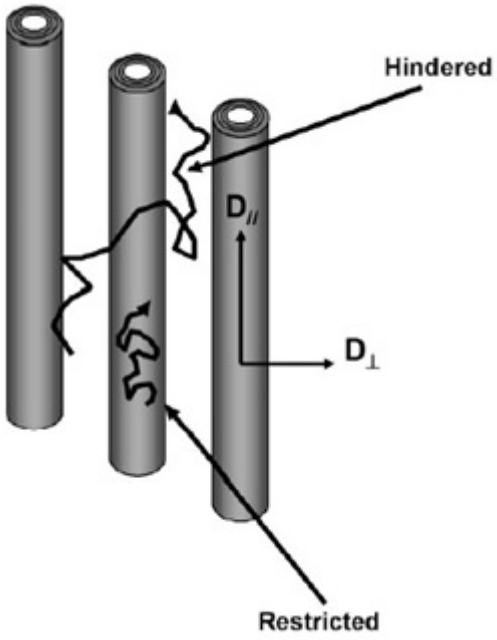

Figure 4.1: Two compartment model for extra and intra-axonal hindered and restricted diffusion. Water molecules diffuse both within and outside axons (Assaf et al., 2004).

Under slow exchange limit (i.e. slow exchange of water molecules between compartments) the measured DW-MRI signal is modelled as the weighted sum of contributions from the hindered and restricted diffusion compartments (Assaf et al., 2000)

$$E(\mathbf{q}, \Delta) = f_h E_h(\mathbf{q}, \Delta) + f_r E_r(\mathbf{q}, \Delta), \tag{4.5}$$

where f_h and f_r are the T2-weighted volume fractions of the hindered and restricted compartments and $f_r + f_h = 1$. Δ is the diffusion time, and $E_h(\mathbf{q}, \Delta)$ and $E_r(\mathbf{q}, \Delta)$ are the normalized MR echo signals from the hindered and restricted

compartments, respectively (Assaf et al., 2004).

The relationship between $E_r(\mathbf{q}, \Delta)$ and the average propagator, $P_s(\mathbf{R}, \Delta)$, at diffusion time, Δ is given by (Callaghan, 1993; Kärger et al., 1988)

$$E_r(\mathbf{q}, \Delta) = \iiint P_s(\mathbf{R}, \Delta) \exp^{2\pi i \mathbf{q}\cdot\mathbf{R}} d\mathbf{R}, \tag{4.6}$$

where $\mathbf{R}$ is the net displacement vector for a spin, and Δ is the diffusion time as previously defined.

It is known that the solution to the diffusion equation in restricted cylinders (Crank, 1975; Robertson, 1966; Neuman, 1974; Codd and Callaghan, 1999) can be represented as products of x-, y-, and z-dependent terms when viewed in the principal coordinate frame of reference. In cylindrical regions, displacement of water molecules in the axial (parallel to the principle axonal axis) and radial (perpendicular to the principle axonal axis) directions are independent of each other. Hence, the average propagator, $P_s(\mathbf{R}, \Delta)$, is expressed as:

$$P_s(\mathbf{R}, \Delta) = P_\perp(\mathbf{R}_\perp, \Delta) P_\parallel(\mathbf{R}_\parallel, \Delta) \tag{4.7}$$

where $P_\perp(\mathbf{R}_\perp, \Delta)$ and $P_\parallel(\mathbf{R}_\parallel, \Delta)$ are the displacement probability propagators for motion of water molecules in the radial and axial directions, respectively. Similarly, the net displacement vector $\mathbf{R}$ and $\mathbf{q}$ can be decomposed into their radial and axial components ($\mathbf{R}_\perp$ and $\mathbf{R}_\parallel$, $\mathbf{q}_\perp$ and $\mathbf{q}_\parallel$).

Statistically independent displacements along the axial and radial directions within axons give rise to an MR signal which is expressed as the product of contributions arising from the respective displacement distributions. MR signal decay arising from motion of water molecules in the radial and axial directions, $E_\perp(\mathbf{q}_\perp)$ and $E_\parallel(\mathbf{q}_\parallel)$, is given as:

$$E_\perp(\mathbf{q}_\perp) = \iint P_\perp(\mathbf{R}_\perp, \Delta) \exp^{2\pi i \mathbf{q}_\perp \mathbf{R}_\perp} d\mathbf{R}_\perp \tag{4.8}$$

and,

$$E_\parallel(\mathbf{q}_\parallel) = \iint P_\parallel(\mathbf{R}_\parallel, \Delta) \exp^{2\pi i \mathbf{q}_\parallel \mathbf{R}_\parallel} d\mathbf{R}_\parallel, \tag{4.9}$$

where

$$E_r(\mathbf{q}, \Delta) = E_\perp(\mathbf{q}_\perp, \Delta) E_\parallel(\mathbf{q}_\parallel, \Delta) \tag{4.10}$$

Codd and Callaghan (1999) calculated the MR signal contribution arising from self diffusion of water molecules in radial direction, $E_\perp(\mathbf{q}_\perp, \Delta)$. However, it should be kept in mind that these expressions are valid only when the narrow pulse approximation holds. Under the assumption that $\delta \sim \Delta$, the asymptotic form

of $E_\perp(\mathbf{q}_\perp, \Delta)$ for restricted diffusion in a cylindrical region under constant field gradient was proposed by Neuman (1974).

$$E_\perp(\mathbf{q}_\perp, \Delta) = \exp^{-\frac{7}{96}\left(\frac{4\pi^2 R^4 |q_\perp|^2}{D_\perp \tau}\right)\left(2-\left(\frac{99}{112}\right)\frac{R^2}{D_\perp \tau}\right)}, \; \Delta = 2\tau \tag{4.11}$$

In the extra-axonal region, the anisotropic self diffusion of water molecules assumed to be hindered in all directions, is represented as a three-dimensional Gaussian displacement distribution characterized by an effective diffusion tensor, $\mathbf{D}$ (Basser et al., 1994a).

$$E_h(\mathbf{q}, \Delta) = \exp^{\left(-4\pi^2\left(\Delta-\frac{\delta}{3}\right)\mathbf{q^T D q}\right)}, \tag{4.12}$$

where $\mathbf{q^T}$ is the matrix transpose of $\mathbf{q}$.

By decomposing $\mathbf{q}$ into its parallel and perpendicular components and assuming that the parallel and perpendicular diffusive motions in the selected frame of reference are statistically independent, the perpendicular hindered component is expressed as

$$E_h(q, \Delta) = \exp^{\left(-4\pi^2\left(\Delta-\frac{\delta}{3}\right)|q_\perp|^2\lambda_\perp^2\right)} \tag{4.13}$$

where $\lambda_\perp$ is the eigenvector of the diffusion tensor in the hindered compartment.

The composite model for the observed MR signal weighted by the diffusive motion of water trapped in extra-axonal and intra-axonal regions is obtained by combining the MR signal contributions from hindered and restricted motion regimes using eq.(4.14).

The description of restricted and hindered diffusion in both axial and radial directions is presented here for completeness. In axons, maximum restriction is observed perpendicular to the principle axonal axis, leading to maximal separation between diffusion signals from axons with varying radii. Therefore, for the purpose of ADD inference, the models presented next consider uni-direction diffusion, i.e. diffusion perpendicular to the principle axonal axis only.

4.2.3 AxCaliber

The two-compartment AcCaliber model considers axons to be geometrically equivalent to tightly packed, impermeable cylinders of varying radii, surrounded by extra-cellular space (Assaf et al., 2004):

$$E(q, \Delta) = fE_r(R, q, \Delta) + (1-f)E_h(q, \Delta), \;\; 0 \leq f \leq 1, \tag{4.14}$$

where f is restricted volume fraction, E_r is the normalised restricted signal decay, R is the cylinder radius, and E_h is the normalised hindered signal decay.
The hindered component is modelled by Gaussian diffusion with apparent diffusion coefficient D_h,

$$E_h = \exp(-\gamma^2 g^2 \delta^2 D_h(\Delta - \delta/3)). \tag{4.15}$$

The form of the restricted signal component depends on the choice of PGSE parameters. It is important to note that the two-compartment model in (4.14) is equivalent to the bi-exponential ADC model, with a deterministic relationship between ADC and R parameters. We outline here E_r under the short (SGP) and long gradient pulse durations.

4.2.4 Restricted Diffusion for Short Gradient Pulses

AxCaliber, derived under the SGP approximation, proposes a restricted diffusion signal within an axon of radius R given by (Assaf et al., 2008)

$$E_r(R,q,\Delta) = \sum_{n,k} w_{k,n} \exp(-\beta_{n,k}^2 D\Delta/R^2) \times \left(\frac{(2\pi qR) J_n'(2\pi qR)}{(2\pi qR)^2 - \beta_{n,k}^2} \right)^2, \tag{4.16}$$

where

$$w_{n,k} = \begin{cases} 4, & n = 0 \\ 8\frac{\beta_{n,k}^2}{\beta_{n,k}^2 - n^2}, & \text{otherwise} \end{cases} \tag{4.17}$$

The AxCaliber restricted signal, $E_r(q,\Delta)$, is implemented via integration of $E_r(R,q,\Delta)$ over R, using a grid approximation and a 2-parameter gamma distribution defining the ADD, $p(R)$.

4.2.5 Long Diffusion Gradient Imaging

Relaxing SGP condition by applying the diffusion gradient pulses for longer duration has been shown to produce stronger signal decay in the transverse fibre plane (Yeh and et al., 2010), which suggests the potential of long diffusion gradient pulses in discerning signal contributions from axons with varying radii. Hence, we develop an imaging paradigm with long duration diffusion gradient pulses applied perpendicular to principle nerve fibre axis, so that

$$\delta \approx \Delta, \tag{4.18}$$

where as before Δ is the separation between the DW gradients. As a result, contrast enhancement is achieved between axons at higher g values, resulting in improved inference of ADD from the signal decay $E(R,q,\Delta)$.
Signal attenuation within an impermeable cylinder for $\delta \approx \Delta$, (that is, when the gradient pulse duration is approximately equal to the time between gradient pulses) was derived in (Neuman, 1974),

$$E_r(R,\delta) = \exp\left(-\frac{2\gamma^2 G^2}{D} \sum_{m=1}^{\infty} \frac{\alpha_m^{-4}}{\alpha_m^2 R^2 - 2} \times \left(2\delta - \frac{3 - 4\exp(-\alpha_m^2 D\delta) + \exp(-2\alpha_m^2 D\delta)}{\alpha_m^2 D} \right) \right). \tag{4.19}$$

Note that E_r is now denoted as a function of δ rather than q, in order to separate the effect of gradient timing, δ, and amplitude, g. Here D is the free diffusion coefficient of water, R is the cylinder radius and α is the m^{th} root of the derivative of the Bessel function of first kind, $J_1'(\alpha_m R) = 0$.

Under the assumption that the imaged tissue is in the rapid diffusion regime (Wang et al., 1995), for which

$$\frac{D\delta}{R^2} >> 1, \tag{4.20}$$

the restricted signal attenuation expression (4.19) simplifies to

$$E_r(R, \delta) = \exp\left(-\frac{7R^4\gamma^2 g^2 \delta}{48D}\right). \tag{4.21}$$

As per the AxCaliber method, we integrate over the ensemble of axons weighted by their surface areas to determine $E_r(\delta)$,

$$E_r(\delta) = \int_R \pi R^2 \, E_r(R, \delta) \, p(R) \, dR. \tag{4.22}$$

where (4.22) is normalised such that $E_r(0) = 1$.

Unlike AxCaliber, however, we choose our ADD model, $p(R)$, such that the integration is tractable, returning an analytic form for E_r rather than a grid approximation. Given the fourth order dependence on R in (4.21), we model the ADD by a generalised gamma distribution,

$$p(R) = \left[\frac{\beta}{\theta\Gamma(k)}\right]\left(\frac{R}{\theta}\right)^{k\beta-1} \exp\left(-\left(\frac{R}{\theta}\right)^{\beta}\right), \tag{4.23}$$

with $\beta = 4$. Substituting (4.23) and (4.21) into (4.22) and carrying out the integration leads to the simplified expression for the restricted signal attenuation,

$$E_r(\delta) = \left(1 + \frac{7\theta^4\gamma^2 g^2 \delta}{48D}\right)^{-(k+0.5)}. \tag{4.24}$$

As, $\delta \approx \Delta$, the hindered component in (4.15) is simplified to

$$E_h = \exp\left(-\frac{2}{3}\gamma^2\delta^3 g^2 D_h\right). \tag{4.25}$$

As per CHARMED approach, contribution from both hindered and restricted compartments are combined through a weighted summation.

$$E(\mathbf{q}, \Delta) = f_h E_h(\mathbf{q}, \Delta) + f_r E_r(\mathbf{q}, \Delta). \tag{4.14}$$

f_h and f_r are the T2-weighted volume fractions of the hindered and restricted compartments, respectively.

4.3 Cramér Rao Analysis

Let $\boldsymbol{\theta} = [\theta_1, \theta_2, ..., \theta_M]$ be the parameter vector for a model under consideration. Assuming that the signal model, $\boldsymbol{x} = [E(q_1), E(q_2), ..., E(q_N)]$, generates the data and for sufficiently high SNR in data, the measured diffusion signal, $\boldsymbol{y} = [y(q_1), y(q_2), ..., y(q_N)]$, is modelled as,

$$\boldsymbol{y}(\boldsymbol{\theta}) = \boldsymbol{x}(\boldsymbol{\theta}) + \boldsymbol{e}(\boldsymbol{\theta}), \tag{4.26}$$

where $\boldsymbol{e}$ is zero-mean additive white Gaussian noise with variance σ_n^2.
The Fisher information matrix, $\boldsymbol{I_\theta}$, is defined as:

$$[\boldsymbol{I_\theta}]_{i,j} = -E\left(\frac{\partial^2 \ln(p(\boldsymbol{y};\boldsymbol{\theta}))}{\partial\theta_i \partial\theta_j}\right), \tag{4.27}$$

where $p(\boldsymbol{y};\boldsymbol{\theta})$ is the joint probability distribution of $\boldsymbol{y}$ and $\boldsymbol{\theta}$.
In case of Gaussian probability distribution, $\boldsymbol{I_\theta}$ is calculated from the derivatives of signal model w.r.t. to each unknown parameter:

$$[\boldsymbol{I_\theta}]_{i,j} = \frac{1}{\sigma_n^2}\left[\frac{\partial \boldsymbol{x}}{\partial\theta_i}\right]^T\left[\frac{\partial \boldsymbol{x}}{\partial\theta_j}\right]. \tag{4.28}$$

Let T be any given estimator of the model parameters. The Cramér Rao Lower Bound (CRLB) for estimated parameters is given by the matrix inverse of $\boldsymbol{I_\Theta}$ (Thomas and Cover, 1991),

$$\text{var}(T(\theta_i)) \geq [\boldsymbol{I_\theta}^{-1}]_{i,i}. \tag{4.29}$$

The above inequality provides a lower bound for the variance of an unbiased estimator of a parameter. For each model, the derivatives in (4.28) can be evaluated analytically.
In order to compare CRLBs between models, we define the normalised CRLB metric,

$$\rho_i = \frac{\text{std dev}(T(\theta_i))}{\theta_i}. \tag{4.30}$$

4.4 Methods

4.4.1 Microscopy

A semi-thin araldite section of the fetal sheep (119 days of gestation; term = 147 days) optic nerve was stained with toluidine blue and imaged using a bright-field microscope equipped with a 100x objective. In the resultant image, axons were manually labelled with circles, providing a histogram representing the empirical ADD. The ADD was fit in MATLAB by a fourth-order generalised gamma distribution (4.23), the best-fit parameters of which were found to be $k = 0.4$ and $\theta = 1.57$.

4.4.2 Simulations

Numerical simulations were carried out in order to generate synthetic diffusion decay curves based on known ADD's. For all simulations $D = 2$ μm^2/ms, $\delta = 60$ ms, and $\Delta = 65$ ms. Ten equally spaced g values from 0-400 mT/μm were applied perpendicular to principle axon axis. Axon diameters were drawn from the empirical optic nerve ADD, $p(R)$ with $\{\beta = 4, k = 0.4, \theta = 1.57\}$, and space was filled with a partial volume fraction of $f = 0.45$, estimated from the microscopy data. Two-dimensional Brownian motion simulations of 10^7 particles distributed uniformly across the synthetic nerve were carried out using a BlueGene/Q supercomputer, with a time step of 1 μs.

4.4.3 Experimental Diffusion-Weighted MRI

A rat brain embedded in agar was scanned twice on a 4.7T Bruker 30cm bore animal scanner using a PGSE-EPI acquisition. For the first scan, $TR/TE = 5000/54$ ms, b-values = [100:100:400, 600, 800, 1000:500:10000] s/mm^2 were used with matrix size 128×128 and $\delta = 8$ ms and $\Delta = 20$ ms. For the second scan $TR/TE =$ is 12000/37 ms, b-values = [100:100:400, 600, 800, 1000:500:10000] s/mm^2 were used with matrix size 96×96. $\delta = 6.5$ ms and $\Delta = 18$ ms, slice thickness = 1 mm. An in-plane resolution of 30 μm × 30 μm is used for both experiments.

A fetal sheep optic nerve (119 days of gestation) was removed posterior to the retina following perfusion fixation with 4% paraformaldehyde, embedded in agar. The optic nerve was then scanned on a 4.7T Bruker small animal MRI system using a PGSE-EPI acquisition with long gradient pulses. In this experiment, $TR/TE =$ 3000/65 ms, 20 gradient values evenly spaced at g = [0-400] mT/m, single slice of 1.5 mm, matrix size = 512×512, a resolution of 30 μm × 30 μm, NEX = 4, $\delta =$ 60 ms and $\Delta = 65$ ms. The 5 ms difference between δ and Δ was necessary for the refocusing pulse.

All imaging was performed with the approval of The Florey Animal Ethics Committee.

Post acquisition processing

Rat Brain

Three ROIs of varying sizes were manually delineated from corpus callosum (CC), thalamus and CSF regions of the rat brain and the mean normalised signals were recorded. The exponential, bi-exponential and gamma distribution models were fit to the three experimental datasets using the Levenberg-Marquardt algorithm to obtain parameter estimates $\hat{D}$, $(\hat{D_h}, \hat{D_r}, \hat{f})$ and $(\hat{k}, \hat{\theta})$, respectively. An estimate of noise variance, $\hat{\sigma_n^2}$, was also obtained from the mean normalised background signal.

Optic Nerve

A region of interest (ROI) of 10×10 voxels was selected from the centre of the optic nerve and the mean normalised signal was obtained. The two-component model with long gradient pulse duration, Eqns. (4.14), (4.15) and (4.24), was fit to extract the ADD ($p(R)$) parameters, k and θ, using the function 'fit' and a Trust Region estimation algorithm in MATLAB.

4.5 Results

4.5.1 Cramér Rao Bounds on ADC Model Parameters

The normalized CRLB metric (4.30), ρ_i, was computed for the bi-exponential and gamma distribution models at the empirical parameter values estimated from ovine experimental data, in order to assess the theoretical robustness of these models. The empirical values used, representative of experimental estimates, were $D_h = 0.5$, $D_r = 0.03$, $f = 0.3$, $k = 0.3$ and $\theta = 1$. The noise variance, σ_n^2, was fixed at 5.17e-04 (as estimated from the ovine experimental DW-MRI data) for all calculations. Even at a high maximum gradient value, $g_{max} = 400$ mT/m, typical of pre-clinical systems, with 20 g-values evenly separated between [0-g_{max}], the normalised CRLBs for both models are generally higher than 10% across a range of δ, with the only exception of normalised CRLB for k parameter of gamma distribution (Figure 4.3a). *Here 10% is chosen as a value at which the variability may be acceptable. Obviously, the closer to zero the bound is, the better.* Similarly, high normalized CRLBs are observed across gradient separations, Δ, for all parameter estimators except the rate parameter, k (Figure 4.3b). High CRLBs directly translate to higher variance in parameter estimates, suggesting that it is not possible to estimate true values of these parameters, even under ideal experimental conditions with minimum noise.

Similarly, normalized CRLBs are evaluated across a wide range of maximum gradient strengths, g_{max} up to 1000 mT/m (Figure 4.3c) and demonstrate that robustness of both models increase with increasing maximum gradient strength, as expected. At gradient strengths typical of human clinical scanners, these models must be applied with extreme caution. It is only as the gradients improve by an order of magnitude that the model estimates become viably robust. Furthermore, acquisition of 20 q-values between zero and g_{max} is arguably too long for anything but lengthy ex-vivo scanning.

4.5.2 Information in Restricted Signal Components

We demonstrate that, under the SGP, the restricted signal component is not able to distinguish between axons with sizes typically found in white matter. Consider a wide range of axons up to radius 3 μm, as may be typically found in white matter. Even at high gradient magnitude, $g = 200$ mT/m, achievable only on

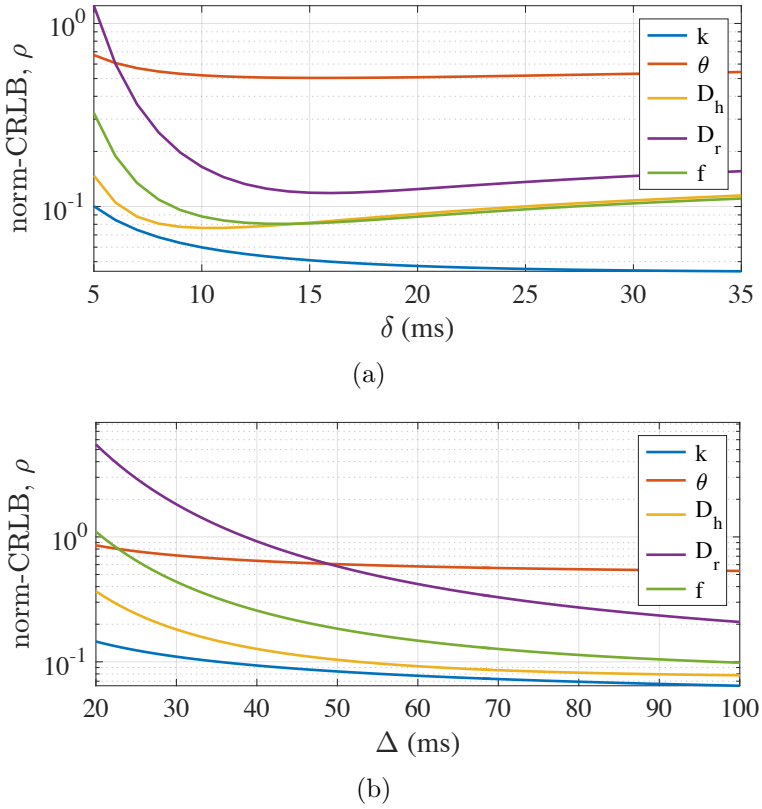

Figure 4.2: Cramér Rao lower bounds for diffusion models across (a) δ, $\Delta = 35$ms and (b) Δ, $\delta = 5$ms, at $g = 400$mT/m.

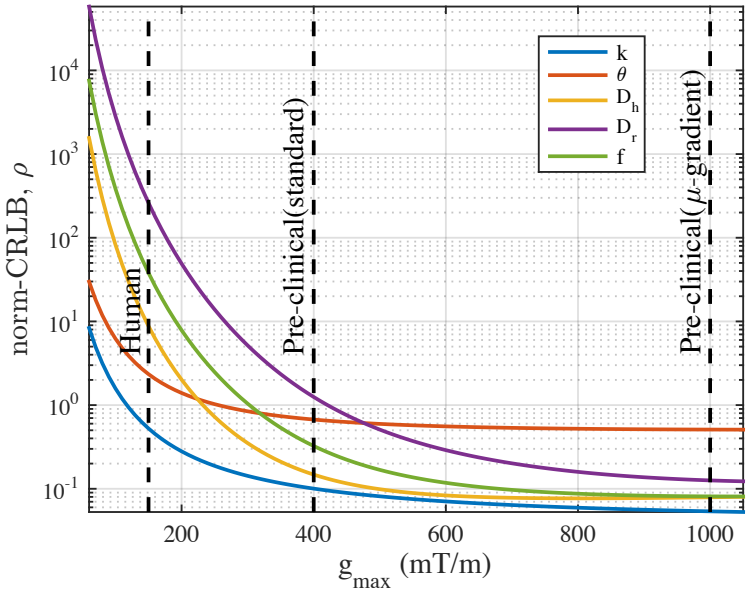

Figure 4.3: CRLBs at $\delta = 5$ ms and $\Delta = 35$ ms across multiple maximum gradient values. Dashed vertical lines indicate CRLBs at typical maximum gradient strengths of human, pre-clinical (standard) and pre-clinical (microgradient) scanners.

pre-clinical systems, the AxCaliber restricted components, $E_r(R, q, \Delta)$, are indistinguishable from each other (Figure 4.4a), and therefore this component carries very little information on which to base an ADD inference. In contrast to this, the long gradient pulse restricted component (4.21) clearly separates the contribution of each axon size, except at small radius, $R < 1$, where the signals exhibit little attenuation (Figure 4.4b).

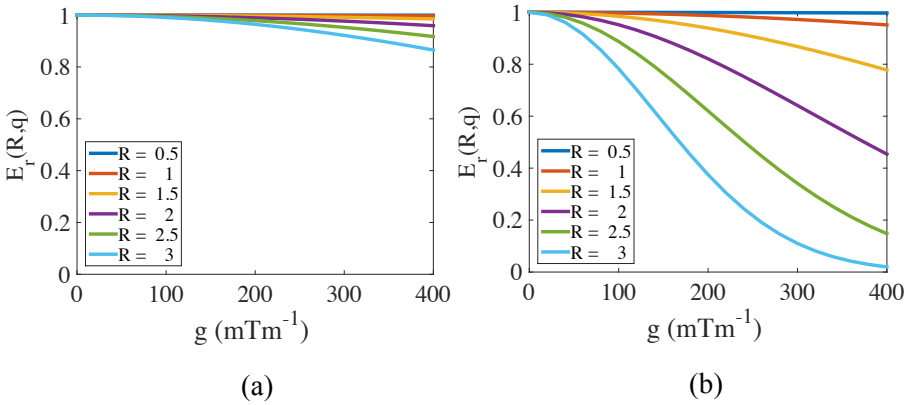

Figure 4.4: Comparison of restricted components for $\Delta = 65$ ms, and (a) short gradient pulse duration, $\delta = 4$ ms, (b) long gradient pulse duration, $\delta = 60$ ms.

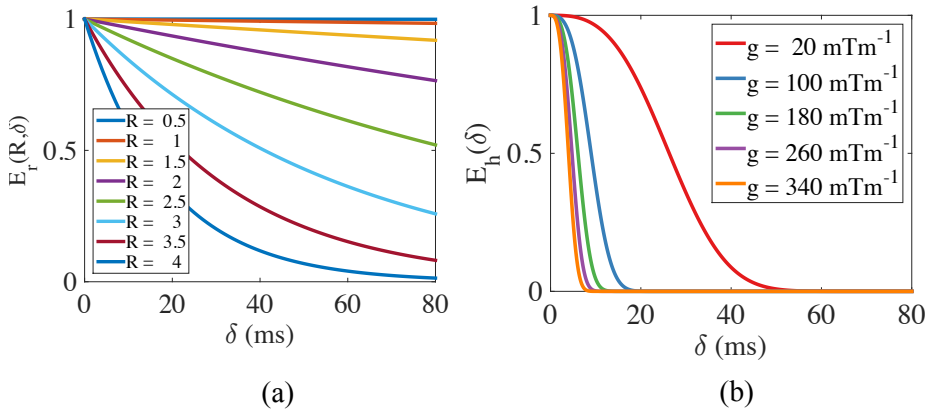

Figure 4.5: (a) Dependence of long gradient pulse restricted component on axon radius, across δ (g = 200 mT/m). (b) Hindered component attenuation across gradient durations.

A second advantageous feature of a long gradient pulse duration is the ability to separate restricted and hindered components. As demonstrated in Figure 4.5a, $E_r(R, \delta)$ exists across a broad range of δ values, while $E_h(\delta)$ in Figure 4.5b is seen to attenuate completely for $\delta > 20$ ms for all but very small gradient magnitudes.

4.5.3 Diffusion Coefficient Profile in Tissue

The experimental attenuation signals from within the optic nerve and rat brain (Figure 4.6a-b) for each set of experimental parameters (δ, Δ) is well-fit by the gamma distribution model. As Table 4.1 shows, the average Mean Square Error (MSE) of model fits to experimental data for the gamma model is comparable to the bi-exponential model, while the error is high for the exponential model, as expected.

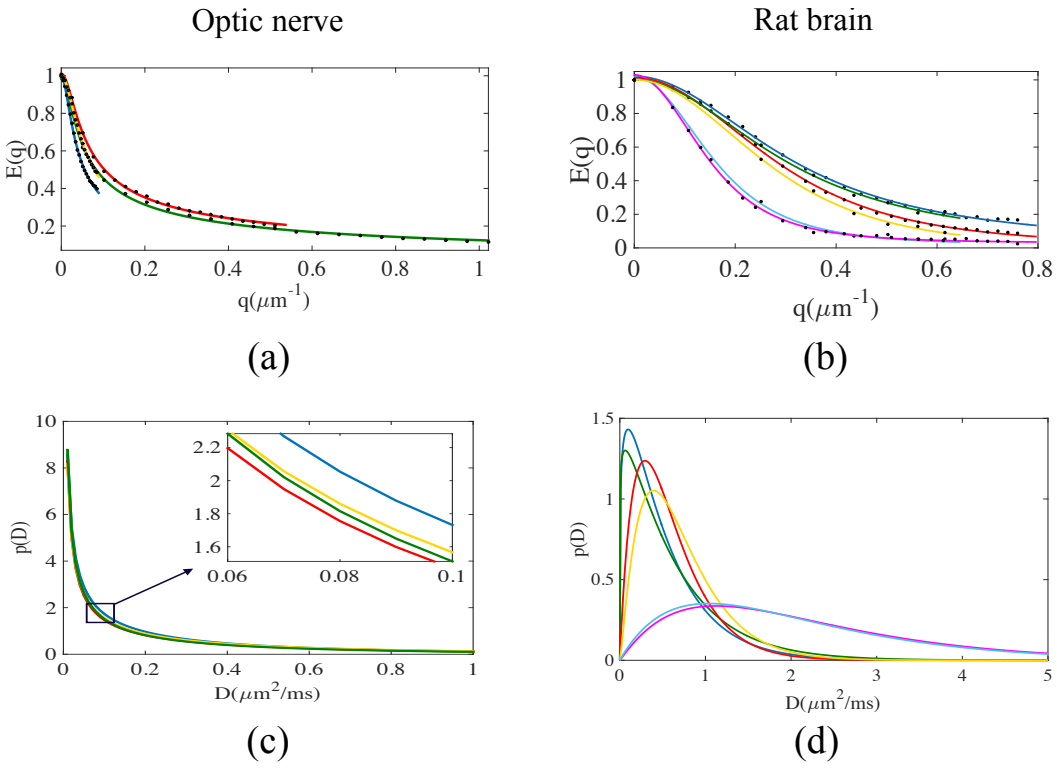

Figure 4.6: (a-b) Experimental q-space decay data fitted by the gamma distribution model from sheep optic nerve and rat brain, respectively. Data: black dots, model fit: solid lines, where (a) Optic nerve signals, yellow: [δ = 5 ms, Δ = 35 ms], red: [δ = 30 ms, Δ = 35 ms], blue: [δ = 5 ms, Δ = 65 ms] and green: [δ = 60 ms, Δ = 65 ms]. (b) Rat brain signals, blue (CC), red (Thalamus), magenta (CSF): [δ = 8 ms, Δ = 20 ms], green (CC), yellow (Thalamus) and cyan (CSF): [δ = 6.5 ms, Δ = 18 ms]. (c-d) Estimated ADC gamma distributions for all experimental datasets. (c) Optic nerve gamma distributions. Inset: zoomed distribution curves, demonstrating minor differences in $p(D)$ estimates. (d) Rat brain gamma distributions.

Table 4.1: Average MSE of model fits to experimental data

Dataset	Exp.	Bi-exp.	Gamma
Optic Nerve	7.7e-3	5.0e-4	1.0e-4
Rat Brain (CC)	4.4e-3	1.0e-4	2.0e-4
Rat Brain (Thalamus)	1.5e-3	1.0e-4	1.0e-4
Rat Brain (CSF)	7.0e-4	1.4e-4	3.6e-4

The mean parameter estimates corresponding to the MSE for each model are given in Table 4.2. A high level of variability exists in parameter estimates of exponential and bi-exponential models, as evidenced by the normalised standard deviation (as a percentage of the true parameter value). This variability in parameter estimates further validates the observations from CRLB analysis. The parameter estimates for the gamma distribution model are more consistent across the range of δ and Δ, with the exception of estimates of θ in rat CC. Highly consistent ADC distribution curves, obtained from curve fits of the four optic nerve and two rat brain DW-MRI datasets, further provide evidence to the robustness of the gamma model (Figure 4.6 c-d). It should be noted that despite high variability in θ, the gamma pdfs in rat CC are relatively unchanged.

The parameter maps for the bi-exponential and gamma models are given in (Figure 6.5). The k map reveals more detailed anatomical structure than other parameter maps.

Table 4.2: Parameter estimates for diffusion models

Data/Model	Exp.	Bi-exp.			Gamma	
	$\hat{D}$ (μm^2/ms)	$\hat{D}_r$ (μm^2/ms)	$\hat{D}_h$ (μm^2/ms)	$\hat{f}$ (a.u.)	$\hat{k}$ (a.u.)	$\hat{\theta}$ (a.u.)
Optic Nerve						
mean	0.13	0.01	0.37	0.42	0.31	0.90
s.d. (%)	0.69	0.96	0.42	0.31	0.12	0.16
Rat (CC)						
mean	0.44	0.04	0.62	0.26	1.16	0.50
s.d. (%)	0.13	0.16	0.11	0.03	0.07	0.18
Rat Thalamus						
mean	0.59	0.13	0.73	0.24	2.10	0.31
s.d. (%)	0.09	0.65	0.24	0.23	0.08	0.04
Rat (CSF)						
mean	1.65	0.07	1.72	0.10	2.02	1.06
s.d. (%)	0.15	1.21	0.18	0.47	0.02	0.01

4.5.4 ADD in Simulated and Experimental Data

We compare the results of numerical simulations with experimental diffusion-weighted MRI, in order to asses the ability of a two-component model to model the signal. Light microscopy of an ovine optic nerve (Figure 4.8a) was used to

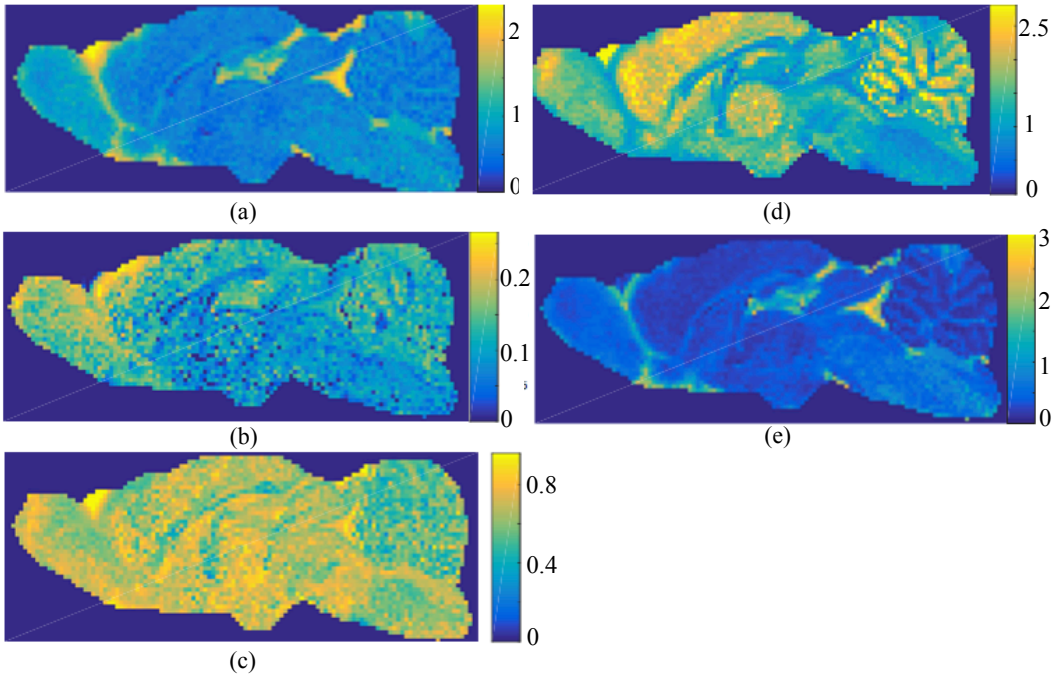

Figure 4.7: Parameter maps for bi-exponential model (a) D_h, (b) D_r, (c) f, and the gamma model (d) k, (e) θ.

manually construct an empirical ADD (Figure 4.8b, blue line). The simulated attenuation signal, including both hindered and long gradient restricted components (Figure 4.8c), lent itself well to inference of an accurate ADD estimate (Figure 4.8b, red line), with estimated $D_h = 0.54$ $\mu m^2/ms$.

The experimental attenuation signal from within the optic nerve (Figure 4.8d) is well-fit by the two-component model (compare black dots and overlaid blue model fit), however direct comparison of this experimental signal with the simulated signal (Figure 4.8c) indicates the mismatch in simulations versus experiment. This provides evidence that the two-component model does not capture the characteristics of the signal attenuation, and therefore should not be used for ADD inference, as is further supported by the ADD estimate (Figure 4.8b, green line) that is strongly skewed toward smaller axon sizes.

4.6 Summary

Through the CRLB analysis, we have exposed high uncertainty in parameter estimates of exponential, biexponential and gamma distribution models of ADC at gradient strengths typical of human and standard pre-clinical scanners. Given the complex tissue morphology, the gamma distribution model arguably provides a better description of the diffusion profile as it models a continuum of diffusion coefficients that can be attributed to hindered or restricted water diffusion across compartment sizes, endowed with more robust estimation as has been demon-

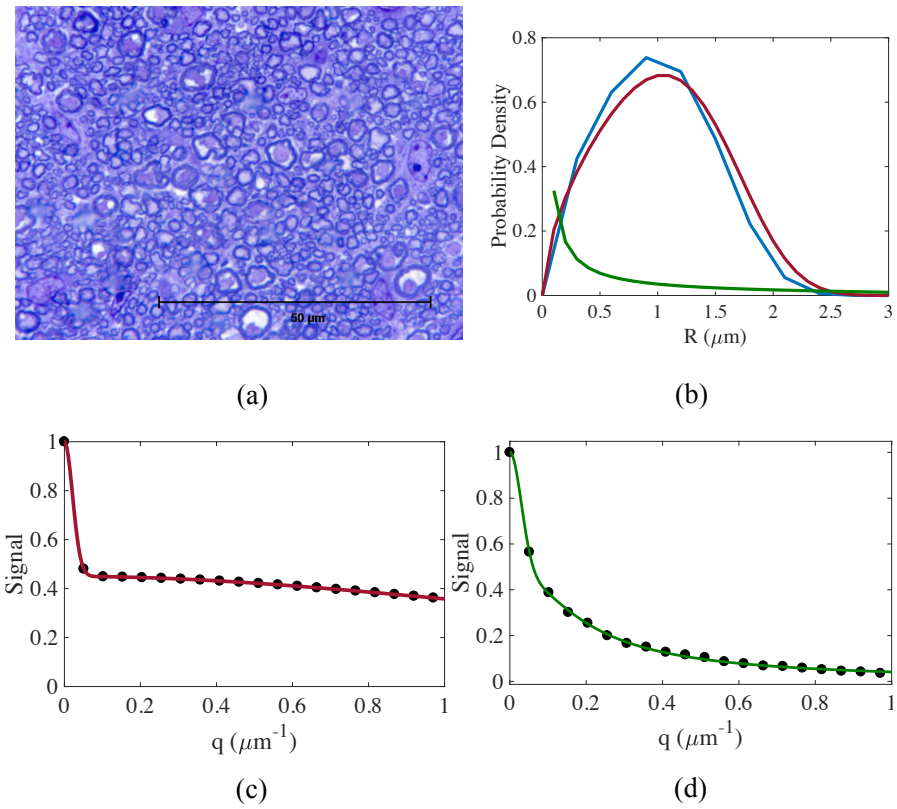

Figure 4.8: (a) Ovine optic nerve. (b) Empirical ADD (blue), ADD estimated from simulations (red) and ADD estimated from experimental MRI data (green). (c) Simulated $E(q)$ attenuation (data: black dots, model fit: solid line). (d) Experimental attenuation curve (data: black dots, model fit: solid line).

strated herein.

The two-component model on which ADD inference is based in SGP methods such as AxCaliber was shown to provide insufficient differentiation between signals from varying axon sizes in order to ensure robust inference. We exposed the limitations of the two-component model by considering long gradient pulse durations, ideal both for their property of separating contributions from small and large axons, and for their property of saturation of the hindered component. Simulations based on the long gradient pulse duration signal model, at $\Delta = 65$ ms, notably within the diffusion separation range applied in CHARMED (Assaf et al., 2004) and AxCaliber (Assaf et al., 2008), gave rise to a signal attenuation curve from which the empirical ADD could be accurately inferred. It was shown, however, that despite inference being possible, the model did not provide an accurate fit to experimental diffusion-weighted data. Propagation of uncertainty from ADC to ADD estimates, incompleteness of signal models in describing complex biophysical diffusion processes and imaging artifacts such as ghosting and signal wrapping are the potential factors contributing to the discrepancy between simulated and experimental MRI

analyses. There were several questions raised about the low b-value acquisitions on the 4.7T scanner, with a slight signal increase observed at low b-values compared to the non-diffusion weighted signal. These questions remained unanswered due to technical complications with the Bruker system; as the purpose of this thesis was analysis and not acquisition, we continued with other compartment modelling and estimation topics, rather than continuing to try to fit ADDs to erroneous data.

Exchange between components is the most likely mechanism to incorporate into the model, although exchange has previously been reported to be insignificant given the timing of PGSE sequences (Assaf et al., 2004). Future work can investigate how to incorporate exchange into the two-component model, to verify whether this can account for the discrepancies between experimental and simulated data. Previous approaches have used a two-pool Karger model (Stanisz et al., 1997; Davoodi-Bojd et al., 2014), however this model is averaged over axon radii prior to exchange. It is unlikely that more realistic modelling of exchange will lead to a closed form expression for restricted diffusion such as the one we propose here, and numerical analysis methods will need to be explored.

CHAPTER
FIVE

Techniques for Improving Signal-to-Noise Ratio in Multi-echo MRI Images

5.1 Introduction

In any MRI acquisition, high signal-to-noise ratio (SNR) is extremely desirable for producing high quality images and for achieving informative and robust quantitative parameter maps. There are a plethora of techniques developed to improve SNR in the various stages of MRI acquisition and analysis pipelines, ranging from the administration of contrast enhancing agents in the pre-imaging stage (Caravan et al., 1999; Na et al., 2009; Caravan, 2006; Schmid et al., 2013), to optimized pulse and sequence design (Duerk et al., 1998; Stenger et al., 2000; Fong, 2005; Stanisz et al., 2005), and dedicated analysis methods (Redpath, 1998; Gerig et al., 1992; Wood and Johnson, 1999; Pizurica et al., 2006; Manjón et al., 2008; Wink and Roerdink, 2004). In this chapter, we consider the optimal combination of multiecho MRI data into composite images that possess improved regional contrast and SNR, advantageous for further data analysis and inference. Given the computational simplicity and ease of implementation of the averaging operation, numerous echo averaging strategies have been proposed that range from simple echo summation to more sophisticated weighted averaging methods. Echo averaging techniques have been applied successfully to diffusion weighted imaging (Nana et al., 2008; Tu et al., 2014), susceptibility weighted imaging (SWI)(Denk and Rauscher, 2010; Wu et al., 2012; Xie et al., 2015), sodium imaging (Blunck et al., 2018), quantitative spinal cord imaging (Cohen-Adad and Wheeler-Kingshott, 2014, p. 109), chemical exchange saturation transfer imaging (CEST) (Sun et al., 2014), FLASH (Helms and Dechent, 2009) and multiecho functional MRI (fMRI) (Posse et al., 1999; Poser et al., 2006; Schmiedeskamp et al., 2010; Gowland and Bowtell, 2007; Kundu et al., 2012; Bhavsar et al., 2014; Puckett et al., 2017; Cohen et al., 2018).

In multiecho acquisitions, multiple echoes are acquired in place of a single echo, typically without prolonging the overall acquisition time. T_2-weighted multiecho techniques sample multiple time-points across the transverse relaxation decay, offering richer information about underlying tissue structure than single echo imaging. The overall gain in SNR through averaging depends on a number of tissue and experiment design parameters, such as the transverse relaxation properties of the underlying tissue, the initial echo time, inter-echo spacing and the noise distribution. The MR signal arising from tissue with faster transverse relaxation decays rapidly, and the later echoes predominantly contain noise. Inclusion of the later echoes in the averaging process leads to SNR drop-off, causing the SNR gain to be tissue-dependent. On the other hand, signal from regions with slower transverse relaxation decay (such as CSF) persists longer, and greater SNR improvement is achievable by averaging later echoes. Therefore, the number of echoes used in the averaging operation is crucial in improving SNR. Previous methods have regulated the averaging process either by discarding the later echoes or through voxel-weighting. Both of these strategies may be sub-optimal solutions; discarding the echoes may result in loss of information, where as weighted averages still include all available echoes, which might result in accumulation of noise. Therefore, it is worthwhile to develop methods for SNR improvement by using optimal

number of echoes in each voxel.

Within the widespread set of echo-combining strategies in the literature, we identify two distinct echo-averaging subsets based on the mathematical treatment of the averaging operation. The first subset contains global techniques that combine either first few, or all echoes, into a single composite image without voxelwise weighting. These methods are usually employed to improve visual quality of low-intensity, high-noise structural images, such as in (Blunck et al., 2018) and (Cohen-Adad and Wheeler-Kingshott, 2014, p.109), in which echo-averaged structural images were presented for low-intensity sodium MRI and quantitative spinal cord imaging studies, respectively. Xie et al. (2015) quantified anisotropy of tubules through SNR-optimized renal susceptibility tensor imaging by averaging the first few echoes. In addition to improving visual quality of the images, echo averaging has been widely applied to increase sensitivity to a wide range of tissue-contrast mechanisms. The second subset of multiecho averaging techniques comprises local voxelwise echo averaging methods that take into account tissue-dependent SNR enhancement and perform voxelwise weighted echo averaging. Based on the nature of the weighting function, voxelwise methods can be further divided into model-free and model-based echo averaging strategies. Model-free voxelwise techniques exploit the information available in empirically determined weighting functions to optimize tissue-dependent SNR. For instance, model-free echo summation strategies were proposed in (Poser et al., 2006; Puckett et al., 2017) weighting each echo by temporal SNR, echo time or simple temporal averaging.

The weights in model-based local averaging are determined by the choice of signal decay model. Nana et al. (2008) proposed a voxelwise weighted echo summation strategy for multiecho parallel EPI acquisition. The weights were determined from multiecho images, under the assumption of mono-exponential T_2 decay. They performed a region-of-interest (ROI) analysis across several tissue types; in GM and WM regions, numerical analyses demonstrated tissue-dependent SNR gain, with the SNR curves tapering off as the number of echoes used for the averaging operation increased. This is not surprising, as signal decay in tissue due to T_2 will lead to an accumulation of noise in the averaged image if the echo time is too long. Tu et al. (2014) employed a similar echo summation strategy, with a phase correction scheme on complex DWI data prior to averaging, and reported similar results. A least squares based optimization algorithm for echo averaging was used to obtain sensitivity enhanced CEST images in (Sun et al., 2014). In SWI, SNR- and contrast-enhanced venography have been performed through combining susceptibility-weighted images from multiple echo times (Denk and Rauscher, 2010). Another such technique computes tissue-optimized resonance frequency shifts through weighted averaging of multiecho gradient-echo data, with a T_2 decay weighting function (Wu et al., 2012).

In fMRI analyses, model-based echo averaging has proven beneficial in increas-

ing BOLD contrast. Posse et al. (1999) demonstrated increased sensitivity to BOLD contrast in single-shot multiecho fMRI through combining data arising from evenly-spaced echo times. They proposed three separate averaging strategies: simple echo summation, weighted echo summation with T_2 weighting, and voxel-wise model-fitting for estimating T_2 followed by weighted echo summation. The theoretical optimization framework proposed in (Gowland and Bowtell, 2007) studied the influence of echo-spacing on the sensitivity of various echo averaging strategies, while incorporating non-exponential decay models into the analysis. The majority of model-based techniques assume exponential weighting functions, described by a single parameter. In addition to model-based techniques, Chiew and Graham (2011) proposed a data-driven echo averaging scheme to improve contrast-to-noise ratio (CNR) in fMRI data, with weights from the principal component analysis. Strong dependence of CNR gain on the physiological noise, echo-spacing and sampling window width was demonstrated, with marginal CNR improvements observed beyond the sampling window width of $3T_2^*$ (Chiew and Graham, 2011).

The model-based voxelwise averaging can be carried out using expected or estimated parameter values in different tissue types. Further, multiple echoes can be combined in complex k-space, complex image space or magnitude image space. Phase variations introduced in the signal due to static field inhomogeneities (Majumdar et al., 1986a) and radiofrequency pulse imperfections (Majumdar et al., 1986b) degrade the performance of echo averaging (Tu et al., 2014). Greater SNR improvement has been reported using the magnitude images (Tu et al., 2014); multiecho gradient echo sequences such as MEDIC or MERGE, commercially available on Siemens and GE scanners, combine multiecho data in the magnitude domain to produce high contrast images (Martin et al., 2012; Schmid et al., 2005).

In this chapter, we develop methods for achieving maximized tissue-dependent SNR gain in magnitude images through averaging optimum number of echoes, n_{opt}. We characterize the distribution of the averaged signal under an assumption of additive Gaussian noise, and construct an optimization problem to find n_{opt}. We consider three models of MR signal decay; the mono-exponential model assumes a single exponential signal decay, characterised by a decay constant. The nature of the decay constant is defined by the imaging modality. For instance, T_2- or T_2^*-weighted decay in transverse relaxation decay (Levitt, 2001) or apparent diffusion coefficient weighted decay for the diffusion weighted signal (Le Bihan et al., 1986). The bi-exponential model describes non-exponential decay by assuming the signal to be comprised of two separate components, each with a distinct decay constant, such as the bi-exponential model of transverse relaxation (Cole et al., 1993) and diffusion (Niendorf et al., 1996). Continuous distribution models of signal decay assume the presence of a continuum of components, characterized by a distribution of the decay constant. The inverse-gamma model considered here is a simplified version of the continuous distribution models of transverse decay proposed in (Layton et al., 2013; Whittall and MacKay, 1989). Similarly, gamma distribution models have been proposed for diffusion weighted data (Yablonskiy et al., 2003; Scherrer et al., 2016). Based on these models, we develop both ex-

ponential and non-exponential weighting functions, which can be calculated using either expected or estimated parameter values. We demonstrate that each weighting function is capable of predicting the optimal number of echoes required for maximum SNR improvement across tissue types.

For the global echo averaging scheme, a constant n_{opt} (n_{g}^*) is used to perform voxelwise averaging. The value of n_{g}^* can be chosen to achieve SNR improvement optimized for any given tissue type. Alternatively, for the case of voxelwise averaging, n_{opt} is calculated for each voxel based on the underlying tissue type and signal model. We refer to this regime of echo averaging by n_{v}^*. Additionally, we construct a model-free composite image using empirically determined n_{v}^* and measure the performance of model-based methods against it. We demonstrate the equivalence in SNR gain using a Gaussian model assumption even when experimental data contains Rician distributed noise.

We apply our optimised echo averaging techniques to two T_2^*-weighted multiecho MRI datasets. The first is multiecho sodium MRI in invivo human. Signal from sodium MRI is inherently low-intensity due to the low concentration of sodium and the smaller gyromagnetic ratio of sodium spins, leading to diminished SNR even under low noise conditions. The second dataset is T_2^*-weighted multiecho proton MRI of in vivo rat brain. We demonstrate that the proposed methods perform successful SNR optimization under these challenging conditions.

5.2 SNR Optimization via Echo Averaging

Consider a set of N multi-echo images acquired at echo times $t_i = t_0 + (i-1)s,\ i = 1, \ldots, N$, where s is the inter-echo spacing and t_0 the initial echo time. Let y_i be the measured signal in a given voxel at echo i. We consider the voxelwise signal model,

$$y_i = A_0 w_i + \eta_i, \quad i = 1, \ldots, N \tag{5.1}$$

where A_0 is the signal strength at time $t = 0$, w_i is the decay weight of a given relaxation model, and $\eta_i \sim N(0, \sigma^2)$ is additive, white Gaussian noise.
The SNR in the given voxel, at the first echo is

$$SNR_1 = \frac{A_0 e^{-t_0/T_2}}{\sigma}. \tag{5.2}$$

The SNR after averaging the first n echoes is

$$\text{SNR}_n = \text{SNR}_1 \frac{1}{\sqrt{n}} \sum_{i=1}^{n} w_i. \tag{5.3}$$

Hence, improvement in SNR from averaging echoes occurs when

$$\frac{\text{SNR}_n}{\text{SNR}_1} = \frac{1}{\sqrt{n}} \sum_{i=1}^{n} w_i \ \geq \ 1. \tag{5.4}$$

The objective is to find the number of echoes that maximizes the ratio $\frac{\mathrm{SNR}_n}{\mathrm{SNR}_1}$:

$$n_{\mathrm{opt}} = \arg\max_n \left(\frac{\mathrm{SNR}_n}{\mathrm{SNR}_1} \right). \tag{5.5}$$

n_{opt} can be determined by solving

$$\frac{\partial}{\partial n} \left(\frac{1}{\sqrt{n}} \sum_{i=1}^{n} w_i \right) = 0, \tag{5.6}$$

and rounding the resultant optimal value of n. Note that for convenience, we model only T_2 decay. All results hold equally for T_2^* decay and any other decay model.

The Mono-Exponential Model

The mono-exponential model (ME) assumes that the signal decay over TE can be described by a single exponential decay with time constant, T_2. At echo time t_i, the decay weight is:

$$w_i = e^{-(i-1)\, s/T_2}. \tag{5.7}$$

The weight summation in (5.6) is given by

$$\begin{aligned} \sum_{i=1}^{n} w_i &= \sum_{i=0}^{n-1} e^{-is/T_2} \\ &= \frac{e^{s/T_2} - e^{-(n-1)s/T_2}}{e^{s/T_2} - 1}. \end{aligned} \tag{5.8}$$

Substituting (5.8) into (5.6) and simplifying yields the following expression:

$$\left(\frac{2ns}{T_2} + 1 \right) e^{-ns/T_2} - e^{s/T_2} = 0. \tag{5.9}$$

The optimum number of echoes is therefore given by

$$n_{\mathrm{opt}} = \lfloor -T_2/s \left(W_{-1}(-0.5\, e^{-0.5}) + 0.5 \right) \rceil, \tag{5.10}$$

where $\lfloor \rceil$ is the nearest integer function and W_{-1} is the Lambert-W function (Olver et al., 2010).

Bi-exponential Model

The bi-exponential model of transverse relaxation decay assumes the signal to be composed of two separate components, often expressed as short and long transverse relaxation decays. Each component is described by an exponential decay,

$$\begin{aligned} w_i &= f\, e^{-t_i/T_{2a}} + (1-f)\, e^{-t_i/T_{2b}} \\ &= f\, e^{-t_0/T_{2a}}\, e^{-i\, s/T_{2a}} + (1-f)\, e^{-t_0/T_{2b}}\, e^{-i\, s/T_{2b}}, \end{aligned} \tag{5.11}$$

where T_{2a} and T_{2b} are the short and long time constants and $0 \leq f \leq 1$ is the volume fraction. The weight summation in (5.6) is calculated as:

$$\sum_{i=0}^{n-1} w_i = f\, e^{-t_0/T_{2\,a}} \frac{e^{s/T_{2a}} - e^{-s/T_{2a}(n-1)}}{e^{s/T_{2a}} - 1} + (1-f)\, e^{-t_0/T_{2b}} \frac{e^{s/T_{2\,b}} - e^{-s/T_{2b}(n-1)}}{e^{s/T_{2b}} - 1}. \tag{5.12}$$

Solving (5.12) and (5.6) together leads to the following expression.

$$(C_0 n + C_1)e^{(-s/T_{2a}(n-1))} + (C_2 n + C_3)e^{(-s/T_{2b}(n-1))} + C_4 = 0, \tag{5.13}$$

where

$$\begin{aligned}
C_0 &= \frac{2sf}{T_{2a}} e^{-t_0/T_{2a}} (e^{s/T_{2b}} - 1), \\
C_1 &= f\, e^{-t_0/T_{2a}}\, (e^{s/T_{2b}} - 1), \\
C_2 &= \frac{2s(1-f)}{T_{2b}}\, e^{-t_0/T_{2b}}\, (e^{s/T_{2a}} - 1), \\
C_3 &= (1-f)\, e^{-t_0/T_{2b}}\, (e^{s/T_{2a}} - 1), \\
C_4 &= -f\, e^{(s-t_0)/T_{2a}}\, (e^{s/T_{2b}} - 1), \\
&\quad - (1-f)\, e^{(s-TE_0)/T_{2b}}\, (e^{s/T_{2a}} - 1).
\end{aligned}$$

The optimum number of echoes, n_{opt}, is given by the rounded root of (5.13). As (5.13) is intractable, an approximate solution can be found through a numerical root finding algorithm (see Methods).

Gamma Distribution Model

In contrast to the BE model that describes the signal as a weighted sum of two discrete T_2 components, the gamma distribution (GA) model assumes a continuum of T_2 components. The GA model admits an inverse-gamma distribution over T_2, or equivalently, a gamma distribution over the decay rate, R_2. The gamma pdf, $p(R_2; k, \theta)$, is parametrized by scale parameter, θ, and rate parameter, k.

The $T_{2\,\text{GA}}$ parameter is defined to be the reciprocal of the mean rate, $R_{2\,\text{GA}} = k\theta$. The decay weights in (5.6) are

$$\begin{aligned}
w_i &= (1 + t_i\theta)^{-k} \\
&= (1 + t_0\theta + is\theta)^{-k}.
\end{aligned} \tag{5.14}$$

Therefore, it follows that

$$\begin{aligned}
\sum_{i=0}^{n-1} w_i &= \sum_{i=0}^{n-1} (1 + t_0\theta + is\theta)^{-k} \\
&= \zeta'(k, 1 + t_0\theta, s\theta) - \zeta'(k, 1 + (t_0 + ns)\theta, s\theta),
\end{aligned} \tag{5.15}$$

where $\zeta'(x, y, z)$ is the modified Hurwitz zeta function defined as,

$$\zeta'(x, y, z) \triangleq \sum_{q=0}^{\infty} (y + zq)^{-x}. \tag{5.16}$$

Solving (5.6) and (5.15) together leads to the following expression.

$$2nsk\theta\ \zeta'(k+1, 1+(t_0+ns)\theta, s\theta) + \zeta'(k, 1+(t_0+ns)\theta, s\theta) - \zeta'(k, 1+t_0\theta, s\theta). \tag{5.17}$$

Similar to the case of BE model, (5.17) is solved using a root finding algorithm, as will be described in the Methods section.

5.2.1 Methods

Simulations

Simulations were performed to evaluate the performance of optimized echo averaging scheme using the ME, BE and GA models of T_2-weighted signal. Zero mean white Gaussian noise with equal variance, σ^2, was assumed on the real and imaginary channels of complex-valued MRI data. Without loss of generality, the MRI signal was assumed to be zero phase. A magnitude signal was generated by combining real and imaginary parts of the simulated MRI signal. Echo averaging was performed on both the real and magnitude signals with the purpose of empirically determining n_{opt} from the SNR curve. Each experiment was repeated N_{trial} = 1000 times, and the mean and standard deviation of the empirical n_{opt} were calculated.

Two separate sets of simulations were performed for each model. In the first set, imaging and model parameters were selected to study the performance of echo averaging over a wide range of parameter values. The initial signal strength was fixed at A_0 = 1a.u., $\sigma \in$ {5.0e-2, 5.0e-3}, the initial echo time, TE_0=0.01 ms, and 40 echoes were generated with echo spacing $s \in \{5, 10, 20\}$ ms. For the ME model, the parameter $T_2 \in \{10, 25, 100\}$ ms. The BE model consisted of a short component with $T_{2a} \in \{25, 50\}$ ms and a long component with $T_{2b} \in \{50, 100\}$ ms, with a total of 3 unique combinations. The volume fraction, f, was fixed at 0.5. Similarly, for the GA model, $k \in$ {3.33, 17, 4.54e2} and $\theta \in$ {3.00e-2, 2.35e-3, 2.20e-5}.

For the second set of simulations, model parameters were chosen to reflect the imaging conditions of the low intensity sodium MRI data at 7T (see MRI experiments section). For these simulations, σ = 190.25, A_0 = 2.86e3 for all models, initial echo time, TE_0 = 0.4 ms and echo spacing, s = 4 ms with a total of 38 echoes. The values of model parameters were derived from ROI analysis of the MRI data, with T_2 = 12.6 ms, T_{2a} = 5.5 ms, T_{2b} = 23 ms, f = 0.6, k = 2.45 and θ = 0.049 for the ME, BE and GA models, respectively.

MRI Experiments

Proton MRI experiments were run on a 4.7T Bruker BioSpec small bore animal MRI scanner. A rat brain was scanned using a MGE sequence. T_2^*-weighted images were acquired with TR = 110ms and 20 evenly spaced echoes with initial echo time at 4ms and inter-echo spacing of 4ms, 70 slices with thickness 10.5, matrix = 352 x 128, 150µm isotropic resolution, FOV = 2.64 x 1.92 x 1.05cm.

Sodium imaging was performed on a research 7T MRI scanner (Siemens Healthcare, Erlangen, Germany) equipped with a transmit/receive dual-tuned ^{1}H-^{23}Na head coil (QED, USA). T_2^*-weighted ^{23}Na MRI was performed on four healthy volunteers using the 3D-MERINA imaging protocol Blunck et al. (2018). Experimental parameters were: repetition time TR = 160 ms, initial echo time, TE_1 = 400μs, sampling duration, T_{RO} = 2ms, 38 echoes, FOV = 20cm, 3.1 mm isotropic resolution with N=10,000 projections.

Parameter Estimation

The estimation of T_2^*-weighted model parameters was performed on the magnitude images obtained from the experimental MRI data. It is well-known that noise in magnitude images is Rician-distributed (Bouhrara et al., 2015). In the absence of an MRI signal, such as in the background region, the noise reduces to be Rayleigh-distributed, with a mean value of $\sigma\sqrt{\pi/2}$. Here, σ is the standard deviation of the underlying zero mean Gaussian white noise in the complex domain. Analysis of noise properties in the rat brain and sodium MRI data was performed on rectangular ROIs selected in the background region. In case of sodium MRI data, the presence of Rayleigh noise was validated and the noise variance, σ^2 was empirically estimated from the mean value of a Rayleigh-distributed background ROI noise. On the other hand, the noise in rat brain data was found to be well-fit by a Gaussian distribution with non-zero mean and positive variance. Therefore, an additive white Gaussian noise model was assumed for this dataset.

For sodium MRI data, a Maximum Likelihood (ML) estimation routine with Rician log-likelihood function, as described in (Sijbers et al., 1998), was employed for parameter estimation. Similarly, for the rat brain data, a Gaussian log-likelihood function was employed. For each model, the ML estimates of the parameters were achieved by maximizing the log-likelihood function using a built-in constrained nonlinear least-squares solver in MATLAB. A detailed description of the parameter estimation algorithm can be found in (Blunck et al., 2018).

Root-finding Algorithm

A two-step root-finding algorithm was implemented in MATLAB to numerically determine n_{opt} for the BE and GA models from (5.13) and (5.17), respectively. Let $f'(n)$ be the function given by the left hand side of either (5.13) or (5.17),

where $n \in Z^+$. In the first step, the potential locations of the roots of $f'(n)$ are heuristically determined. More specifically, all such intervals $[a_i - 1, a_i]$ are identified between $[1, n]$ for which the condition, $\{a_i \,|\, a_i \in Z^+ \cap [1, n],\ f'(a_i - 1)$ and $f'(a_i)$ have opposite signs, $\forall$i=1,. . . ,m$\}$ is true. The initial estimate of the location of the root, a_i^*, is simply given by

$$a_i^* = \arg\max_i\ f(a_i). \tag{5.18}$$

Here, the upper endpoint of the interval $[a_i^* - 1, a_i^*]$ is arbitrarily chosen. In reality, n_{opt} could be either one of the endpoints. The second step is to determine the precise location of the root by employing a built-in MATLAB function for finding the root of a continuous nonlinear function. This MATLAB function implements a linear interpolation algorithm, as described in (Dekker, 1969). The value, $\hat{n}_{\text{opt}}$ is provided as the initial guess and the output from MATLAB's function is rounded to the nearest integer to obtain an estimate of n_{opt}.

$$\hat{n}_{\text{opt}} = \lfloor \text{fzero}\,(f(n), a_i^*) \rceil. \tag{5.19}$$

Echo Averaging

Voxelwise averaging was performed on the sodium MRI and rat brain data. For each dataset, four separate voxelwise averaged images were generated using empirically determined and model-dependent values of n_{v}^* obtained after model-fitting. Averaged signal from each voxel was SNR-normalized according to (5.3). In case of averaging using n_{g}^*, two composite images were obtained. For the first image, the value of n_{g}^* was given by the mode of number of echoes used for voxelwise averaged image. The mode value was 4 echoes in the sodium MRI and 10 echoes in the rat brain datasets. In second image, all available echoes were averaged (38 echoes for sodium MRI and 20 echoes for the rat brain data). Each averaged image was normalized for comparison with voxel-wise averaged images.

5.3 Results

Optimum number of Echoes for SNR Enhancement

Simulations

We first investigate the performance of signal decay models using a range of tissue and experimental parameters. The mean and standard deviation of $\hat{n}_{\text{opt}}$ calculated from the first set of simulations across a range of parameters are shown in Table 5.1-5.3. Here the initial signal strength, A_0, is fixed at 1 and $t_0 = 0.01$ms. In case of ME model (Table 5.1), the mean value of empirically determined $\hat{n}_{\text{opt}}$ is closely matched with the theoretically computed n_{opt} across the inter-echo spacing, s. As expected, less variations in the mean value of $\hat{n}_{\text{opt}}$ are observed at lower noise levels (last column of Table 5.1). Greater improvement in SNR is achieved with small inter-echo spacing, s, and slow T_2 components. Results from simulations of

BE signal model show similar trends (Table 5.2). Improvements in SNR up to a factor of 2.47 is observed when both T_2 components are comparatively longer (50,100)ms with smallest considered echo spacing of 5ms. Due to rapidly decaying signal, n_{opt}, is generally lower for smaller T_2 values and large inter-echo spacing. The simulation parameter for the GA model were selected so as to match the values of the mean T_{GA} to the decay constant, T_2, of the ME model (Table 5.3). The locations of $\hat{n}_{\text{opt}}$ estimated by the GA model are in good agreement to those estimated by the ME model, with the only exception of the n_{opt} at $T_{2\,\text{GA}} = 25$ms at the inter-echo spacing of 5ms.

SNR curves under low signal intensity conditions of simulated sodium MRI data are plotted against n_{opt} are presented in Figure 5.1. The empirically obtained SNR curves for each signal model are matched closely to the theoretically predicted curves. Each model provides identical location of n_{opt}, as expected. SNR curves from both Gaussian and Rician distributed signals match closely in the start and predict identical SNR improvement through averaging. The influence of noise distribution on the averaging process becomes apparent with increasing number of averaged echoes, as both curves start declining and diverging. The bias introduced due to the Rician noise causes the SNR curve to slowly taper off, in contrast to the zero-mean Gaussian noise SNR curve which drops more rapidly.

In vivo data

We compare the results of numerical simulations with experimental MRI, in order to assess the ability of the proposed methods to estimate n_{opt} correctly in practical situations. For sodium MRI data, the signal from a tissue ROI was fitted by the ME, BE and GA models of the transverse relaxation decay (Figure 5.2a). The ME curve-fit was least accurate, mainly due to the inability of the ME model to characterize non-exponential decay. The BE and GA curve-fits showed comparable accuracy. Parameter estimates were used to generate SNR curves across the number of echoes and to predict the location of n_{opt}, along with an empirically determined SNR curve through averaging data points (Figure 5.2b). All three models successfully identified the location of n_{opt}, despite the ME SNR curve being slightly different. Due to the bias in the data, the empirical SNR curve deviates significantly from the model-based Gaussian-distributed SNR curves with the increasing number of averaged echoes. However, this deviation from Gaussian behaviour does not have any significant effect on the location of n_{opt}, where highest SNR is observed and the Rician noise is well-approximated by a Gaussian distribution.

The mean signal from a tissue ROI in the rat brain data was fitted to the signal models (Figure 5.3a). All three models demonstrated comparable accuracy, and the corresponding SNR curves were identical. Further, the model-generated SNR curves closely matched the empirically generated SNR curve, validating our observation of Gaussian-distributed noise in the data (Figure 5.3b). The location of

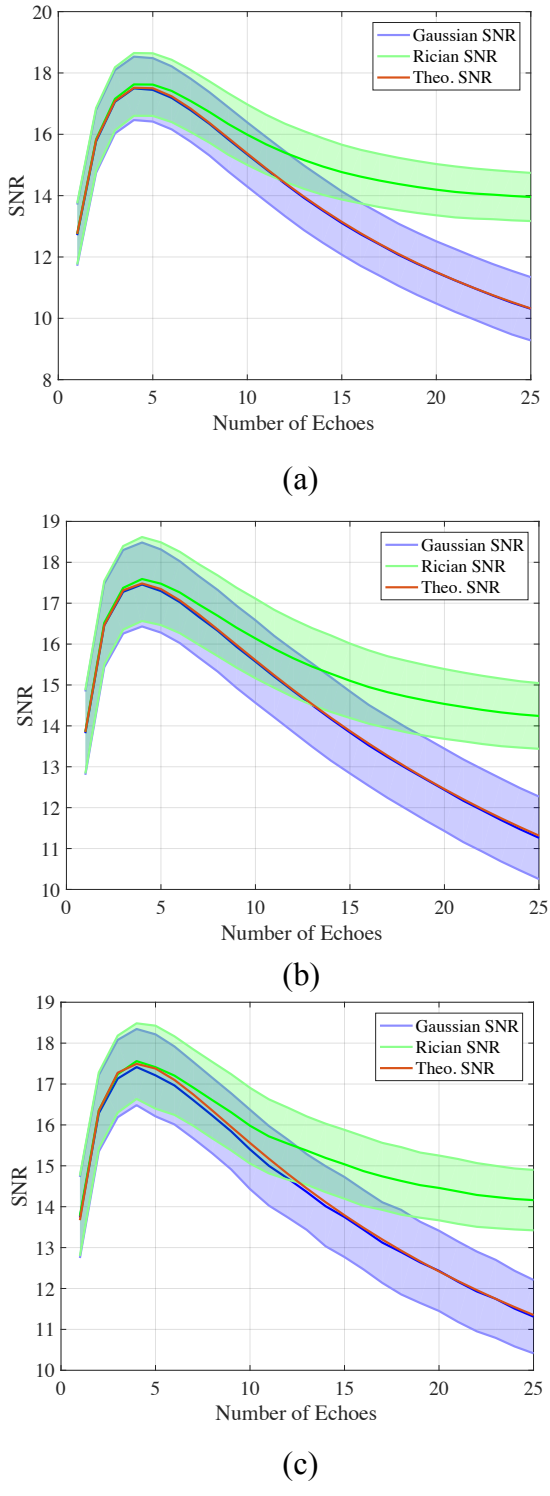

Figure 5.1: Overall gain in SNR plotted against number of averaged echoes. Experimental parameters are derived from the sodium ROI analysis. Theoretically determined SNR curves (red) are overlaid with SNR curves (mean±std) using Gaussian (blue) and Rician (green) noise model. SNR curves obtained using (a) ME, (b) BE and (c) GA model parameters.

Table 5.1: SNR gain and optimal number of averaged echoes using ME signal model.

s (ms)	T_2 (ms)	$\frac{\text{SNR}_n}{\text{SNR}_0}$	n_{opt} (echoes)	$\hat{n}_{\text{opt}}$ (mean ± std) (echoes)	
				σ = 5.0e-2	σ = 5.0e-3
5	10	1.14	3	2.60 ± 0.56	2.89 ± 0.31
	25	1.57	6	6.26 ± 0.96	6.04 ± 0.19
	100	2.92	25	25.04 ± 2.51	25.22 ± 0.61
10	10	1	1	1.21 ± 0.40	1.00 ± 0.00
	25	1.22	3	3.25 ± 0.59	3.00 ± 0.00
	100	2.12	13	13.12 ± 1.61	12.6 ± 0.49
20	10	1	1	1.00 ± 0.00	1.00 ± 0.00
	25	1.02	2	1.75 ± 0.44	2.00 ± 0.00
	100	1.57	6	6.39 ± 0.98	6.09 ± 0.27

n_{opt} and the corresponding SNR gain was well-predicated by all models.

SNR Maps

SNR maps generated through voxelwise echo averaging and normalization show significant improvement in SNR as compared to that at the first echo (Figures 5.4-5.7). Additional structural details are visible in all averaged images of sodium MRI data (Figure 5.4- 5.5). The SNR map obtained using empirically determined n_{v}^* (Figure 5.4b) has superior SNR as compared to averaged SNR maps using n_{g}^* (Figure 5.4c-d). We consider the SNR map in Figure 5.4b as the benchmark and evaluate the performance of other averaging methods against it. The difference images between the benchmark map and averaged maps using n_{g}^* are displayed in Figure 5.4e-f. Tissue regions in the all-echo averaging map (Figure 5.4c) appear darker, indicating decrease in the SNR gain due to inclusion of low intensity later echoes, as evidenced by the difference image (Figure 5.4e). It is difficult to visually identify SNR differences between the benchmark map and the averaged image using n_{g}^*=4 echoes (Figure 5.4d), but the difference image (Figure 5.4f) shows that voxelwise averaging outperforms averaging using n_{g}^* in certain areas of the tissue. SNR maps achieved through model-based weighting functions (Figure 5.5a-c) demonstrate that all models yield equivalent results which are comparable to the benchmark SNR map in Figure 5.4b.

SNR maps generated though voxelwise echo averaging methods for the rat brain

Table 5.2: SNR gain and optimal number of averaged echoes using BE signal model. The volume fraction, f, is fixed at 0.5.

s (ms)	$(T_{2\,a}, T_{2\,b})$ (ms, ms)	$\frac{\mathrm{SNR}_n}{\mathrm{SNR}_0}$	n_{opt} (echoes)	$\hat{n}_{\mathrm{opt}}$ (mean ± std)(echoes)	
				σ = 5.0e-2	σ = 5.0e-3
5	(25, 50)	1.80	9	9.32 ± 1.39	9.08 ± 0.28
	(25, 100)	2.07	15	15.50 ± 2.59	15.25 ± 0.58
	(50, 100)	2.47	18	18.55 ± 2.19	18.43 ± 0.54
10	(25, 50)	1.37	5	4.67 ± 0.85	4.75 ± 0.43
	(25, 100)	1.54	7	7.56 ± 1.63	7.32 ± 0.47
	(50, 100)	1.80	9	9.35 ± 1.42	9.08 ± 0.28
20	(25, 50)	1.10	2	2.32 ± 0.50	2.00 ± 0.00
	(25, 100)	1.19	3	3.68 ± 0.92	3.47 ± 0.45
	(50, 100)	1.37	5	4.65 ± 0.85	4.75 ± 0.43

Table 5.3: SNR gain and optimal number of averaged echoes using GA signal model.

s (ms)	(k, θ) (a.u., a.u.)	$T_{2\,\mathrm{GA}}$ (ms)	$\frac{\mathrm{SNR}_n}{\mathrm{SNR}_0}$	n_{opt} (echoes)	$\hat{n}_{\mathrm{opt}}$ (mean ± std)(echoes)	
					σ = 5.0e-2	σ = 5.0e-3
5	(3.33, 3.00e-2)	10	1.18	3	3.19±0.68	3.00±0.00
	(17.00, 2.35e-3)	25	1.59	7	6.75±1.13	6.65±0.48
	(4.54e2, 2.20e-5)	100	2.93	25	25.5±2.73	25.18±0.59
10	(3.33, 3.00e-2)	10	1	1	1.58±0.52	1.68±0.47
	(17.00, 2.35e-3)	25	1.23	3	3.44±0.65	3.00±0.00
	(4.54e2, 2.20e-5)	100	2.12	13	12.59±1.49	12.79 ±0.41
20	(3.33, 3.00e-2)	10	1	1	1.00±0.00	1.00±0.00
	(17.00, 2.35e-3)	25	1.03	2	1.78±0.46	2.00±0.00
	(4.54e2, 2.20e-5)	100	1.57	6	6.47±1.01	6.09 ±0.29

data further reinforce the inferences from the sodium MRI data. The SNR maps

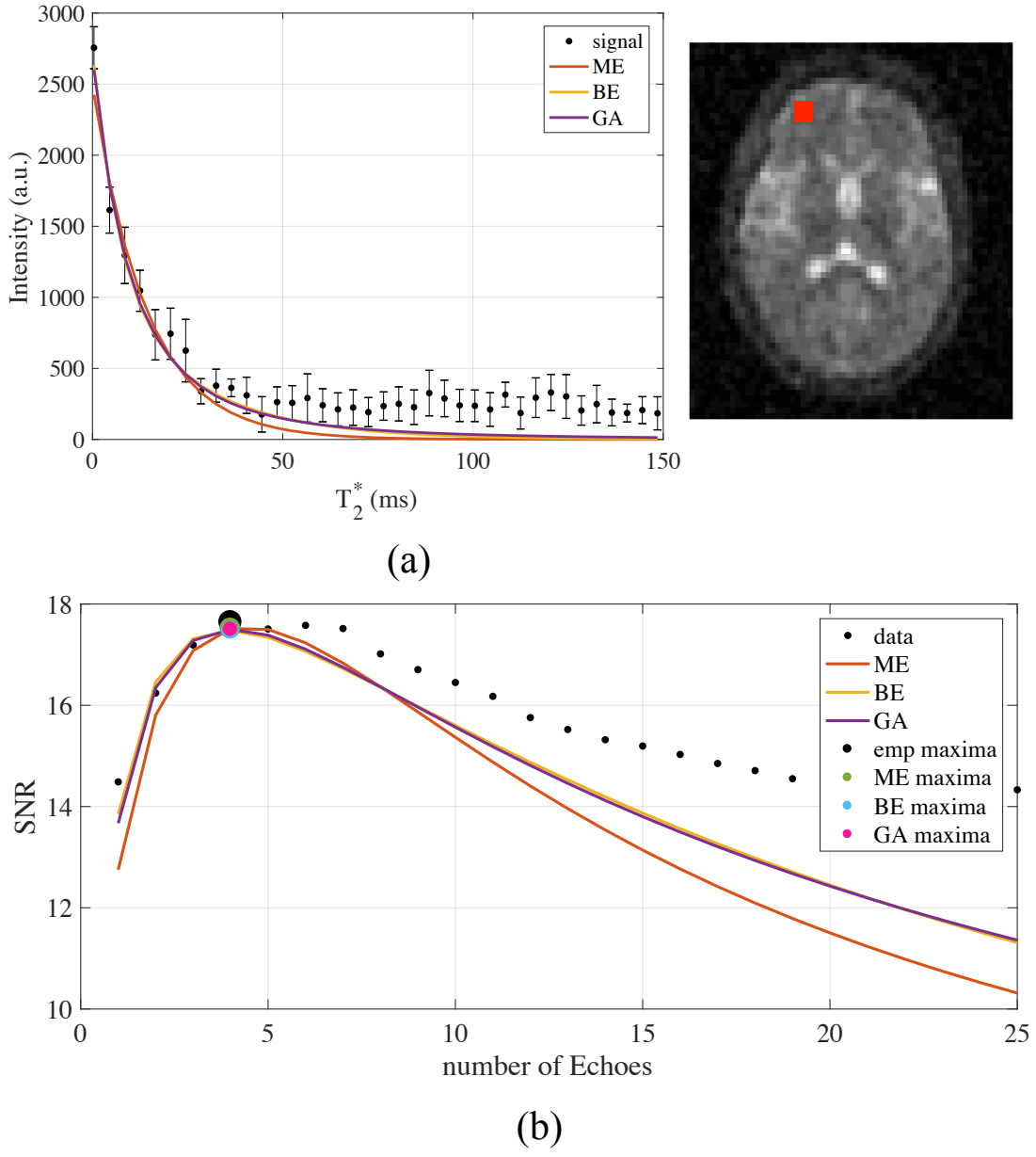

Figure 5.2: (a) ROI data in sodium MRI images of subject 1 (mean±std), overlaid with curve-fits from ME (Red), BE (yellow) and GA (purple) models. (b) Gain in SNR by multi-echo averaging. Empirical SNR curve across number of echoes (dotted line), overlaid with theoretical SNR curves from ME (Red), BE (yellow) and GA (purple) models. Maximum empirical SNR achieved at $n_{\text{opt}} = 4$ echoes (black dot). Theoretically calculated n_{opt} assuming ME (green), BE (blue) and GA (pink) models.

from the rat brain are shown in Figure 5.6. Significantly smaller SNR is observed in the first echo map (Figure 5.6a) as compared to the SNR in the averaged maps. WM structures are more prominent and visible in the averaged images. Similar to the sodium MRI analysis, we selected the voxelwise averaged signal using empiri-

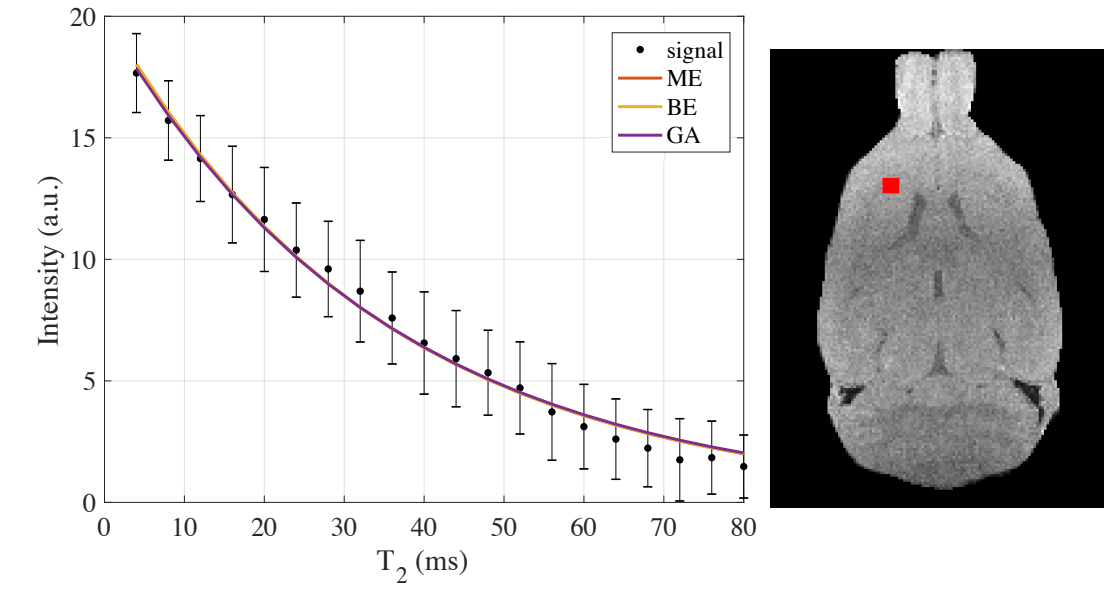

(a)

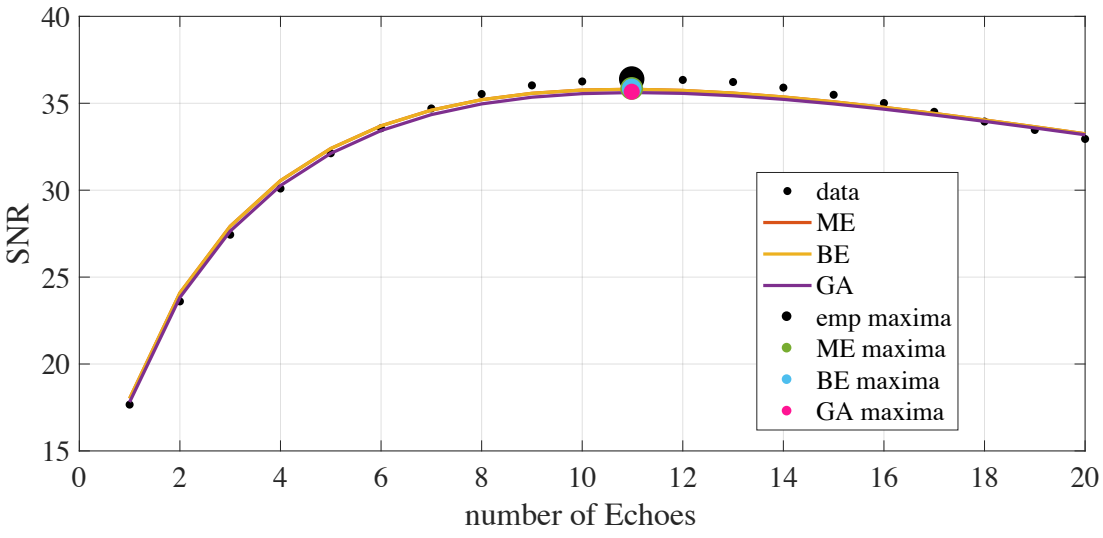

(b)

Figure 5.3: (a) ROI data in rat brain MRI images (mean±std), overlaid with curve-fits from ME (Red), BE (yellow) and GA (purple) models. (b) Gain in SNR by multi-echo averaging. Empirical SNR curve across number of echoes (dotted line), overlaid with theoretical SNR curves from ME (Red), BE (yellow) and GA (purple) models. Maximum empirical SNR achieved at $n_{\text{opt}} = 11$ echoes (black dot). Theoretically calculated n_{opt} assuming ME (green), BE (blue) and GA (pink) models.

cally determined n_{opt} as the benchmark and measure the SNR properties of other maps against it (Figure 5.6b). Significant loss of SNR is observed in the WM

regions of the averaged map using all echoes (Figure 5.6c), as further evidenced by the difference image in Figure 5.6e. The averaged image using the first 10 echoes (Figure 5.6d) has less SNR in CSF regions as compared to the benchmark image. Model-based voxelwise averaged maps (Figure 5.7a-c)show comparable performance to the benchmark map and provide high SNR maps, with the only exception of the GA model map which shows SNR attenuation in the CSF regions.

Comparison of $n_{\mathbf{g}}^*$ and $n_{\mathbf{v}}^*$

We investigate the effect of using a constant number of echoes for the averaging operation on the range of T_2 values. To this end, we plotted the ratio $\mathrm{SNR}_n/\mathrm{SNR}_0$ from the ME model against the number of echoes and T_2 values. Here ME model is selected for ease of visualization offered by a single parameter model and the fact that all models show equivalent performance given a decay signal arising from the same voxel. Employing a constant number of echoes for averaging might lead to attenuation in voxels with T_2 value below a certain threshold. For instance, n_{opt} was fixed at 4ms and 38ms in the n_{g}^* averaged sodium data, leading to SNR attenuation in voxels described by T_2 <6.5, 22.5ms (Figure 5.8a). Similarly, in the averaged rat brain data with n_{g}^*=10, 20ms, SNR attenuation occurs in voxels with T_2 <16, 20 ms, respectively (Figure 5.8b). In contrast, voxelwise averaging methods ensure that appropriate n_{opt} is used for each voxel, thus avoiding the chance of SNR attenuation, as evidenced by the experimental results.

5.4 Discussion

We have demonstrated that SNR improvement through averaging multiecho MRI data is strongly dependent on the number of echoes employed in the averaging process. Averaging an ill-advised number of echoes results in suboptimal SNR improvement, or even signal attenuation. We have developed a model-based technique to perform voxelwise, tissue-dependent SNR optimization. Our results demonstrate that both exponential and non-exponential models perform equally well in optimal echo averaging. When a voxelwise model-fit is used for parameter estimation and subsequent averaging, it should be kept in mind that inaccurate parameter estimation will lead to incorrect averaging. For instance, the gamma model suffered from sub-optimal estimation performance in the CSF region of the rat brain, that directly effected the averaging procedure.

Averaging methods presented in this chapter are applied on the magnitude data but they are easily translatable to complex or k-space data. The k-space echo averaging technique, MEFIC (Multiple Echo Frequency-domain Image Contrast), performs a complex Fourier transform along the echo dimension to produce SNR optimized T_2-weighted images (Yang et al., 1999; Sharief and Johnson, 2006). Due to linearity of the averaging operation, this is equivalent to performing averaging in the complex image domain.

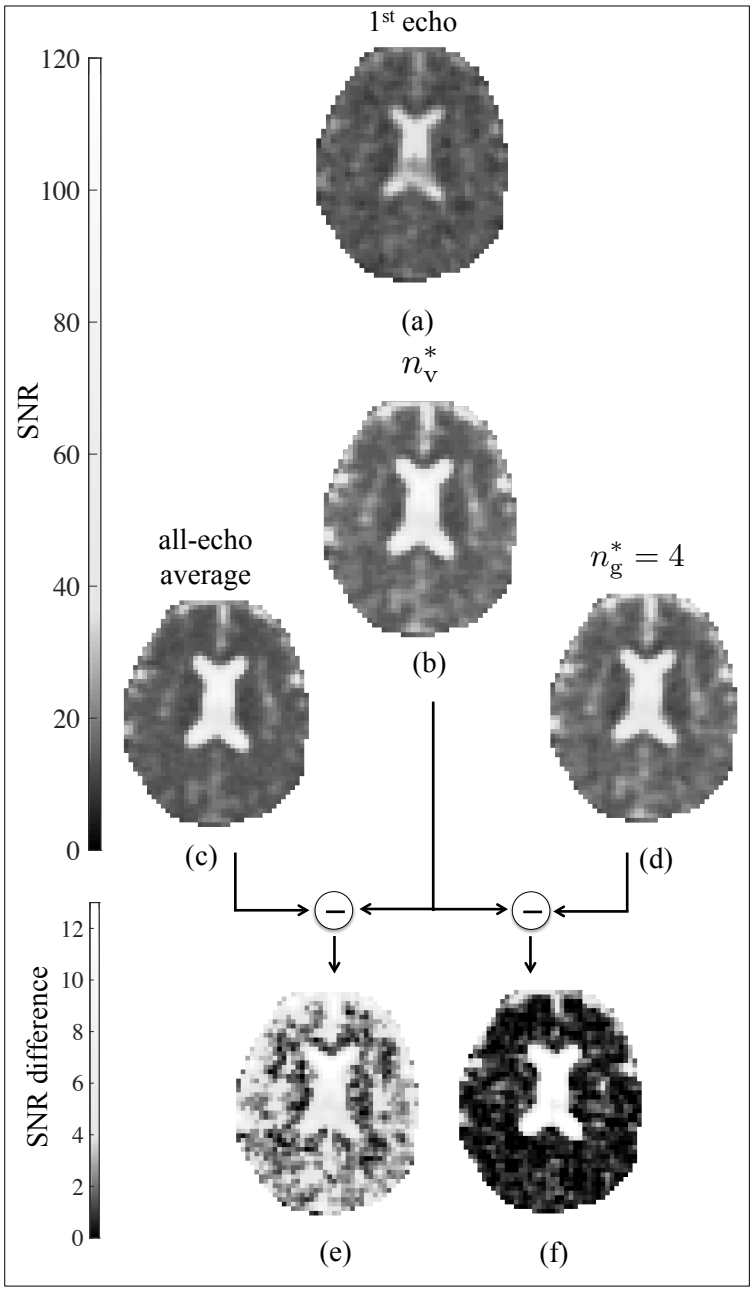

Figure 5.4: Top panel: (a) An axial slice from sodium MRI data at $t_0 = 0.04$ms (first echo). Corresponding SNR maps using (b) all echoes, (c) first 4 echoes, (d) n_{opt} calculated empirically and through voxelwise (e) ME, (f) BE and (g) GA model-fits. Note: Accentuated shades of white are used in the colorbar for ease of visualization. Bottom panel: Difference maps. SNR differences between composite images using empirically calculated n_{opt} and (a) all echoes, (b) first 4 echoes. Note the non-linear colorbar for ease of visualization.

Model-based averaging methods presented here offer increased flexibility due to both exponential and non-exponential model support. This is especially advan-

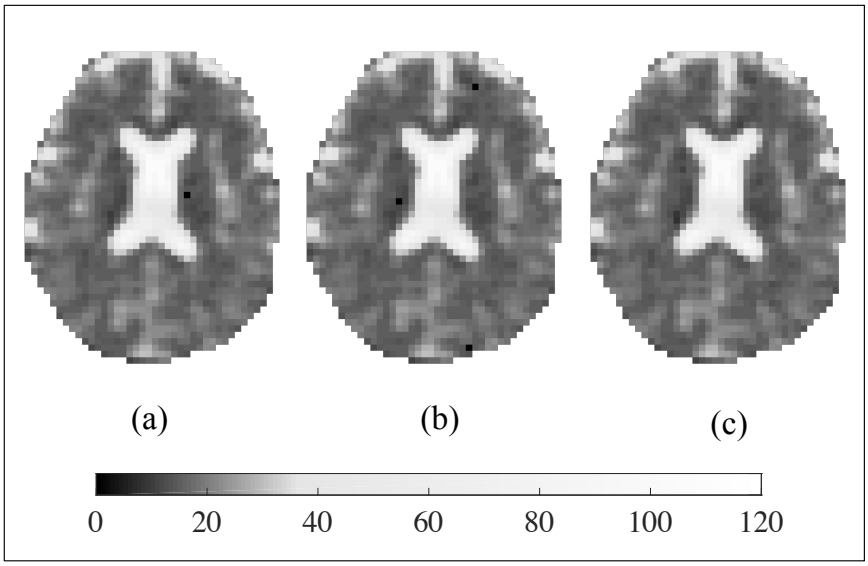

Figure 5.5: SNR maps of an axial slice from the sodium MRI dataset using n_{opt} calculated by voxelwise (a) ME, (b) BE and (c) GA model-fits.

tageous in situations where weighted averaging is performed on multiecho data for increasing sensitivity to a particular contrast mechanism, such as the heuristic signal weighting employed for increasing sensitivity to BOLD, susceptibility weighted or CEST based contrasts (Posse et al., 1999; Wu et al., 2012; Bhavsar et al., 2014; Schmiedeskamp et al., 2010). The T_2-weighted signal arising from complex cellular structures is well-known to exhibit non-exponential decay. By incorporating signal models such as the bi-exponential and gamma distribution models employed in this chapter, more accurate weighting can be incorporated in the multiecho data.

It is well-known that performing a magnitude operation on complex image data changes the noise distribution from Gaussian to Rician (Sijbers et al., 1998). This introduces a magnitude bias at low SNR, causing the measured intensity to deviate significantly from the true signal magnitude value. This bias in Rician-distributed data is aggravated further in averaged multiecho data, where the addition of highly biased latter echoes artificially produces higher SNR. Hence, the resultant SNR values are false and may lead to fictitious contrast variations. We have demonstrated that both Gaussian and Rician-distributed noise models yield equal SNR gain when an optimised number of echoes are averaged. This is an important result as there is a widespread belief that the bias due to averaging Rician noise limits the overall SNR gain (Tu et al., 2014). We have shown in both simulations and experiments that this is not the case for the voxelwise n_{v}^{*} scheme, in which the averaging process is tailored to achieve optimized SNR gain; the bias only becomes a problem if later echoes are introduced in the averaging operation.

Prior to performing voxelwise averaging, parameter estimation must be carried out in order to achieve optimal SNR. The additional information available through

estimation has the potential to offer greater insight into tissue structure, but voxelwise estimation is a computationally expensive and time consuming process. In time and resource sensitive applications, expected parameter estimates based on prior knowledge can be employed, such as suggested in (Posse et al., 1999). This approach, although sub-optimal, still results in tissue-dependent SNR optimization, leading to more precise inference. Our methods can be applied before or after data acquisition.

5.5 Conclusion

Echo averaging is widely used in MRI applications for SNR and contrast enhancement. However, understanding the impact of averaging multiple echoes on the underlying signal strength and distribution is of vital importance. In this chapter, we investigated the importance of employing correct number of echoes in the averaging process to obtain tissue-optimized SNR improvements. We have presented methods for straight-forward determination of the optimum number of echoes. Through application to low intensity and high noise MRI data, we have demonstrated a practical method for achieving significant SNR improvements, and have shown that exponential and non-exponential models can be used while still correctly identifying the optimized echo average. The practical equivalence of Gaussian and Rician noise distributions for the purpose of optimized echo averaging was shown.

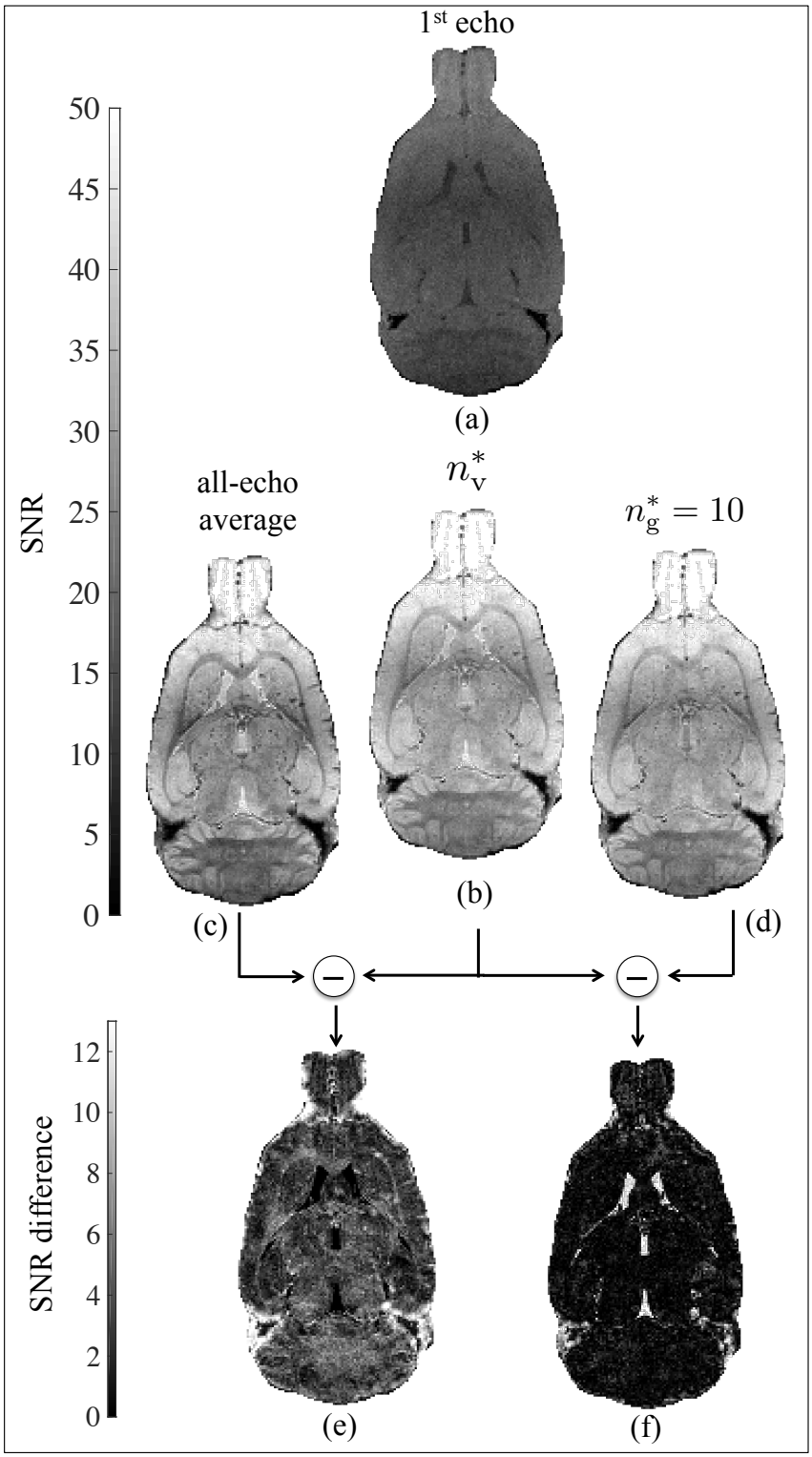

Figure 5.6: Top panel: (a) An axial slice from the rat brain dataset at $t_0 = 4$ms (first echo). Corresponding SNR maps using (b) all echoes, (c) first 4 echoes, (d) n_{opt} calculated empirically and through voxelwise (e) ME, (f) BE and (g) GA model-fits. Bottom panel: Difference maps. SNR differences between composite images using empirically calculated n_{opt} and (a) all echoes, (b) first 10 echoes.

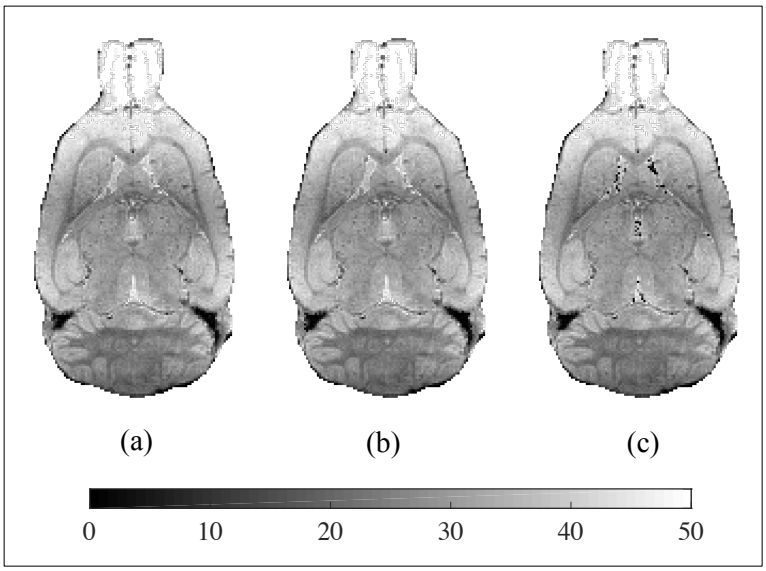

Figure 5.7: SNR maps of an axial slice from the rat brain dataset using n_{opt} calculated by voxelwise (a) ME, (b) BE and (c) GA model-fits.

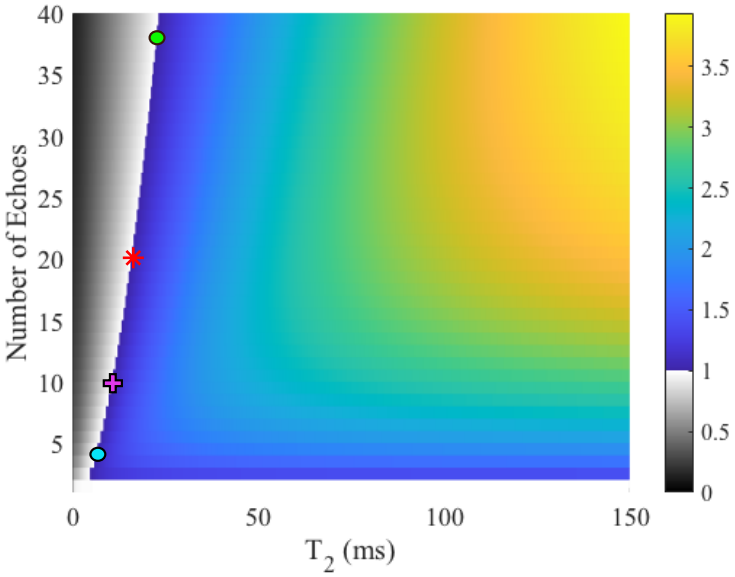

Figure 5.8: The ratio $\text{SNR}_n/\text{SNR}_0$ plotted against a range of n_{g}^* and T_2^* values. Performing global averaging using n_{g}^* attenuates SNR in voxels with T_2^* values below a certain threshold. SNR attenuation when $\text{SNR}_n/\text{SNR}_0 < 1$ (gray region) and SNR improvement when $\text{SNR}_n/\text{SNR}_0 > 1$ (colored region). Symbols mark attenuation threshold for various values of n_{g}^* used in experimental datasets. (a) Sodium data conditions, $t_0 = 0.04$ms. Attenuation in SNR of T_2^* values below 6.5ms at n_{g}^*=4 (cyan circle) and below 22ms at n_{g}^*=38 (green circle). (b) Rat brain data conditions, $t_0 = 4$ms. Attenuation in SNR of T_2^* values below 15.5ms at n_{g}^*=10 (purple plus sign) and 20ms at n_{g}^*=20 (red star sign).

CHAPTER
SIX

Performance Metrics for Multicompartment Models: Application to ADC estimation

6.1 Introduction

The output of an analysis of MRI data is often spatial maps of parameter estimates, the result of having applied a model to the observed data, eg. the regression weights in a General Linear Model analysis of fMRI data, relaxation parameter maps inferred from multiecho data, or the many parameter maps that are output from model-based analyses of diffusion weighted data. The utility of a parameter map is typically determined by its discrimination capability of contrast between, and homogeneity within, regions. Furthermore, statistical analyses are most often employed to determine group level differences between the parameters. Therefore it is easy to neglect the check that the models are actually robust and meaningful.
It is our conjecture that assessment of model fit is a crucial component of parameter estimation in MRI analyses. Without due respect paid to verifying model fit, parameter maps may become nothing more than pretty, yet meaningless, pictures. In order to demonstrate the need for model fit assessment, and to propose an appropriate framework to carry out this assessment, we focus on the estimation of Apparent Diffusion Coefficient maps from models of the diffusion decay signal.

Free diffusion of water in DW-MRI is characterized by a single Apparent Diffusion Coefficient (ADC) and gives rise to an exponential signal decay across b-values, equivalent to a Gaussian decay process across q-space. Accurate estimation of ADC is important for studying tissue development, classification and disease detection (Bihan et al., 1986). Although a single exponential decay is a sufficient description for free, unrestricted diffusion, in reality water molecules diffuse in multiple complex cellular environments, thereby undergoing hindered or restricted diffusion, which is well-known to lead to non-exponential signal decay (Beaulieu, 2002). Parametric models to account for the effects of cellular environment on the diffusing spins can be categorized in two basic groups, multicomponent and non-gaussian models, according to the description of the diffusion displacement profile.

Multicomponent models assume that the spins are diffusing in two or more isolated cellular compartments, with each component described by a different ADC value corresponding to a distinct Gaussian diffusion displacement distribution. The commonly used bi-exponential model is a two-component model with two discrete ADC values, often attributed to hindered and restricted compartments, as employed in the Composite Hindered and Restricted Model of Diffusion (CHARMED) approach (Assaf et al., 2004). The bi-exponential model can be extended to multi-exponential model by including three or more diffusion compartments in the tissue (Barazany et al., 2009; Zhang et al., 2012).

In contrast to compartment ADC models are the continuum models of ADC, as first proposed by Yablonskiy et al (Yablonskiy et al., 2003), in which the complex tissue micro-architecture results in a continuum of diffusion compartments each with a distinct ADC. Thus a continuum ADC (cADC) model is an infinite sum of Gaussian components. This continuum idea was exploited in a two parameter

gamma distribution model of the ADC (Johnston et al., 2011), used to describe restricted diffusion in white matter. Recently, the gamma distribution model has been applied to model the diffusion profiles of normal and cancerous prostate tissues (Oshio et al., 2014), assessment of renal function (Yamada et al., 2016), study of ischemic changes in brain tissue (Grinberg et al., 2014), WM parameter estimation (Pisharady et al., 2017) and characterization of water diffusion in heterogeneous biofilms through NMR (Herrling et al., 2017).

We consider also the popular diffusion Kurtosis (DK) model as an ADC model of non-Gaussianity (Jensen et al., 2005). DKI has been used extensively in clinical applications as a diagnostic imaging tool to evaluate neurological disorders including stroke (Hui et al., 2012), Alzheimer's disease (Lu et al., 2006), schizophrenia (Ramani et al., 2007), glioma (Raab et al., 2010; Cauter et al., 2012), Parkinson disease (Wang et al., 2011) and attention deficit hyperactivity disorder (Helpern et al., 2007). Here we examine how robust and meaningful the DK model is compared to its component and continuum counterparts.

When an assessment of model accuracy is made, mean square error (MSE) is used to quantify how accurately the inference fits the experimental data (Scherrer et al., 2016). MSE is only meaningful for Gaussian noise, and is replaced by Maximum Likelihood (ML) when the noise is Rician (Bouhrara et al., 2015). It is evident, however, that some parameter maps are more meaningful than others; a model can be very accurate, but the parameter maps are highly speckled and seemingly noisy (Layton et al., 2013), again returning to this notion that an efficacious parameter map displays some form of spatial consistency: smoothness within regions and contrast between them. Thus the variability in parameter estimates must be taken into account when assessing the goodness of model fit.

Variability of parameter estimates has been quantified empirically using metrics such as the coefficient of variation (Kurugol et al., 2017; Syeda et al., 2017), the inverse of the standard deviation of estimation error over multiple model fits (Harms et al., 2017), or any other variety of variance-derived quantity. Beyond empirical measures of variability, the information theoretic Cramer Rao lower bound (CRLB) provides a lower limit on the variance of parameter estimates, given a signal model and associated noise properties (Thomas and Cover, 1991). The CRLB is given by the diagonal entries of the inverse Fisher Information Matrix. Thus meaningful parameter estimates (low variability) are given by highly informative models. The CRLB has been applied extensively in diffusion-weighted MRI analyses and design (Alexander, 2008; Basharat et al., 2015; Beltrachini et al., 2013; Farid et al., 2016; Gras et al., 2016; Guyader et al., 2015; Leporq et al., 2015; Majumdar et al., 2011; Poot and Klein, 2015; Sid et al., 2015).

Our previous work has demonstrated that diffusion models suffer from extremely high CRLBs, to the point that parameter estimates are grossly imprecise (Syeda et al., 2017). There is a mismatch, however, between this theoretical result, and

the reality that diffusion parameter maps are produced and reproduced throughout the literature with great success. How then can the CRLB results get it so wrong, and so misrepresent practicality? A key requirement in CRLB analysis is that the model must be 'true'. That is, the model must be able to generate the data, with no unmodelled effects, for the CRLB to be valid. It is well established that without unbiased parameter estimates, the empirical variability may be far less than that predicted by the CRLB (Trees, 1968).

There are two primary reasons why models employed in diffusion-weighted MRI analyses might not be 'true'. Firstly, the complicated biophysics that gives rise to the diffusion-weighted signal may be too difficult to model, despite best attempts to consider microstructural tissue geometry (Beaulieu, 2002). Secondly, and related, is that model abstractions are often preferred in order to simplify behaviour to one or two particular parameters that can provide meaning from an otherwise complex system. It therefore becomes a question of how to quantify precision and information in such cases where unmodelled effects are both present and unknown.

Our measure of precision is an empirical variant of the Fisher Information Matrix known as the Observed Fisher Information (OFI) (Efron and Hinkley, 1978). The OFI characterises the curvature of the log likelihood function at the ML estimate, and is therefore a data-dependent measure of the information content of the model. This is in direct contrast to the CRLB, which implicitly computes an expectation over all loglikelihood curvatures that the model may generate.

The proposed framework, MLOFI, includes both accuracy (ML) and precision (OFI) to determine the goodness of model fit, and a straightforward method by which to compare and contrast the strengths and weaknesses of models when applied to particular instantiations of data. Importantly, our framework is valid regardless of the unbiasedness of the model or any unmodelled effects in the data.

6.2 Models of the Diffusion Weighted Signal

Consider data acquired using pulsed gradient spin echo (PGSE) diffusion weighted MRI. It is well known that spins diffusing in an unbounded medium undergo free diffusion with a Gaussian displacement probability distribution, that results in Gaussian distributed phase from the PGSE preparation. In contrast, in a bounded medium, particles cannot freely diffuse, leading to non-Gaussian phase distributions. The acquired phase distribution causes attenuation of the MR signal, the parametric modelling of which forms the basis of the model comparison methodology we outline herein.

Standard notation for a PGSE acquisition is followed, with q-value defined as $q = \gamma g \delta/(2\pi)$ (μm^{-1}), where γ is the gyromagnetic ratio, g (mT/m) is the diffusion gradient magnitude and δ (ms) is the gradient pulse duration. The b-value (ms/μm^2), often quoted in diffusion-weighted MRI experiments and derived un-

der free diffusion conditions, is $b = 4\pi^2 q^2 (\Delta - \delta/3)$, where Δ (ms) is the duration between the two gradient pulses.

Mono-exponential Model: The mono-exponential model (ME) assumes that the signal decay over b (or q) can be described by a single exponential decay with decay constant, D in $\mu m^2/ms$, as is valid for free diffusion:

$$M^{ME}(b, \boldsymbol{\theta}^{ME}) = e^{-b\,D}, \tag{6.1}$$

where the parameter vector is $\boldsymbol{\theta}^{ME} \triangleq \{D\}$. Thus the ME model can only model Gaussian diffusion arising from a single tissue compartment.

The Bi-Exponential Model: The bi-exponential model (BE) assumes the signal to be comprised of two separate components, often expressed as restricted and hindered diffusion in geometrically complex cellular structures,

$$\begin{aligned} M^{BE}(b, \boldsymbol{\theta}^{BE}) &= f e^{-b\,D_r} + (1-f) e^{-b\,D_h}, \\ \boldsymbol{\theta}^{BE} &\triangleq \{D_r, D_h, f\}, \end{aligned} \tag{6.2}$$

where $0 \leq f \leq 1$ is restricted volume fraction, D_r is the ADC of the restricted component, and D_h is the ADC of the hindered component (Niendorf et al., 1996).

The Diffusion Kurtosis Model: Rather than model non-Gaussian diffusion as a sum of Gaussian diffusion processes as in the BE model, the Diffusion Kurtosis (DK) model accounts for non-Gaussianity using the kurtosis of the diffusion displacement probability distribution:

$$M^{DK}(b, \boldsymbol{\theta}^{DK}) = e^{-bD_{DK} + \frac{1}{6} b^2 D_{DK}^2 K}, \tag{6.3}$$

where K is the apparent diffusion kurtosis of the diffusion displacement probability distribution and D_{DK} is the ADC. Therefore, $\boldsymbol{\theta}^{DK} \triangleq \{D_{DK}, K\}$.

The Gamma Distribution Model: This continuum ADC model assumes that the ADC follows a gamma distribution, $p(D)$, with rate parameter, k, and scale parameter, ζ, rather than being a sum of a discrete number of compartments:

$$p(D, k, \zeta) = \frac{1}{\zeta^k \Gamma(k)} D^{k-1} e^{-D/\zeta}. \tag{6.4}$$

The continuum diffusion decay model can be analytically derived by integration of the signal decay over $p(D)$,

$$\begin{aligned} M^{GA}(b, \boldsymbol{\theta}^{GA}) &= \int e^{-b\,D}\, p(D)\, dD \\ &= (1 + b\,\zeta)^{-k}, \end{aligned} \tag{6.5}$$

The gamma distribution is a suitable choice both given its ability to represent a wide range of ADC profiles and because it makes the integral in (6.5) tractable.

The gamma distribution has mean, $D_{GA} = k\zeta$, and variance, $\nu = k\zeta^2$. Re-parameterization of the above model with D_{GA} and ν leads to

$$M^{GA}(b, \boldsymbol{\theta}^{GA}) = \left(1 + b\,\frac{\nu}{D_{GA}}\right)^{-D_{GA}^2/\nu}, \tag{6.6}$$
$$\boldsymbol{\theta}^{GA} \triangleq \{D_{GA}, \nu\}.$$

This parameterization provides physically intuitive values of the mean and variability of the estimated ADC distribution.

6.3 Methods

6.3.1 The MLOFI Framework

Consider measurements of a diffusion-weighted MRI signal in a voxel, $\mathbf{y} = [y_1, y_2, ..., y_n]^T$, where n indexes b-value. The likelihood function describes the probability of observing $\mathbf{y}$ given a particular model $M^i(b, \boldsymbol{\theta})$ and noise variance σ^2:

$$f(\mathbf{y}|\boldsymbol{\theta}) = \prod_{k=1}^{n} f(y_k|M^i(b_k, \boldsymbol{\theta}), \sigma^2), \tag{6.7}$$

where $i \in \{\text{ME, BE, DK, GA}\}$. For ease of computation, it is convenient to use the log-likelihood (LL) function, defined as

$$\ell\left(\boldsymbol{\theta}; \mathbf{y}\right) = \sum_{k=1}^{n} \ln f(y_k|M^i(b_k, \boldsymbol{\theta}), \sigma^2). \tag{6.8}$$

In Maximum Likelihood estimation, the objective is to find the parameter vector $\boldsymbol{\theta}$ that maximizes the probability of the measurements being generated from the model,

$$\hat{\boldsymbol{\theta}}_{ML} \triangleq \arg\min_{\boldsymbol{\theta}} \; -\ell\left(\boldsymbol{\theta}; \mathbf{y}\right). \tag{6.9}$$

Consider a Taylor series expansion of the LL function about $\hat{\boldsymbol{\theta}}_{ML}$ (dropping the dependence on $\mathbf{y}$ for notational simplicity) (Braunstein, 1992) :

$$\ell(\boldsymbol{\theta}) = \ell(\hat{\boldsymbol{\theta}}_{ML}) + \ell'(\hat{\boldsymbol{\theta}}_{ML})(\boldsymbol{\theta} - \hat{\boldsymbol{\theta}}_{ML}) \tag{6.10}$$
$$+ \frac{\ell''(\hat{\boldsymbol{\theta}}_{ML})}{2!}(\boldsymbol{\theta} - \hat{\boldsymbol{\theta}}_{ML})^2 + ... \tag{6.11}$$

The first derivative of the LL function at the ML estimate is zero, nulling the second term in (6.10). The remaining two non-zero terms in the above expansion form the MLOFI framework, as follows.

Accuracy of ML Parameter Estimates

The constant term in (6.10), $\ell(\hat{\boldsymbol{\theta}})$, is a natural measure of accuracy of the parameter estimate, describing the likelihood that a particular parameter vector of the model generated the data.
For additive white Gaussian noise with variance, σ^2, the negative LL function is

$$\ell(\boldsymbol{\theta}; \mathbf{y}) = \sum_{k=1}^{n} \frac{(y_k - M^i(b_k, \boldsymbol{\theta}))^2}{2\sigma^2}, \tag{6.12}$$

where $M^i(b_k, \boldsymbol{\theta})$ is the i^{th} signal model, with $i \in \{\text{ME, BE, DK, GA}\}$ at the k^{th} b-value. Thus the Gaussian LL function evaluated at the ML estimate is the same as the Mean Square Error (MSE).

Precision of ML Parameter Estimates

The measure of precision, or certainty, of the ML parameter estimate is the coefficient of the third term in (6.10). This second derivative is the curvature of the LL function, also known as the Hessian. From this, the Observed Fisher Information is simply defined to be (Efron and Hinkley, 1978):

$$\mathcal{I}(\hat{\boldsymbol{\theta}}_{ML}) = -\text{diag}(\mathcal{H}(\boldsymbol{\theta}))|_{\boldsymbol{\theta}=\hat{\boldsymbol{\theta}}_{ML}}, \tag{6.13}$$

where

$$[\mathcal{H}(\boldsymbol{\theta})]_{ij} = \frac{\partial^2 \ell(\boldsymbol{\theta}; \mathbf{y})}{\partial\theta_i \partial\theta_j} \tag{6.14}$$

OFI is an empirical quantification of the information in the measurements about the unknown parameter, $\boldsymbol{\theta}$. A parameter with high OFI is more informative and, consequently, more precise and more certain.
The detailed OFI expressions for the Gaussian noise model are given in Appendix 6.A.

6.3.2 Cramer Rao Lower Bound

In contrast to the OFI that quantifies the certainty of a parameter estimate given measured data and a model, the Fisher Information Matrix (FIM) is the expected value of the Fisher information over all possible likelihood curvature values of a given model,

$$[\mathbf{I}(\boldsymbol{\theta})]_{ij} = -E\left\{\frac{\partial^2 \log(f(\boldsymbol{y}, \boldsymbol{\theta}))}{\partial\theta_i \theta_j}\right\}. \tag{6.15}$$

The diagonal elements of FIM are the expected Fisher information in each model parameter. The celebrated Cramer Rao Lower Bound (CRLB) provides a lower bound on the variance of an unbaised estimator, and is given by the diagonal entries of the inverse of the FIM. Specifically, let $\tilde{\boldsymbol{\theta}}$ be any unbiased estimator of an unknown parameter, $\boldsymbol{\theta}$, then under certain regularity conditions on $f(\boldsymbol{y}, \boldsymbol{\theta})$ (see

Appendix 6.B), the CRLB states that the variance of the i^{th} parameter estimator, $\tilde{\theta}_i$, is lower bounded as follows:

$$Var\left(\tilde{\theta}_i\right) \geq \left[\mathbf{I}(\boldsymbol{\theta})^{-1}\right]_{ii}. \tag{6.16}$$

For the Gaussian noise model, the FIM can be calculated from the first derivatives of the signal models, $M^i(\mathbf{b}, \boldsymbol{\theta})$, with respect to each unknown parameter:

$$\left[\mathbf{I}(\boldsymbol{\theta})\right]_{ij} = \frac{\partial M^{iT}}{\partial \theta_i} \boldsymbol{\Sigma}^{-1} \frac{\partial M^i}{\partial \theta_j} \tag{6.17}$$

Derivatives of the ADC models are provided in the Appendix 6.A.

6.3.3 Experiments

Diffusion weighted MRI experiments were run on a 4.7T Bruker BioSpec small bore MRI scanner fitted with a high performance gradient set. A rat brain embedded in agar was scanned using a PGSE-EPI acquisition with TR/TE = 5000/50 ms and multiple b-values in a single direction: b = 100, 200, 300, 400, 500, 1000, 1500, 2000, ..., 6000 s/mm^2, single slice of thickness = 1 mm, matrix = 192×192 and resolution of 167×167 µm^2, $\delta = 6$ ms, $\Delta = 17$ ms, number of averages = 4.

Preprocessing

Two masks of the rat brain data were manually generated. The first mask provided an outline of the whole rat brain. The second mask segmented six regions in the rat brain including Corpus Callsoum (CC), Olefactory Bulb (OB), Thalamus, Cortex, Cerebellar White Matter (CB-WM) and Cerebellar Gray Matter (CB-GM), with reference to the atlas (Lein et al., 2007). A rectangular region of interest (ROI) in the background between the coil and the rat brain was selected as noise region.

Parameter Estimation

The estimation of diffusion model parameters was performed on the magnitude images. Although it is well-known that noise in magnitude images is Rician-distributed (Sijbers and Den Dekker, 2004), analysis of background region showed Gaussian distributed noise, with sufficiently stable parameters across b-values so as to validate the use of an additive white Gaussian noise model. A Gaussian distribution was fitted to background ROI and estimates of mean (μ_{noise}) and variance (σ^2) across b-values were empirically calculated.

For each diffusion model, the ML estimates of the parameter vector were achieved by maximizing the log-likelihood function in (6.12), using a constrained nonlinear least-squares solver in MATLAB. Appropriate lower and upper bounds were employed to ensure components of $\boldsymbol{\theta}$ remain positive, with the only exception being

the kurtosis parameter, K, which can be negative. To find the optimized parameter estimates in each voxel, the estimation routine was run five times per voxel with random initial values in the range $(\boldsymbol{\theta}_{min}, \boldsymbol{\theta}_{max})$ (see Table 6.1). Note that for ease of estimation, the gamma model was fit using parameters (k, ζ), from which estimates of (D_{GA}, ν) were calculated. The corresponding OFI values were calculated using (6.13) (see Appendix 6.A for details).

Table 6.1: Range of initial values of diffusion parameters for ML estimation

Model	Parameter	θ_{min} - θ_{max}
ME	D (μm^2/ms)	0 - 1.0
BE	D_r (μm^2/ms)	0 - 0.5
	D_h (μm^2/ms)	0 - 1.0
	f	0 - 0.5
DK	D_{DK} (μm^2/ms)	0 - 1.0
	K	0 - 1.0
GA	k	0 - 3.0
	ζ	0 - 0.1

Spatial Heterogeneity Index

In order to quantify the heterogeneity of parameter estimates within tissue ROIs, we define an empirical spatial heterogeneity index to be

$$\hat{\sigma}_{\text{emp}} = \sqrt{\overline{(\hat{\theta} - \bar{\theta})^2}}, \tag{6.18}$$

where $\hat{\theta}$ is the ML estimate in a single voxel and $\bar{\theta}$ is the mean of ML estimates in the ROI.

The empirical spatial heterogeneity index is compared with that predicted by the CRLB, via the ratio $\sigma_{\text{CRLB}}/\hat{\sigma}_{\text{emp}}$, where σ_{CRLB} is the square root of the appropriate diagonal element of the inverse Fisher Information Matrix (6.15).

6.3.4 MLOFI Analyses

Voxelwise estimates of ML and OFI for each parameter of each diffusion model were calculated. Parameter-wise MLOFI diagrams were generated as scatter plots of OFI against ML on a log scale. For improved visual quality of MLOFI diagrams, each point in the scatter plot was assigned a weight in the range $\{0, 1\}$ based on the normalized spatial density of points in its neighbourhood. The

point neighbourhood was arbitrarily defined by a circle with radius of 0.2 units on log scale. A point with weight less than 0.4 was considered an outlier and discarded from the plot. Further, each parameter plot was assigned a distinct color gradient, with darker shades for higher spatial densities. ADC parameters $\{D, D_r, D_h, D_{DK}, D_{GA}\}$ were plotted together for comparison, with boundary lines delineating point cloud of each parameter. Similarly, other model parameters $\{f, K, \nu\}$ were plotted on a single diagram.

Figure 6.1 describes the MLOFI plot in conceptual quadrants; a point-cloud situated at the top-left of the MLOFI diagram is both more accurate and more precise than a point cloud in the bottom-right corner.

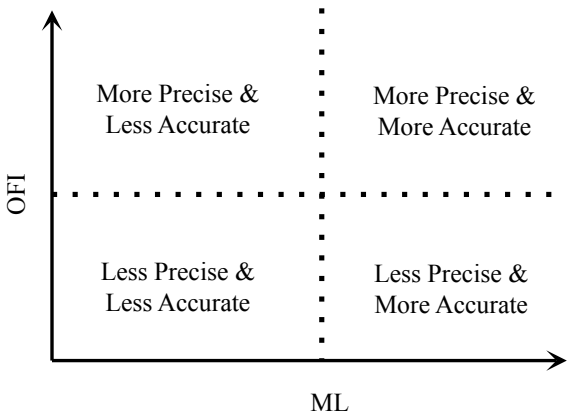

Figure 6.1: Conceptual quadrants of the MLOFI diagram.

6.4 Results

6.4.1 ML Estimation

We first verify that it is appropriate to use a Gaussian noise model for the maximum likelihood estimation algorithm. Noise in a background ROI of the rat brain data shows Gaussian characteristics across b-values; empirical noise distributions for no diffusion weighting and $b = 3500$ s/mm^2 are well-fit by Gaussian distributions (Figure 6.2a). Further, the noise variance is consistent across b-values (Figure 6.2b), validating our assumption of constant noise parameters, μ_{noise} and σ^2, in the parameter estimation algorithm. The tissue signal decay is significantly higher than the background noise signal (Figure 6.2c), which together with the consistency of the noise characteristics demonstrates that the additive white Gaussian noise model is justified.

In order to compare ADC models, it is instructive to determine what evidence can be gleaned from a visualisation of voxelwise model fits. To this end, diffusion decay signals from single voxels in CC, thalamus and CSF, along with the ML model fits are shown in Figure 6.3. It is evident that in CC and CSF, all models

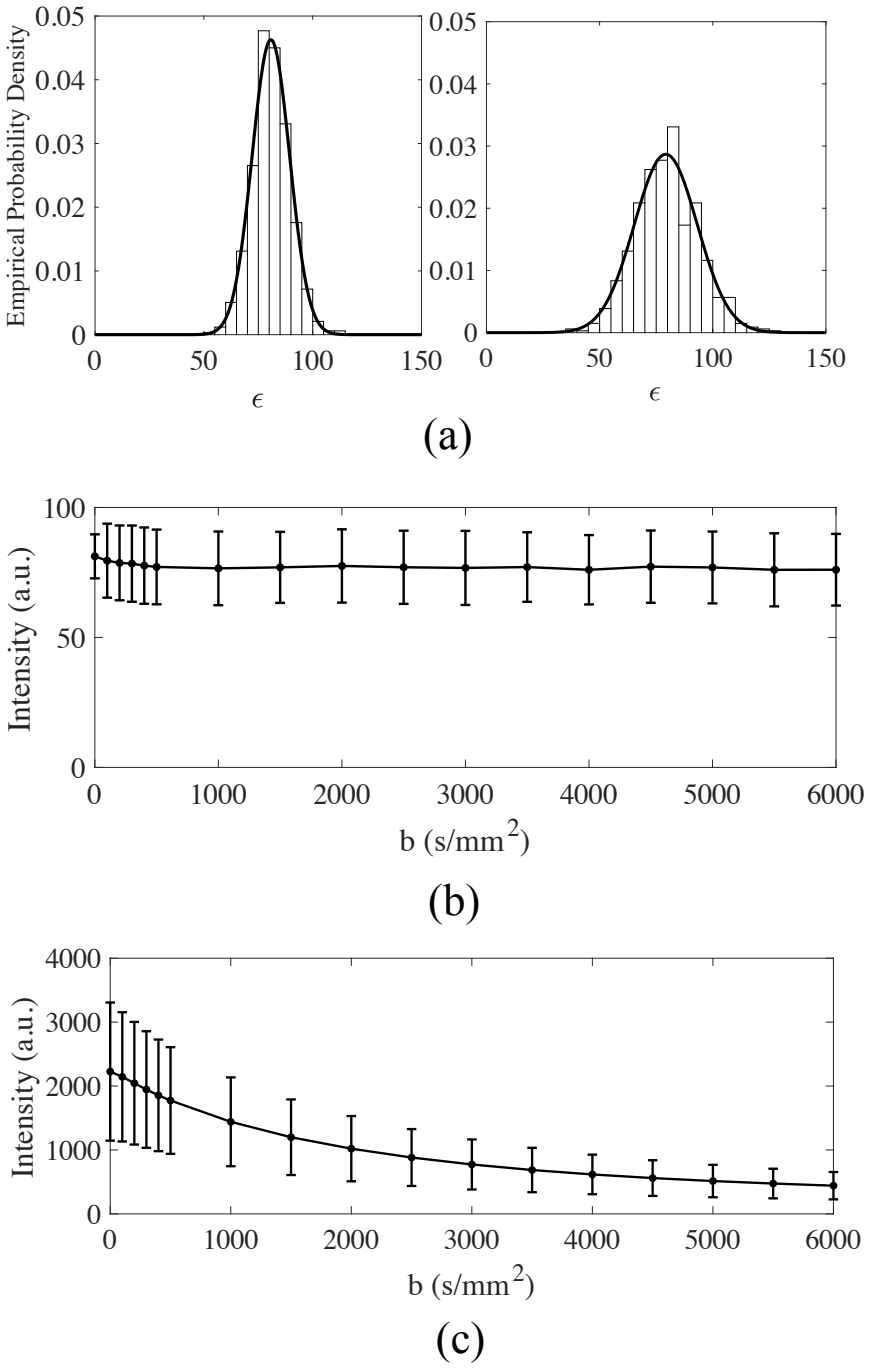

Figure 6.2: (a) Noise distribution in a background ROI, at $b = 0$ (left) and $b = 3500$ s/mm^2 (right). Empirical distribution (histogram) well fit by Gaussian distributions (solid lines). (b) Background noise (mean ± s.d.). The noise characteristics are highly consistent across b-values. (c) Whole brain signal (mean ± s.d.).

fit the data well except the ME model. In particular as expected in WM, the ME model fails to fit data at high b-values, demonstrating its inability to model complex diffusion processes in tissue. All models fit the diffusion signal from thalamus equally well, as evidenced by near identical curves.

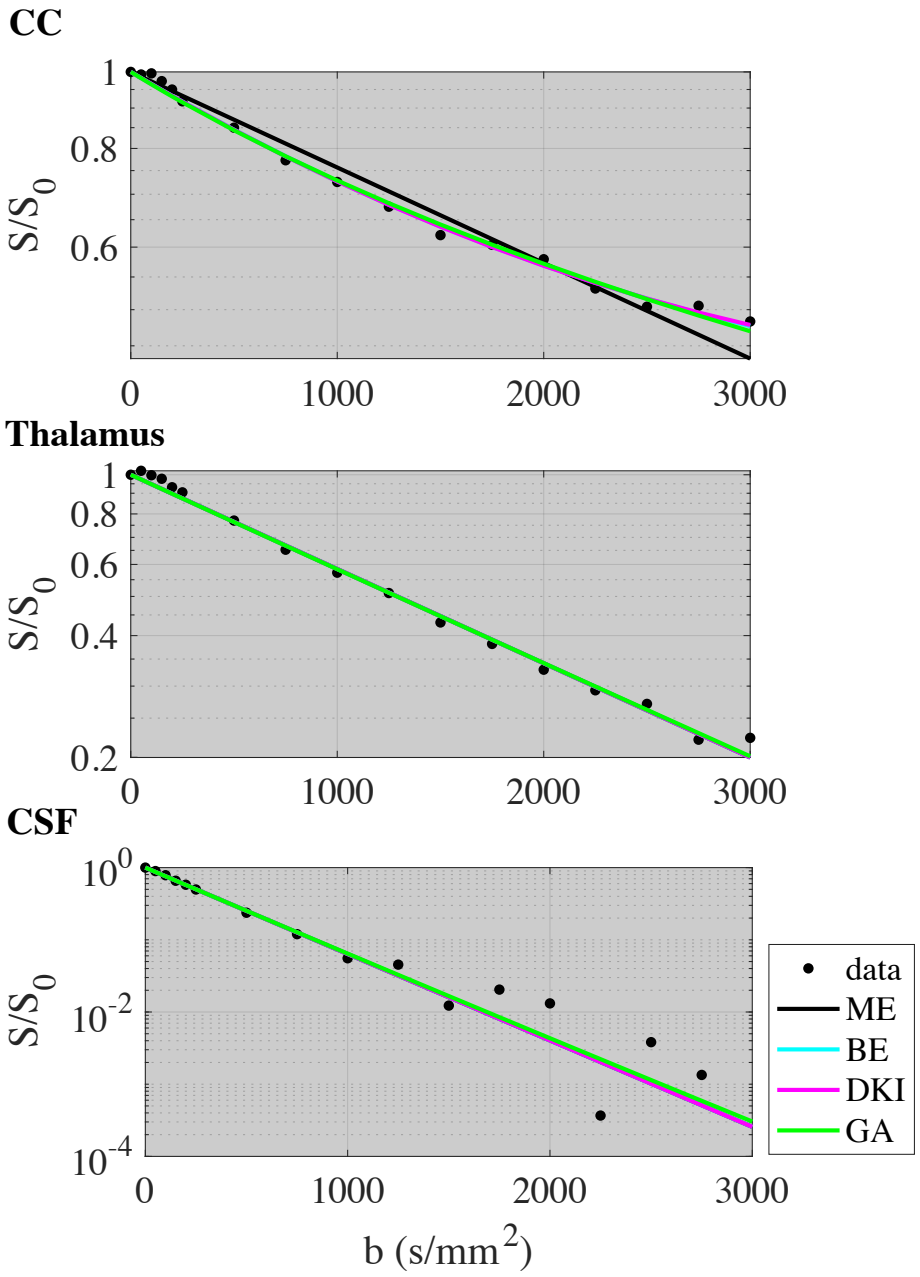

Figure 6.3: Single voxel data in CC, Thalamus and CSF regions of rat brain, overlaid with curve-fits from ME (black), BE (cyan), DK (magenta) and GA (green) diffusion models.

From the visualisation in Figure 6.3 alone, it is difficult to determine how the models compare with each other, beyond the obvious limitations of the mono-exponential model. Plotting the shape of the likelihood function in the vicinity of the ML estimates, however, demonstrates that the similar curve fits are derived from vastly different likelihood functions (Figure 6.4). As depicted in Figure 6.4, the curvature of bi-exponential likelihood function in CC and CSF regions is flat

along the parameter D_r and sharp along the parameter D_h, demonstrating that D_h carries more information than D_r. The reverse is seen to be true in the thalamus. Similarly, the DK likelihood function reveals that the ADC parameter D_{DK} is more informative than the kurtosis parameter, K. The likelihood function for the Gamma model shows similar trends in CC, thalamus and CSF, with the rate parameter, k, carrying more information than the scale parameter, ζ. Interestingly, the ME ADC parameter, D, has a stronger curvature in the thalamus than in CC or CSF, demonstrating that D is more precise in thalamus than WM or CSF.

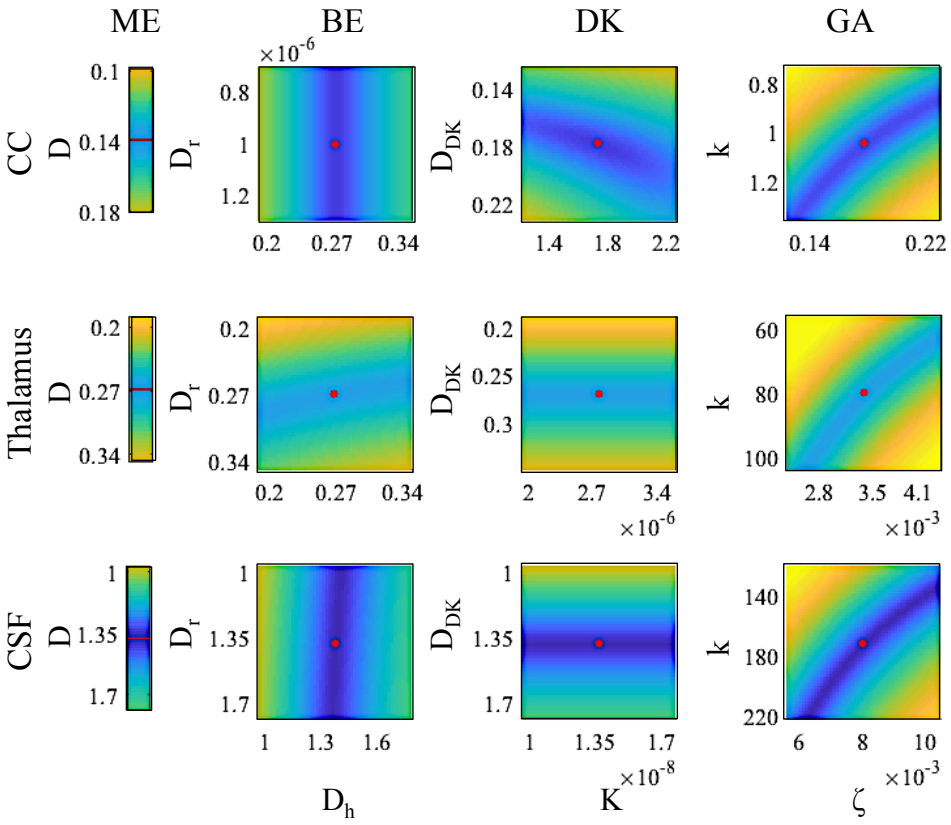

Figure 6.4: Exemplar log-likelihood functions, plotted on a log scale, in CC (top row), Thalamus (middle row) and CSF (bottom row), for ME, BE, DK and GA models. Red dots (or line in the ME column) indicate the ML estimates. Note that for BE model, the log-likelihood function is shown at fixed ML volume fraction value, f_{ML}.

6.4.2 Model Comparison

Parameter maps for each ADC model parameter are displayed in Figure 6.5. The ME model returns a very smooth ADC map, D, while the BE ADC maps are highly speckled, as is the volume fraction map, f. The DK and GA model ADC maps retain the smoothness of the ME, with kurtosis and variance parameter maps showing some structured artifact (Figure 6.5c). Visualisation alone cannot

fully inform model comparison; additional quantitative information is required. The MLOFI diagrams (left of Figure 6.5) summarise the accuracy (ML) and the precision (OFI) of the curve fits, and clearly distinguish the performance of the various models across whole brain.

The top MLOFI diagram in Figure 6.5 compares the ADC parameters from each model. The ADC of the ME model is not surprisingly the least accurate, encompassing the lower ML region on the MLOFI diagram (Figure 6.5a). If only accuracy is considered, the multi-parameter diffusion models $\{\mathrm{BE}, \mathrm{DK}, \mathrm{GA}\}$ exhibit comparable performance. It is in the addition of the OFI dimension that it becomes clear that D_{GA} provides more precise ADC estimates that all other models, reflecting the the sharper likelihood functions of the GA model. Although the D parameter of ME model is the least accurate, it occupies a relatively high OFI region, and therefore the estimates of D are more certain than estimates of D_r, D_h and D_{DK}. This is unsurprising, as the shape of the ME model's LL function ensures a global minimum even if it fails to accurately model the data. The relatively low OFI values of D_{DK}, D_r and D_h are relfective of the flatter LL functions that potentially contain troughs of local minima, resulting in less certainty in parameter estimates.

The MLOFI diagram of the non-ADC parameters (lower panel of Figure 6.5) clearly distinguishes the the GA model's variance parameter, ν, as the most precise, followed by the BE restricted volume fraction, f. The Kurtosis parameter, D_{DK}, is the least precise parameter. Note that the OFI values of these three non-ADC parameters can be directly compared given the same ranges of the parameters.

Region specific MLOFI diagrams

Whole brain MLOFI diagrams are complemented by region-wise MLOFI diagrams, highlighting the differences in models performance across brain regions. The top row in Figure 6.6 compares ADC parameters from each model across WM and GM regions of the brain. Consistent to whole brain MLOFI analysis, the ADC of the ME model is least accurate in all regions, while the other diffusion models show comparable accuracy. Interestingly, the ADC of the restricted component of the BE model is less informative in WM regions than the ADC of the hindered component. This trend reverses in thalamus, with more certainty in restricted ADC estimates. Both components of the BE model show comparable OFI in GM. The ADC parameter of the GA model exhibits consistently higher OFI across all regions of the brain. In contrast, the ADC parameter of the DK model consistently occupies lower OFI regions. The non-ADC parameters show consistent performance across all regions of the brain (Figure 6.6). The variance parameter of the GA model is most informative with higher OFI values, followed by the volume fraction from the BE model. The excess kurtosis parameter of the DK model is the least informative of all with the majority of OFI values less than unity.

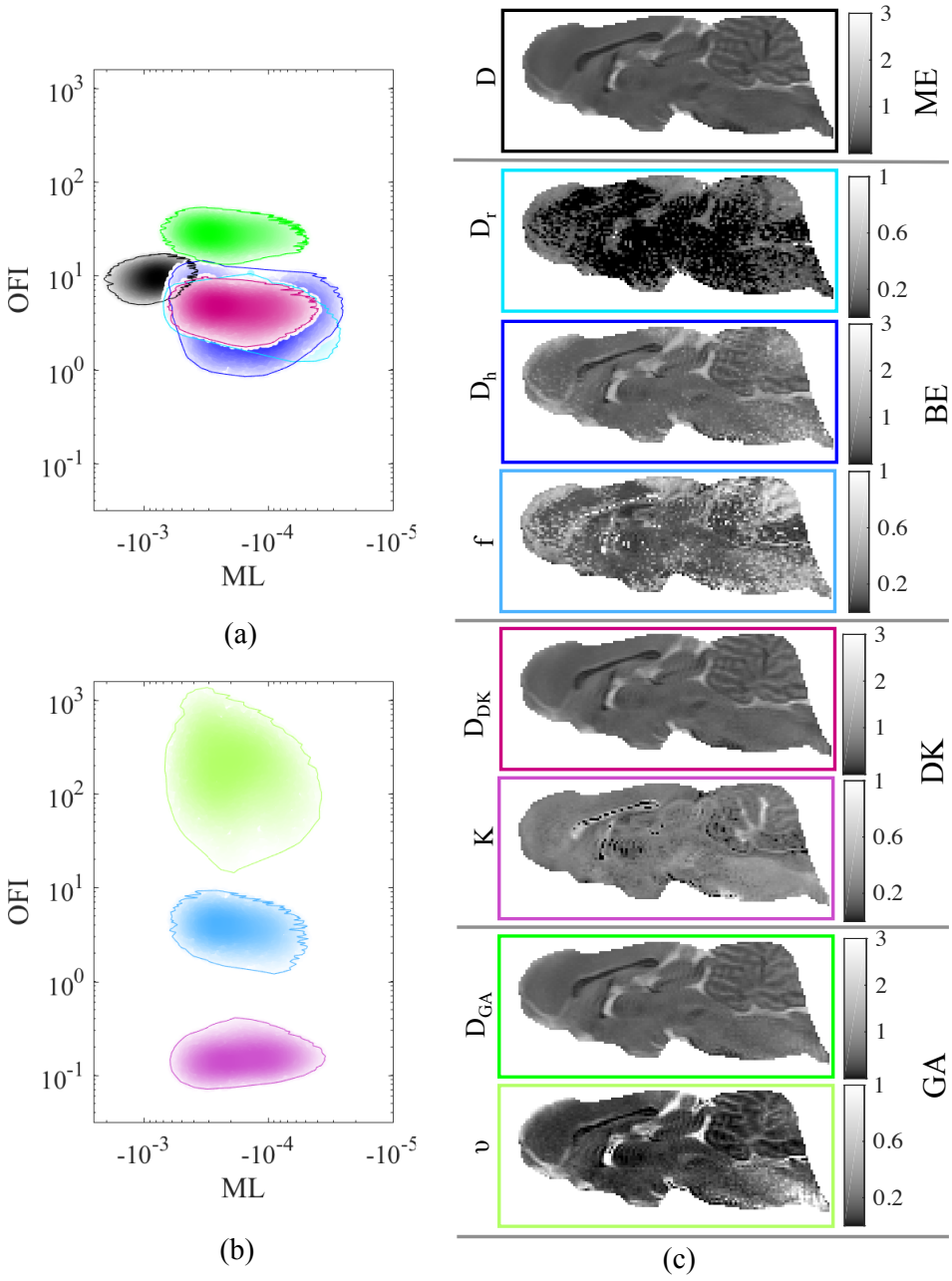

Figure 6.5: MLOFI diagrams and corresponding parameter maps for four diffusion models. (a)-(b) MLOFI diagrams for ADC parameters from diffusion models. (a) MLOFI of D (black), D_h (blue) and D_r (cyan), D_{DK} (magenta) and D_{GA} (green). (b) MLOFI of kurtosis K (magenta), volume fraction f (blue) and variance of the gamma distribution ν (lime). (c) Parameter maps, color coding as per (a)-(b). Note: all color bars start at zero (marking not displayed due to space limitations.)

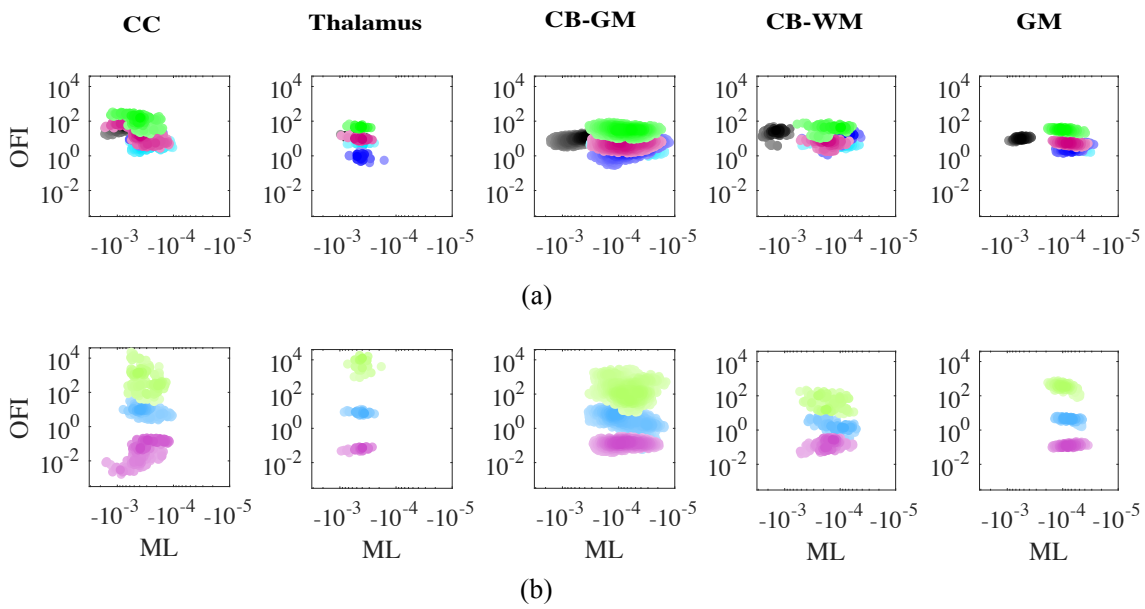

Figure 6.6: Region-wise MLOFI diagrams of rat brain in CC, Thalamus, CB-GM, CB-WM and GM. (a) MLOFI of D (black), D_h (blue) and D_r (cyan), D_{DK} (magenta) and D_{GA} (green). (b) MLOFI of kurtosis K (magenta), volume fraction f (blue) and variance of the gamma distribution ν (lime). The OFI in GA parameters is consistently higher than other diffusion models across the regions.

6.4.3 CRLB versus Empirical Spatial Heterogeneity

As evidenced in Figure 6.7a, the spatial heterogeneity of parameter estimates is both model- and region-specific, reflecting the parameter maps in Figure 6.1. In particular, parameter maps in CC are more spatially heterogeneous than in GM regions (Figure 6.7a). Higher spatial heterogeneity is observed in the kurtosis parameter, K, the BE's hindered ADC, D_h, and restricted volume fraction, f. The D parameter of ME model exhibits lower spatial heterogeneity compared to similar D_{DK} and D_{GA} parameters.

For most diffusion model parameters, the theoretical CRLB calculation provided extremely conservative lower bounds on estimator precision compared to the empirical parameter variability, as demonstrated by very high values of the ratio $\sigma_{\text{CRLB}}/\hat{\sigma}_{\text{emp}}$, for the four diffusion models' parameters across ROIs (Figure 6.7b). The results are plotted on log scale for ease of visualization, with equivalence between empirical and theoretical variability being indicated by the dotted black line in Figure 6.7b). In the thalamus, CB-GM and GM, the CRLB grossly overestimates the degree of variability in the empirical parameter estimates. In WM regions, CRLB is again not predictive of $\hat{\sigma}_{\text{emp}}$, except for D and K parameters in which $\hat{\sigma}_{\text{emp}}$ is higher than σ_{CRLB}.

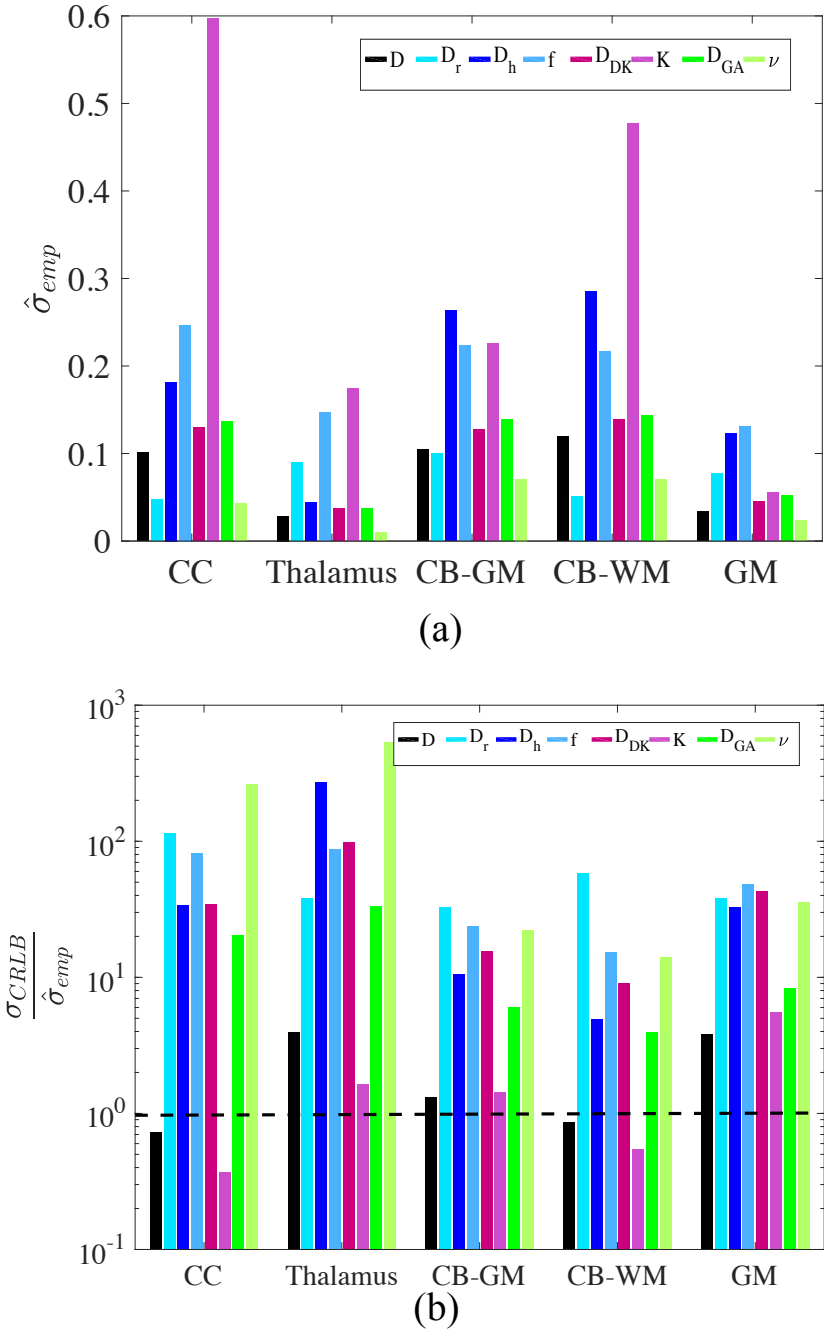

Figure 6.7: (a) Spatial heterogeneity index, $\hat{\sigma}_{emp}$ of diffusion parameters across ROIs. (b) Comparison of theoretical lower bound on variance as given by CRLB and empirical variance. The ratio, $\sigma_{CRLB}/\hat{\sigma}_{emp}$, (plotted on log scale) demonstrates that σ_{CRLB} is not predictive of $\hat{\sigma}_{emp}$, that is, the degree of variability in practical parameter estimates is generally much less than that predicted by the theoretical analysis (with a few exceptions, as discussed in text).

6.5 Discussion

We have demonstrated that a MLOFI analysis of parameter map quality is both straight-forward and meaningful, via quantifying both the accuracy (goodness of fit) and precision (certainty of parameter estimates) associated with a model fit. In certain MRI applications, quality maps are commonplace, for example in fMRI, GLM parameter maps have inherent quality assurance given that model weights are routinely transformed to t- and z-statistics. In diffusion-weighted MRI and other structural imaging areas, measures of quality are far less common. We have demonstrated the importance of performance metrics beyond visualisation of the parameter maps themselves; the mono-exponential model produced a regionally-smooth ADC map, with a high degree of precision, however its accuracy was lacking in comparison with other ADC models, as expected. Conversely, the Diffusion Kurtosis model is sufficiently accurate, but estimates of the kurtosis parameter, K, were seen to be very uncertain. High levels of uncertainty, evidenced by low Observed Fisher Information values, casts reasonable doubt on the conclusions that can be drawn from the parameter maps.

The Information Criterion based approaches to model comparison, such as the Akaike and Bayesian Information Criteria (Akaike, 1974; Schwarz, 1978), provide a scalar that summarises the optimal model for a given set of data. They are limited in their applicability however, as they are more concerned with penalising the number of parameters in a model, rather than the confidence with which those parameters can be estimated. They have found application in order selection of models used in Granger Causality connectivity analyses, for example (Seth et al., 2015), but application to a broad range of biophysical models, such as the ADC models herein, would not be possible using these technqiues. Automatic Relevance Determination (ARD) (MacKay, 1994) is another common model comparison technique that has found application in MRI such as in determining the number of fibres in multitensor models (Behrens et al., 2007). Instead of fitting different models to the data separately, ARD starts by considering a single complex model with large number of parameters and gradually weeds out the irrelevant parameters. In contrast, the generalization error based model selection strategy in (Scherrer et al., 2013) begins with a simple model and minimizes the generalization error through incremental increase in model complexity. Both of these techniques are applied to nested models and are therefore not applicable to the set of non-linear models considered here.

The MLOFI metrics are taken directly from the Taylors series expansion of the likelihood function. The ML value quantifies accuracy of the ML estimate, while the OFI value describes the shape of the LL function in the vicinity of the ML estimate; highly curved LL surfaces result in more certain, more informative parameter estimates (Efron and Hinkley, 1978). Note that this is well known in signal processing theory, however we highlight it's utility to MRI parameter maps given the need for model comparison methods. The LL function can therefore be any noise model, and is equally applicable to Rician as to Gaussian noise charac-

teristics. The Hessian, from which the OFI is derived, can be used to approximate confidence intervals for the parameters (Efron and Hinkley, 1978). For highly nonlinear models such as ADC models, these are approximations only and therefore we determine that the information already present in the OFI is sufficient to provide a measure of precision.

Mean Square Error, a metric often used to quantify curve fits, is only truly valid when the noise is Gaussian. MSE is often decomposed into a bias and variance term, and the relative advantages and disadvantages of models can be expressed with reference to these metrics (Bouhrara et al., 2015). The very notion of bias, however, means that the 'true' parameter values must be known, and thus that the model is 'correct', in the sense that it can be said to generate the observed data. This is clearly not the case for the majority of practical MRI situations, such as the ADC estimation example we present here-in. If there were one ground truth model by which to describe the diffusion-weighted signal, there would not be ongoing research in the area.

The Cramer Rao Lower Bound analysis is a celebrated technique for finding the lowest achievable variance of an estimator (Thomas and Cover, 1991), that has found application in MRI analyses. CRLB is used as a stochastic tool for optimizing MRI experimental setup (Alexander, 2008). Majumdar (Majumdar et al., 2011) proposed a diffusion gradeint optimization framework based on minimizing Rician CRLB on model parameters for uncertainty reduction in estimates. Similarly, CRLB has been applied in optimizing multi-coil diffusion MRI systems (Beltrachini et al., 2013). CRLB is also widely used as a performance comparison tool, for instance, CRLB analysis is employed to evaluate relative performance of two separate image reconstruction methods namely matched filtering and sum-of-squares (Farid et al., 2016).Besides DWI, CRLB has been used to optimized design and sampling strategies for measuring transverse relaxation times (Dula et al., 2009; Jones et al., 1996). The caveat when applying a CRLB analysis is that the model must generate the data. Clearly, in the case of diffusion weighted signal models, all models are abstractions of complex biophysical interactions of water molecules with their surrounding cellular environments. We have shown that the estimator variability predicted by a CRLB analysis bears no relation to the practical reality. We therefore conclude that CRLB should not be used to guide experimental design. Modifications to the CRLB have been introduced to deal with biased estimators (Eldar, 2008), including Bayesian CRLB approaches that weight the expectation implicit in the CRLB toward likely parameter ranges, rather than integrating over all possible model instances (Trees, 1968; Trees and Bell, 2007). These techniques are not applicable as they primarily address the limitations of biased estimators but fail to take into account the impact of unmodelled aspects of the data on parameter variance.

Our MLOFI analysis of ADC models has distinguished the gamma continuum model as the strongest amongst the candidate models. Conversely, some DK and

BE model parameters were shown to suffer from low precision and high spatial heterogeneity. The recently proposed DIAMOND model extends the gamma model to multidirectional dMRI data and was shown to provide more accurate ADC estimates (Scherrer et al., 2016). The concept of continuum component models has previously been applied elsewhere in the MRI literature. The popular NNLS algorithm for T_2 estimation used a nonlinearly spaced set of T_2 components, and in so doing, constructs a pseudo-continuous distribution of T_2 values (Whittall and MacKay, 1989) Layton et al. applied a mixture model with inverse gamma distributed weights to estimate the width of the modes of a multicomponent T_2 distribution (Layton et al., 2013). The AxCaliber method assumes a gamma distributed axon diameter density in ordered WM structures and performs parameter estimation via a grid search algorithm (Assaf et al., 2008).

The notion of spatial heterogeneity in the estimated maps must be considered together with the algorithm tuning parameters, such as the intialisation conditions. Here we randomised initial conditions five times per voxel per model in an attempt to avoid local minima. A constant initialisation may have the effect of producing a smoother parameter map, quite artificially.

In this chapter, we have applied MLOFI framework to single direction diffusion MRI models. The MLOFI framework can be extended to more complicated models of multi-direction dMRI data, such as Diffusion Tensor (DT), CHARMED, multi-directional Diffusion Kurtosis models or the recently proposed DIAMOND model (Scherrer et al., 2016). The model derivatives required for OFI calculations are easily computable with respect to the primary model parameters, such as the six distinct ADCs that constitute the diffusion tensor in the DT model or the multiple distribution parameters in DIAMOND's mixture model.

6.6 Summary

The increase in Quantitative MRI techniques is increasing the relevance of intuitive metrics by which to gauge parameter estimation performance. With application to ADC modelling, we have shown that the traditional Cramer Rao lower bound analysis produces misleading predictions of estimator performance. Further, we have introduced the simple concept of MLOFI, with model accuracy encapsulated by the height of the likelihood function, and estimator precision encapsulated by the curvature of the likelihood surface. The Gamma model, which comprises a contiuum of compartment sizes distribued according to a Gamma probability distribution, was shown to be a more robust ADC model that the traditional one and two component exponential models.

Appendices

6.A Hessian of The Log-likelihood Function with Gaussian Distribution

For all models, $M^i(\boldsymbol{b}, \boldsymbol{\theta}^i)$, with the parameter vector, $\boldsymbol{\theta}^i$, the Hessian of the log-likelihood function is defined as,

$$\mathcal{H}(\theta_j) = \sum_{k=1}^{n} \frac{1}{\sigma^2} \left(\frac{\partial^2 M^i(b_k, \boldsymbol{\theta}^i)}{\partial \theta_j^2} (y_k - M^i(b_k, \boldsymbol{\theta}^i)) - \left(\frac{\partial M^i(b_k, \boldsymbol{\theta}^i)}{\partial \theta_j} \right)^2 \right), \quad (6.19)$$

where $\theta_j \in \boldsymbol{\theta}^i$, and $i \in \{\text{ME, BE, DK, GA}\}$. The first and second order derivatives of the diffusion models w.r.t. each parameter are given below.

Model Derivatives:

Exponential Model

$$\frac{\partial}{\partial D} M^{ME}(\mathbf{b}, \boldsymbol{\theta}^{ME}) = -\boldsymbol{b} \exp^{-\boldsymbol{b}D}. \quad (6.20)$$

$$\frac{\partial^2}{\partial D^2} M^{ME}(\mathbf{b}, \boldsymbol{\theta}^{ME}) = \boldsymbol{b}^2 \exp^{-\boldsymbol{b}D}. \quad (6.21)$$

Bi-exponential Model

First order derivatives:

$$\frac{\partial}{\partial D_r} M^{BE}(\boldsymbol{b}, \boldsymbol{\theta}^{BE}) = -f\, \boldsymbol{b} \exp^{-\boldsymbol{b}D_r}, \quad (6.22)$$

$$\frac{\partial}{\partial D_h} M^{BE}(\boldsymbol{b}, \boldsymbol{\theta}^{BE}) = -(1-f)\, \boldsymbol{b} \exp^{-\boldsymbol{b}D_h}, \quad (6.23)$$

$$\frac{\partial}{\partial f} M^{BE}(\boldsymbol{b}, \boldsymbol{\theta}^{BE}) = \exp^{-\boldsymbol{b}D_r} - \exp^{-\boldsymbol{b}D_h}. \quad (6.24)$$

Second order derivatives:

$$\frac{\partial^2}{\partial D_r^2} M^{BE}(\boldsymbol{b}, \boldsymbol{\theta}^{BE}) = f\, \boldsymbol{b}^2 \exp^{-\boldsymbol{b}D_r}, \quad (6.25)$$

$$\frac{\partial^2}{\partial D_h^2} M^{BE}(\boldsymbol{b}, \boldsymbol{\theta}^{BE}) = (1-f)\, \boldsymbol{b}^2 \exp^{-\boldsymbol{b}D_h}, \quad (6.26)$$

$$\frac{\partial^2}{\partial f^2} M^{BE}(\boldsymbol{b}, \boldsymbol{\theta}^{BE}) = 0. \quad (6.27)$$

DKI Model

We know that $M^{DK}(\boldsymbol{b}, \boldsymbol{\theta}^{DK}) = \exp^{-\boldsymbol{b}D + \frac{1}{6}\boldsymbol{b}^2 D^2 K}$, then

$$\frac{\partial}{\partial D} M^{DK}(\boldsymbol{b}, \boldsymbol{\theta}^{DK}) = (-\boldsymbol{b} + \frac{1}{3}\mathbf{b}^2 DK)\ M^{DK}(\boldsymbol{b}, \boldsymbol{\theta}^{DK}), \tag{6.28}$$

$$\frac{\partial}{\partial K} M^{DK}(\boldsymbol{b}, \boldsymbol{\theta}^{DK}) = \frac{1}{6}\boldsymbol{b}^2 D^2\ M^{DK}(\boldsymbol{b}, \boldsymbol{\theta}^{DK}). \tag{6.29}$$

Second order derivatives:

$$\frac{\partial^2}{\partial D^2} M^{DK}(\boldsymbol{b}, \boldsymbol{\theta}^{DK}) = \frac{1}{3}\mathbf{b}^2 K M^{DK}(\boldsymbol{b}, \boldsymbol{\theta}^{DK}) + (-\boldsymbol{b} + \frac{1}{3}\mathbf{b}^2 DK)\ \frac{\partial}{\partial D} M^{DK}(\boldsymbol{b}, \boldsymbol{\theta}^{DK}), \tag{6.30}$$

$$\frac{\partial^2}{\partial K^2} M^{DK}(\boldsymbol{b}, \boldsymbol{\theta}^{DK}) = \frac{1}{6}\boldsymbol{b}^2 D^2\ \frac{\partial}{\partial K} M^{DK}(\boldsymbol{b}, \boldsymbol{\theta}^{DK}). \tag{6.31}$$

Gamma Model

First order derivatives:

$$\frac{\partial}{\partial k} M^{GA}(\boldsymbol{b}, \boldsymbol{\theta}^{GA}) = -(1 + \boldsymbol{b}\theta)^{-k} \ln(1 + \boldsymbol{b}\theta), \tag{6.32}$$

$$\frac{\partial}{\partial \theta} M^{GA}(\boldsymbol{b}, \boldsymbol{\theta}^{GA}) = -\boldsymbol{b}k(1 + \boldsymbol{b}\theta)^{-(k+1)}, \tag{6.33}$$

$$\frac{\partial}{\partial D_{GA}} M^{GA}(\boldsymbol{b}, \boldsymbol{\theta}^{GA}) = 2D_{GA}\nu^{-1} \frac{\partial}{\partial k} M^{GA}(\boldsymbol{b}, \boldsymbol{\theta}^{GA}), \tag{6.34}$$

$$\frac{\partial}{\partial \nu} M^{GA}(\mathbf{b}, \boldsymbol{\theta}^{GA}) = D_{GA}^{-1} \frac{\partial}{\partial \theta} M^{GA}(\boldsymbol{b}, \boldsymbol{\theta}^{GA}). \tag{6.35}$$

Second order derivatives:

$$\frac{\partial^2}{\partial k^2} M^{GA}(\boldsymbol{b}, \boldsymbol{\theta}^{GA}) = -\ln(1 + \boldsymbol{b}\theta)\ \frac{\partial}{\partial k} M^{GA}(\boldsymbol{b}, \boldsymbol{\theta}^{GA}), \tag{6.36}$$

$$\frac{\partial^2}{\partial \theta^2} M^{GA}(\boldsymbol{b}, \boldsymbol{\theta}^{GA}) = -\boldsymbol{b}^2 k(k+1)(1 + \boldsymbol{b}\theta)^{-(k+2)}, \tag{6.37}$$

$$\tag{6.38}$$

$$\frac{\partial^2}{\partial D_{GA}^2} M^{GA}(\boldsymbol{b}, \boldsymbol{\theta}^{GA}) = 4D_{GA}^2 \nu^{-2} \frac{\partial^2}{\partial k^2} M^{GA}(\boldsymbol{b}, \boldsymbol{\theta}^{GA}) + 2\nu^{-1} \frac{\partial}{\partial k} M^{GA}(\boldsymbol{b}, \boldsymbol{\theta}^{GA}), \tag{6.39}$$

$$\frac{\partial^2}{\partial \nu^2} M^{GA}(\mathbf{b}, \boldsymbol{\theta}^{GA}) = D_{GA}^{-2} \frac{\partial^2}{\partial \theta^2} M^{GA}(\boldsymbol{b}, \boldsymbol{\theta}^{GA}). \tag{6.40}$$

6.B Regularity Conditions for CRLB

C1: $\forall\{y : f(y,\theta) > 0\}$ the derivative $\frac{\partial}{\partial\theta} f(y,\theta)$ exists and is finite.
C2: For any unbiased estimator, $\hat{\theta}(y)$ of the unknown parameter θ,

$$\frac{\partial}{\partial\theta}\left[\int \hat{\theta}(y) f(y,\theta) dy\right] = \int \hat{\theta}(y)\left[\frac{\partial}{\partial\theta} f(y,\theta)\right] dy \tag{6.41}$$

CHAPTER
SEVEN

Conclusion

MULTICOMPARTMENT models provide a simplified description of a non-exponential signal decay. Over the years, such models have been applied to characterize transverse relaxation, diffusion, susceptibility effects, myelin water fraction and a number of other biophysical phenomenons. This thesis developed methods to advance and improve multicompartment modelling paradigms while keeping in mind the limitations of such modelling approaches.

7.1 Summary of original contributions

Chapter 3 developed a continuum distribution model of transverse relaxation decay in low intensity sodium MRI images. Compared to the parameter maps of bi-exponential mixture model, the continuum distribution model parameters (i.e. the mean of gamma distributed T_2 compartments and fast fraction) provided structurally detailed parameter maps, with superior tissue contrast. The fast fraction maps allowed to discern between unordered media, such as the CSF, and highly organized tissue structures including WM and GM regions.

Chapter 4 investigated the robustness of various diffusion models, and through experimental evidence, exposed the limitations of CRLB in providing accurate estimates of parameter variance. Further, a two-compartment model for the estimation of axon diameter distribution from diffusion-weighted data was developed and applied to the experimental data from an ovine optic nerve. The resultant analysis revealed the insufficiency of such models in describing the complicated tissue morphology and highlighted the need for more accurate and robust modelling techniques.

Chapter 5 explored the potential of obtaining high SNR images through averaging multiecho MRI data. An simple optimization problem was developed, leading to an analytical expression for identifying optimal number of echoes needed for averaging given a mono-exponential model of T_2^*-weighted signal. In case of bi-exponential and gamma distribution models, the optimization lead to intractable expressions, which were solved by a root-finding algorithm. The equivalence between the optimized SNR gain under the assumptions of Gaussian and Rician noise models was established through simulations and experimental data.

Chapter 6 addressed the limitations of CRLB analyses for assessing estimation performance and presented a data-dependent performance analysis framework called MLOFI. The terms describing precision and accuracy in parameter estimates in the MLOFI framework arise naturally from the Taylor's expansion of the model log-likelihood function. MLOFI of the multicompartment ADC models to an experimental DW-MRI dataset demonstrated superior performance of the gamma model parameters as compared to the mono-exponential, bi-exponential and the diffusion kurtosis models.

7.2 Future Directions

Statistical modelling and inference are powerful mathematical tools for characterizing tissue microstructure from MR signals. Given the wide range of NMR-based imaging modalities, there is always room for improvement and further development. This thesis applied the concept of multicompartment modelling to sodium and diffusion weighted imaging. In sodium imaging, the continuum distribution model provided robust parameter mapping that offered invaluable insights into the organization of sodium spin systems. Conversely, the axon diameter distribution model failed to describe the diffusion weighted signal decay under long gradient pulses, exposing the practical limitations to which a signal model can be utilized to infer information about tissue properties. Hence, this thesis presents opportunities for future investigation of both strengths and limitations of compartment modelling techniques.

Models of Sodium Signal

The gamma distribution model of the sodium signal assumes a unimodal distribution of T_2^* components, and as a result, we observed in chapter 3 that the estimated mean of the gamma distribution was biased more towards the short T_2^* component as it forms 60% of the observed sodium signal. Since each T_2^* compartment is characterised by a bi-exponential decay, the future work could develop a bimodal distribution model to model the signal. The potential of mixture distributions such as a gamma mixture distribution could be explored.

The fast fraction parameter emerging from the gamma distribution model offers the potential to gain insights into the sodium content of structured tissue. This thesis presents preliminary comparison between WM structures delineated by the sodium fast fraction and proton images. In future, there is a need for rigorous validation and studies could be conducted to correlate the fast fraction to tissue complexity. Cues from DW-MRI could provide more clear validation.

Axon Diameter Distribution

Theoretical analysis of the two-compartment axon diameter distribution model under long gradient pulses was shown to provide enhanced differentiation between signals from varying axon sizes. Despite inference being possible, the resulting parameter estimates did not reflect the histological ground truth, with potential cause on both the model and the data side of the equation. Future work can explore the causes of the discrepancy between the theoretical and experimental estimation results. Insufficiency of tractable signal models in describing complicated biophysical diffusion processes, un-modelled effects such as compartmental exchange, uncertain estimation due to ill-posedness of the optimization expression, and imaging artifacts such as ghosting and signal wrapping are the potential contributing factors.

Estimation Performance

This thesis presented an estimation performance framework based on the characteristics of the log-likelihood function at and in the vicinity of the maximum likelihood estimate. This framework has the potential to overcome the limitations of CRLB analyses in determining parameter precision. Future work could focus on extending the MLOFI framework to incorporate it into experiment design and optimization applications.

7.3 Final Remarks

This thesis considered the utility and limitations of multicompartment modelling techniques in providing meaningful insights into the tissue structure. Although additional work is required before the modelling strategies presented herein can be adapted to clinical applications, it is hoped that the work presented will provide a direction for improving the efficacy of statistical modelling techniques in MRI.

Bibliography

Abragam, A. *The principles of nuclear magnetism*. Oxford University Press, 1961.

Abramowitz, M and Stegun, I. A. *Handbook of mathematical functions: with formulas, graphs, and mathematical tables*, volume 55. Courier Corporation, 1964.

Acosta-Cabronero, J, Williams, G. B, Cardenas-Blanco, A, Arnold, R. J, Lupson, V, and Nestor, P. J. In vivo quantitative susceptibility mapping (QSM) in Alzheimer's disease. *PloS one*, 8(11):e81093, 2013.

Akaike, H. A new look at the statistical model identification. *IEEE Transactions on Automatic Control*, 19(6):716–723, 1974.

Alexander, D. A general framework for experiment design in diffusion MRI and its application in measuring direct tissue-microstructure features. *Magn Reson Med*, 60:439–448, 2008.

Alexander, D, Hubbard, P, Hall, M, Moore, E, Ptito, M, Parker, G, and Dyrby, T. Orientationally invariant indices of axon diameter and density from diffusion MRI. *NeuroImage*, 52:1374–1389, 2010.

Andersson, J. L and Sotiropoulos, S. N. Non-parametric representation and prediction of single-and multi-shell diffusion-weighted MRI data using Gaussian processes. *NeuroImage*, 122:166–176, 2015.

Assaf, Y and Basser, P. J. Composite hindered and restricted model of diffusion (CHARMED) MR imaging of the human brain. *NeuroImage*, 27(1):48–58, 2005.

Assaf, Y, Mayk, A, and Cohen, Y. Displacement imaging of spinal cord using q-space diffusion-weighted MRI. *Magn Reson Med*, 44(5):713–722, 2000.

Assaf, Y, Freidlin, R, Rohde, G, and Basser, P. New modeling and experimental framework to characterize hindered and restricted water diffusion in brain white matter. *Magn Reson Med*, 52(5):965–978, 2004.

Assaf, Y, Blumenfeld-Katzir, T, Yovel, Y, and Basser, P. J. AxCaliber: a method for measuring axon diameter distribution from diffusion MRI. *Magn Reson Med*, 59(6):1347–1354, 2008.

Barazany, D, Basser, P. J, and Assaf, Y. In vivo measurement of axon diameter distribution in the corpus callosum of rat brain. *Brain*, 132(5):1210–1220, 2009.

Basharat, M, Payne, G, Morgan, V, Parker, C, Dearnaley, D, and DeSouza, N. TE = 32 ms vs TE = 100 ms echo-time ^{1}H-magnetic resonance spectroscopy in prostate cancer: Tumor metabolite depiction and absolute concentrations in tumors and adjacent tissues. *Journal of Magnetic Resonance Imaging*, 42(4): 1086–1093, 2015.

Basser, P. J, Mattiello, J, and LeBihan, D. Estimation of the effective self-diffusion tensor from the NMR spin echo. *Journal of Magnetic Resonance, Series B*, 103 (3):247–254, 1994a.

Basser, P. J, Mattiello, J, and LeBihan, D. MR diffusion tensor spectroscopy and imaging. *Biophysical Journal*, 66(1):259–267, 1994b.

Beaulieu, C. The basis of anisotropic water diffusion in the nervous system - a technical review. *NMR in Biomed*, 15(7-8):435–455, 2002.

Beck, J. V and Woodbury, K. A. Inverse problems and parameter estimation: integration of measurements and analysis. *Measurement Science and Technology*, 9(6):839, 1998.

Behrens, T, Berg, H, Johansen, H, Jbabdi, S, Rushworth, M, and Woolrich, M. Probabilistic diffusion tractography with multiple fibre orientations: What can we gain? *NeuroImage*, 34(1):144–155, 2007.

Behrens, T. E, Woolrich, M. W, Jenkinson, M, Johansen-Berg, H, Nunes, R. G, Clare, S, Matthews, P. M, Brady, J. M, and Smith, S. M. Characterization and propagation of uncertainty in diffusion-weighted MR imaging. *Magn Reson Med*, 50(5):1077–1088, 2003.

Beltrachini, L, von Ellenrieder, N, and Muravchik, C. Error bounds in diffusion tensor estimation using multiple-coil acquisition systems. *Magnetic Resonance Imaging*, 31(8):1372–1383, 2013.

Berendsen, H and Edzes, H. The observation and general interpretation of sodium magnetic resonance in biological material. *Annals of the New York Academy of Sciences*, 204(1):459–485, 1973.

Bhavsar, S, Zvyagintsev, M, and Mathiak, K. BOLD sensitivity and SNR characteristics of parallel imaging-accelerated single-shot multi-echo EPI for fMRI. *NeuroImage*, 84:65–75, 2014.

Bihan, D, Breton, E, Lallemand, D, Grenier, P, Cabanis, E, and Laval-Jeantet, M. MR imaging of intravoxel incoherent motions: application to diffusion and perfusion in neurologic disorders. *Radiology*, 161:401–407, 1986.

Biver, P, Clerico, A, Paci, A, Balzan, S, Boldrini, A, and Cipolloni, C. Endogenous digitalis-like factors: their possible pathophysiological implications with particular regard to the perinatal period. *Child Nephrology and Urology*, 10(3): 164–180, 1990.

Bloch, F. Nuclear induction. *Physical review*, 70(7-8):460, 1946.

Blunck, Y, Josan, S, Taqdees, S. W, Moffat, B. A, Ordidge, R. J, Cleary, J. O, and Johnston, L. A. 3D-multi-echo radial imaging of ^{23}Na (3D-MERINA) for time-efficient multi-parameter tissue compartment mapping. *Magn Reson Med*, 79(4):1950–1961, 2018.

Bouhrara, M, Reiter, D, Celik, H, Bonny, J, Lukas, V, Fishbein, K, and Spencer, R. Incorporation of Rician noise in the analysis of biexponential transverse relaxation in cartilage using a multiple gradient echo sequence at 3 and 7 Tesla. *Magn Reson Med*, 73(1):352–366, 2015.

Braunstein, S. How large a sample is needed for the maximum likelihood estimator to be approximately gaussian? *Journal of Physics A: Mathematical and General*, 25(13):3813, 1992.

Brihuega-Moreno, O, Heese, F. P, and Hall, L. D. Optimization of diffusion measurements using Cramer-Rao lower bound theory and it sapplication to articular cartilage. *Magn Reson Med*, 50(5):1069–76, 2003.

Bull, T. Nuclear magnetic relaxation of spin-3/2 nuclei involved in chemical exchange. *Journal of Magnetic Resonance (1969)*, 8(4):344–353, 1972.

Callaghan, P. T. *Principles of Nuclear Magnetic Resonance Microscopy*. Oxford Science Publications. Clarendon Press, 1993.

Caravan, P. Strategies for increasing the sensitivity of gadolinium based MRI contrast agents. *Chemical Society Reviews*, 35(6):512–523, 2006.

Caravan, P, Ellison, J. J, McMurry, T. J, and Lauffer, R. B. Gadolinium (III) chelates as MRI contrast agents: structure, dynamics, and applications. *Chemical reviews*, 99(9):2293–2352, 1999.

Cauter, S. V, Veraart, J, and Sijbers, J. Gliomas: diffusion kurtosis MR imaging in grading. *Radiology*, 263:492–501, 2012.

Ceccarelli, A, Bakshi, R, and Neema, M. MRI in multiple sclerosis: a review of the current literature. *Current Ppinion in Neurology*, 25(4):402–409, 2012.

Celik, H, Bouhrara, M, Reiter, D. A, Fishbein, K. W, and Spencer, R. G. Stabilization of the inverse Laplace transform of multiexponential decay through introduction of a second dimension. *Journal of Magnetic Resonance*, 236:134–139, 2013.

Chang, G, Wang, L, Schweitzer, M. E, and Regatte, R. R. 3D ^{23}Na MRI of human skeletal muscle at 7 Tesla: initial experience. *European Radiology*, 20 (8):2039–2046, 2010.

Chen, W, Zhu, W, Kovanlikaya, I, Kovanlikaya, A, Liu, T, Wang, S, Salustri, C, and Wang, Y. Intracranial calcifications and hemorrhages: characterization with quantitative susceptibility mapping. *Radiology*, 270(2):496–505, 2014.

Chiew, M and Graham, S. J. Bold contrast and noise characteristics of densely sampled multi-echo fMRI data. *IEEE transactions on medical imaging*, 30(9): 1691–1703, 2011.

Christo, P and El-Mallakh, R. Possible role of endogenous Ouabain-like compounds in the pathophysiology of bipolar illness. *Medical Hypotheses*, 41(4): 378–383, 1993.

Clark, C and Bihan, D. L. Water diffusion compartmentation and anisotropy at high b values in the human brain. *Magn Reson Med*, 44(6):852–859, 2000.

Clerico, A and Giampietro, O. Is the endogenous digitalis-like factor the link between hypertension and metabolic disorders as diabetes mellitus, obesity and acromegaly? *Clinical Physiology and Biochemistry*, 8(3):153–168, 1990.

Codd, S. L and Callaghan, P. T. Spin echo analysis of restricted diffusion under generalized gradient waveforms: planar, cylindrical, and spherical pores with wall relaxivity. *Journal of Magnetic Resonance*, 137(2):358–372, 1999.

Cohen, A. D, Nencka, A. S, and Wang, Y. Multiband multi-echo simultaneous ASL/BOLD for task-induced functional MRI. *PloS one*, 13(2):e0190427, 2018.

Cohen-Adad, J and Wheeler-Kingshott, C. Quantitative MRI of the spinal cord. page 109. Academic Press, 2014.

Cole, W. C, Leblanc, A. D, and Jhingran, S. G. The origin of biexponential T^2 relaxation in muscle water. *Magn Reson Med*, 29(1):19–24, 1993.

Crank, J. *The mathematics of diffusion.* Oxford University Press, 1975.

Damadian, R. Tumor detection by nuclear magnetic resonance. *Science*, 171 (3976):1151–1153, 1971.

Davoodi-Bojd, E, Chopp, M, Soltanian-Zadeh, H, Wang, S, Ding, G, and Jiang, Q. An Analytical Model for Estimating Water Exchange Rate in White Matter Using Diffusion MRI. *PLoS ONE*, 9(5), 2014.

Dean, R. Theories of electrolyte equilibrium in muscle. In *Biol. Symp*, volume 3, pages 331–348, 1941.

Dekker, T. Finding a zero by means of successive linear interpolation. In Dejon, B and Henrici, P, editors, *Constructive aspects of the fundamental theorem of algebra*, pages 37–51. Wiley-Interscience, 1969.

Denk, C and Rauscher, A. Susceptibility weighted imaging with multiple echoes. *Journal of Magnetic Resonance Imaging*, 31(1):185–191, 2010.

Duerk, J. L, Lewin, J. S, Wendt, M, and Petersilge, C. Remember true FISP? a high SNR, near 1-second imaging method for T_2-like contrast in interventional MRI at. 2 T. *Journal of Magnetic Resonance Imaging*, 8(1):203–208, 1998.

Dula, A, Gochberg, D, and Does, M. Optimal echo spacing for multi-echo imaging measurements of Bi-exponential T_2 relaxation. *Journal of Magnetic Resonance*, 196(2):149–156, 2009.

Efron, B and Hinkley, D. Assessing the accuracy of the maximum likelihood estimator: Observed versus expected fisher information. *Biometrika*, 65(3): 457–482, 1978.

El-Mallakh, R, Barrett, J, and Jed-Wyatt, R. The Na, K-ATPase hypothesis for bipolar disorder: Implications of normal development. *Journal of Child and Adolescent Psychopharmacology*, 3(1):37–52, 1993.

Eldar, Y. Rethinking biased estimation: Improving maximum likelihood and the Cramer-Rao bound. *Foundations and Trends in Signal Processing*, 1(4):305–449, 2008.

Eliav, U and Navon, G. Analysis of double-quantum-filtered NMR spectra of ^{23}Na in biological tissues. *Journal of Magnetic Resonance, Series B*, 103(1):19–29, 1994.

Farid, A, Fatima, O, Karim, A, and Harba, R. On the optimal reconstruction of dMRI images with multi-coil acquisition system. In *European Signal Processing Conference*, volume 2016-Novem, pages 1318–1322, 2016.

Fass, L. Imaging and cancer: a review. *Molecular Oncology*, 2(2):115–152, 2008.

Fiege, D. P, Romanzetti, S, Mirkes, C. C, Brenner, D, and Shah, N. J. Simultaneous single-quantum and triple-quantum-filtered MRI of ^{23}Na (SISTINA). *Magn Reson Med*, 69(6):1691–1696, 2013.

Fong, W. Handbook of MRI pulse sequences. *Medical Physics*, 32(5):1452–1452, 2005.

Freed, J. H. Generalized cumulant expansions and spin-relaxation theory. *The Journal of Chemical Physics*, 49(1):376–391, 1968.

Frisoni, G. B, Fox, N. C, Jack Jr, C. R, Scheltens, P, and Thompson, P. M. The clinical use of structural MRI in Alzheimer disease. *Nature Reviews Neurology*, 6(2):67, 2010.

Gerig, G, Kubler, O, Kikinis, R, and Jolesz, F. A. Nonlinear anisotropic filtering of MRI data. *IEEE Transactions on medical imaging*, 11(2):221–232, 1992.

Goldberg, M and Gilboa, H. Sodium magnetic resonance in biological systems. interpretation of the relaxation curves. In *Nuclear magnetic resonance spectroscopy in molecular biology*, pages 481–491. Springer, 1978.

Gowland, P and Bowtell, R. Theoretical optimization of multi-echo fMRI data acquisition. *Physics in Medicine and Biology*, 52(7):1801, 2007.

Granziera, C, Schmahmann, J. D, Hadjikhani, N, Meyer, H, Meuli, R, Wedeen, V, and Krueger, G. Diffusion spectrum imaging shows the structural basis of functional cerebellar circuits in the human cerebellum in vivo. *PLoS One*, 4(4): e5101, 2009.

Gras, V, Farrher, E, Grinberg, F, and Shah, N. Diffusion-weighted DESS protocol optimization for simultaneous mapping of the mean diffusivity, proton density and relaxation times at 3 Tesla. *Magn Reson Med*, 78(1):130–141, 2016.

Graves, S, Brown, B, and Valdes, R. An endogenous digoxin-like substance in patients with renal impairment. *Annals of Internal Medicine*, 99(5):604–608, 1983.

Grebenkov, D. S. NMR survey of reflected Brownian motion. *Reviews of Modern Physics*, 79(3):1077, 2007.

Greicius, M. D, Srivastava, G, Reiss, A. L, and Menon, V. Default-mode network activity distinguishes Alzheimer's disease from healthy aging: evidence from functional MRI. *Proceedings of the National Academy of Sciences of the United States of America*, 101(13):4637–4642, 2004.

Grinberg, F, Farrher, E, Ciobanu, L, Geffroy, F, Bihan, D. L, and Shah, J. Non-gaussian diffusion imaging for enhanced contrast of brain tissue affected by ischemic stroke. *Plos One*, 9(2):1–15, 02 2014.

Grodd, W and Klose, U. Sodium-MR-imaging of the brain: initial clinical results. *Neuroradiology*, 30(5):399–407, 1988.

Guyader, J, Bernardin, L, Douglas, N, Poot, D, Niessen, W, and Klein, S. Influence of image registration on apparent diffusion coefficient images computed from free-breathing diffusion MR images of the abdomen. *Journal of Magnetic Resonance Imaging*, 42(2):315–330, 2015.

Hancu, I, Boada, F. E, and Shen, G. X. Three-dimensional triple-quantum–filtered ^{23}Na imaging of in vivo human brain. *Magn Reson Med*, 42(6):1146–1154, 1999.

Harms, R, Fritz, F, Tobisch, A, Goebel, R, and Roebroeck, A. Robust and fast nonlinear optimization of diffusion MRI microstructure models. *NeuroImage*, 155:82–96, 2017.

Hashimoto, T, Ikehira, H, Fukuda, H, Yamaura, A, Watanabe, O, Tateno, Y, Tanaka, R, and Simon, H. In vivo sodium-23 MRI in brain tumors: evaluation of preliminary clinical experience. *American Journal of Physiologic Imaging*, 6 (2):74–80, 1991.

Heads, T, Pollock, M, Robertson, A, Sutherland, W, and Allpress, S. Sensory nerve pathology in amyotrophic lateral sclerosis. *Acta Neuropathol*, 82:316–320., 1991.

Helms, G and Dechent, P. Increased SNR and reduced distortions by averaging multiple gradient echo signals in 3D FLASH imaging of the human brain at 3T. *Journal of Magnetic Resonance Imaging*, 29(1):198–204, 2009.

Helpern, J, Falangola, M, and Martino, A. D. Alterations in brain microstructure in ADHD by diffusional kurtosis imaging. *Proc 15th Ann Mtg ISMRM Berlin, Germany*, 2007.

Hernando, D, Haldar, J, Sutton, B, Ma, J, Kellman, P, and Liang, Z. Joint estimation of water/fat images and field inhomogeneity map. *Magn Reson Med*, 59(3):571–580, 2008.

Hernando, D, Kellman, P, Haldar, J, and Liang, Z. Robust water/fat separation in the presence of large field inhomogeneities using a graph cut algorithm. *Magn Reson Med*, 63(1):79–90, 2010.

Herrling, M, Weisbrodt, J, Kirkland, C, Williamson, N, Lackner, S, Codd, S, Seymour, J, Guthausen, G, and Horn, H. NMR investigation of water diffusion in different biofilm structures. *Biotechnology and Bioengineering*, 114(12):2857–2867, 2017.

Hilal, S. K, Maudsley, A. A, Ra, J, Simon, H. E, Roschmann, P, Wittekoek, S, Cho, Z, and Mun, S. In vivo NMR imaging of sodium-23 in the human head. *Journal of Computer Assisted Tomography*, 9(1):1–7, 1985.

Horisberger, J. Recent insights into the structure and mechanism of the sodium pump. *Physiology*, 19(6):377–387, 2004.

Horsefield, M and Jones, D. Applications of diffusion-weighted and diffusion tensor MRI to white matter disease a review. *NMR in Biomedicine*, 15(7-8):570–577, 2002.

Hubbard, P. Nonexponential nuclear magnetic relaxation by quadrupole interactions. *The Journal of Chemical Physics*, 53(3):985–987, 1970.

Hui, E, Fieremans, E, Jensen, J, Tabesh, A, Feng, W, Bonilha, L, Spampinato, M, Adams, R, and Helpern, J. Stroke assessment with diffusional kurtosis imaging. *Stroke*, 43(11):2968–2973, 2012.

Hursh, J. The properties of growing nerve fibers. *American Journal of Physiology-Legacy Content*, 127(1):140–153, 1939.

Inglese, M, Madelin, G, Oesingmann, N, Babb, J, Wu, W, Stoeckel, B, Herbert, J, and Johnson, G. Brain tissue sodium concentration in multiple sclerosis: a sodium imaging study at 3 Tesla. *Brain*, 133(3):847–857, 2010.

Isom, L. The role of sodium channels in cell adhesion. *Frontiers in Bioscience 7*, 53(3):12–23, 2002.

Jack, C. R, Bernstein, M. A, Fox, N. C, Thompson, P, Alexander, G, Harvey, D, Borowski, B, Britson, P. J, L Whitwell, J, Ward, C, et al. The Alzheimer's disease neuroimaging initiative (ADNI): MRI methods. *Journal of Magnetic Resonance Imaging*, 27(4):685–691, 2008.

Jenkinson, M, Beckmann, C. F, Behrens, T. E, Woolrich, M. W, and Smith, S. M. FSL. *Neuroimage*, 62(2):782–790, 2012.

Jensen, J. H, Helpern, J. A, Ramani, A, Lu, H, and Kaczynski, K. Diffusional kurtosis imaging: The quantification of non-gaussian water diffusion by means of magnetic resonance imaging. *Magn Reson Med*, 53:1432–1440, 2005.

Jerecic, R, Bock, M, Wacker, C, Bauer, W, and Schad, L. ^{23}Na-MRI of the human heart using a 3D radial projection technique. *Biomedizinische Technik/Biomedical Engineering*, 47(s1a):458–459, 2002.

Johnston, L, Wright, D, Philipsen, R. H, Kolbe, S, Bourne, J, Mareels, I, and Egan, G. Inferring micron-scale tissue structure using extreme value theory for cylindrically restricted diffusion. *Proc. Intl. Soc. Mag. Reson. Med.*, 19, 2011.

Jones, D. *Diffusion MRI: Theory, Methods, and Applications*. Oxford University Press, 2010.

Jones, J, Hodgkinson, P, Barker, A, and Hore, P. Optimal sampling strategies for the measurement of spin-spin relaxation times. *Journal of Magnetic Resonance, Series B*, 113(1):25–34, 1996.

Kaden, E, Kelm, N. D, Carson, R. P, Does, M. D, and Alexander, D. C. Multi-compartment microscopic diffusion imaging. *NeuroImage*, 139:346–359, 2016.

Kärger, J. NMR self-diffusion studies in heterogeneous systems. *Adv. Colloid. Interface. Sci.*, 23:129–148, 1985.

Kärger, J, Pfeifer, H, and Heink, W. Principles and applications of self-diffusion measurements by nuclear magnetic resonance. *Advances in Magnetic Resonance*, 12:1–89, 1988.

Komlosh, M. E, Özarslan, E, Lizak, M, Horkayne-Szakaly, I, Freidlin, R. Z, Horkay, F, and Basser, P. J. Mapping average axon diameters in porcine spinal cord white matter and rat corpus callosum using d-PFG MRI. *NeuroImage*, 78: 210–216, 2013.

Kundu, P, Inati, S, Evans, J, Luh, W, and Bandettini, P. Differentiating BOLD and non-BOLD signals in fMRI time series using multi-echo EPI. *NeuroImage*, 60(3):1759–1770, 2012.

Kurugol, S, Freiman, M, Afacan, O, Domachevsky, L, Perez-rossello, J, Callahan, M, and Warfield, S. Motion-robust parameter estimation in abdominal diffusion-weighted MRI by simultaneous image registration and model estimation R. *Medical Image Analysis*, 39:124–132, 2017.

Laule, C and MacKay, A. Chapter 3.5 - T_2 Relaxation . In Cohen-Adad, J and Wheeler-Kingshott, C. A, editors, *Quantitative MRI of the Spinal Cord* , pages 181 – 206. Academic Press, 2014.

Lauterbur, P et al. Image formation by induced local interactions: examples employing nuclear magnetic resonance. 1973.

Layton, K, Morelande, M, Wright, D, Farrell, P, Moran, B, and Johnston, L. Modelling and estimation of multicomponent T_2 distributions. *IEEE Transactions on Medical Imaging*, 32(8):1423–1434, 2013.

Le Bihan, D, Breton, E, Lallemand, D, Grenier, P, Cabanis, E, and Laval-Jeantet, M. MR imaging of intravoxel incoherent motions: application to diffusion and perfusion in neurologic disorders. *Radiology*, 161(2):401–407, 1986.

Lee, D. C, Markl, M, DallArmellina, E, Han, Y, Kozerke, S, Kuehne, T, Nielles-Vallespin, S, Messroghli, D, Patel, A, Schaeffter, T, et al. The growth and evolution of cardiovascular magnetic resonance: a 20-year history of the Society for Cardiovascular Magnetic Resonance (SCMR) annual scientific sessions. *Journal of Cardiovascular Magnetic Resonance*, 20(1):8, 2018.

Lein, E et al. Genome-wide atlas of gene expression in the adult mouse brain. *Nature*, 445:168–176, 2007.

Leporq, B, Saint-Jalmes, H, Rabrait, C, Pilleul, F, Guillaud, O, Dumortier, J, Scoazec, J, and Beuf, O. Optimization of intra-voxel incoherent motion imaging at 3.0 Tesla for fast liver examination. *Journal of Magnetic Resonance Imaging*, 41(5):1209–1217, 2015.

Levesque, I. R and Pike, G. B. Characterizing healthy and diseased white matter using quantitative magnetization transfer and multicomponent T_2 relaxometry: A unified view via a four-pool model. *Magn Reson Med*, 62(6):1487–1496, 2009.

Levitt, M. H. Spin dynamics: basics of nuclear magnetic resonance. *Jon Wiley and Sons*, 196, 2001.

Li, X, Van Gelderen, P, Sati, P, De Zwart, J. A, Reich, D. S, and Duyn, J. H. Detection of demyelination in multiple sclerosis by analysis of T_2^* relaxation at 7T. *NeuroImage: Clinical*, 7:709–714, 2015.

Liang, Z.-P and Lauterbur, P. C. *Principles of magnetic resonance imaging: a signal processing perspective*. SPIE Optical Engineering Press, 2000.

Ljunggren, S. A simple graphical representation of fourier-based imaging methods. *Journal of Magnetic Resonance (1969)*, 54(2):338–343, 1983.

Lu, H, Jensen, J, Hu, C, Falangola, M, Ramani, A, Ferris, S, and Helpern, J. Alterations in cerebral microstructual integrity in normal aging and in Alzheimer's disease: a multi-contrast diffusion MRI study. *Proc 14th Ann Mtg ISMRM Seattle, WA, USA*, 2006.

MacKay, A, Laule, C, Vavasour, I, Bjarnason, T, Kolind, S, and Mädler, B. Insights into brain microstructure from the T_2 distribution. *Magnetic Resonance Imaging*, 24(4):515–525, 2006.

MacKay, D. Bayesian nonlinear modeling for the prediction competition. *ASHRAE transactions*, 100(2):1053–1062, 1994.

Madelin, G and Regatte, R. Biomedical applications of sodium MRI in vivo. *Journal of Magnetic Resonance Imaging*, 38(3):511–529, 2013.

Madelin, G, Lee, J, Regatte, R. R, and Jerschow, A. Sodium MRI: Methods and applications. *Progress in Nuclear Magnetic Resonance Spectroscopy*, 79 (Supplement C):14 – 47, 2014.

Majumdar, S, Orphanoudakis, S, Gmitro, A, O'donnell, M, and Gore, J. Errors in the measurements of T_2 using multiple-echo MRI techniques. I. Effects of radiofrequency pulse imperfections. *Magn Reson Med*, 3(3):397–417, 1986a.

Majumdar, S, Orphanoudakis, S, Gmitro, A, O'donnell, M, and Gore, J. Errors in the measurements of T_2 using multiple-echo MRI techniques. II. Effects of static field inhomogeneity. *Magn Reson Med*, 3(4):562–574, 1986b.

Majumdar, S, Zhu, D, Udpa, S, and Raguin, L. A diffusion gradient optimization framework for spinal cord diffusion tensor imaging. *Magnetic Resonance Imaging*, 29(6):789–804, 2011.

Manjón, J. V, Carbonell-Caballero, J, Lull, J. J, García-Martí, G, Martí-Bonmatí, L, and Robles, M. MRI denoising using non-local means. *Medical Image Analysis*, 12(4):514–523, 2008.

Mansfield, P, Maudsley, A, and Bains, T. Fast scan proton density imaging by NMR. *Journal of Physics E: Scientific Instruments*, 9(4):271, 1976.

Maril, N, Rosen, Y, Reynolds, G. H, Ivanishev, A, Ngo, L, and Lenkinski, R. E. Sodium MRI of the human kidney at 3 Tesla. *Magn Reson Med*, 56(6):1229–1234, 2006.

Martin, N, Malfair, D, Zhao, Y, Li, D, Traboulsee, A, Lang, D, and Vertinsky, A. T. Comparison of MERGE and axial T_2-weighted fast spin-echo sequences for detection of multiple sclerosis lesions in the cervical spinal cord. *American Journal of Roentgenology*, 199(1):157–162, 2012.

Mellon, E, Pilkinton, D, Clark, C, Elliott, M, Witschey, W, Borthakur, A, and Reddy, R. Sodium MR imaging detection of mild Alzheimer disease: preliminary study. *American Journal of Neuroradiology*, 30(5):978–984, 2009.

Mesri, H, Layton, K, Mareels, I, and Johnston, L. Performance bounds for diffusion MRI models of tissue microstructure. In *International Society for Magnetic Resonance in Medicine (ISMRM)*, 2014.

Mosher, T. J and Dardzinski, B. J. Cartilage MRI T_2 relaxation time mapping: overview and applications. In *Seminars in Musculoskeletal Radiology*, volume 8, pages 355–368, 2004.

Mulkern, R, Bleier, A, Adzamli, I, Spencer, R, Sandor, T, and Jolesz, F. Two-site exchange revisited: a new method for extracting exchange parameters in biological systems. *Biophysical Journal*, 55(2):221–232, 1989.

Na, H. B, Song, I. C, and Hyeon, T. Inorganic nanoparticles for MRI contrast agents. *Advanced Materials*, 21(21):2133–2148, 2009.

Nagel, A. M, Bock, M, Hartmann, C, Gerigk, L, Neumann, J.-O, Weber, M.-A, Bendszus, M, Radbruch, A, Wick, W, Schlemmer, H.-P, et al. The potential of relaxation-weighted sodium magnetic resonance imaging as demonstrated on brain tumors. *Investigative Radiology*, 46(9):539–547, 2011.

Nam, Y, Lee, J, Hwang, D, and Kim, D.-H. Improved estimation of myelin water fraction using complex model fitting. *NeuroImage*, 116:214–221, 2015.

Nana, R, Zhao, T, and Hu, X. Single-shot multiecho parallel echo-planar imaging (EPI) for diffusion tensor imaging (DTI) with improved signal-to-noise ratio (SNR) and reduced distortion. *Magn Reson Med*, 60(6):1512–1517, 2008.

Neuman, C. Spin echo of spins diffusing in a bounded medium. *The Journal of Chemical Physics*, 60(11):4508–4511, 1974.

Niendorf, T, Dijkhuizen, R, Norris, D, van Lookeren Campagne, M, and Nicolay, K. Biexponential diffusion attenuation in various states of braintissue: implications for diffusion-weighted imaging. *Magn Reson Med*, 36(6):847–857, 1996.

Olver, F, Lozier, D, Boisvert, R, and Clark, C. Lambert W function. *NIST Handbook of Mathematical Functions, Cambridge University Press*, 2010.

Oshio, K, Shinmoto, H, and Mulkern, R. Interpretation of diffusion MR imaging data using a gamma distribution model. *Magn Reson Med Sci*, 13(3):191–195, 2014.

Ouwerkerk, R, Bleich, K. B, Gillen, J. S, Pomper, M. G, and Bottomley, P. A. Tissue sodium concentration in human brain tumors as measured with ^{23}Na MR imaging. *Radiology*, 227(2):529–537, 2003.

Ouwerkerk, R, Weiss, R. G, and Bottomley, P. A. Measuring human cardiac tissue sodium concentrations using surface coils, adiabatic excitation, and twisted projection imaging with minimal T_2 losses. *Journal of Magnetic Resonance Imaging*, 21(5):546–555, 2005.

Ouwerkerk, R, Jacobs, M. A, Macura, K. J, Wolff, A. C, Stearns, V, Mezban, S. D, Khouri, N. F, Bluemke, D. A, and Bottomley, P. A. Elevated tissue sodium concentration in malignant breast lesions detected with non-invasive ^{23}Na MRI. *Breast cancer research and treatment*, 106(2):151–160, 2007.

Ouwerkerk, R, Bottomley, P. A, Solaiyappan, M, Spooner, A. E, Tomaselli, G. F, Wu, K. C, and Weiss, R. G. Tissue Sodium Concentration in Myocardial Infarction in Humans: A Quantitative ^{23}Na MR Imaging Study1. *Radiology*, 248 (1):88–96, 2008.

Parish, T. B, Fieno, D. S, Fitzgerald, S. W, and Judd, R. M. Theoretical basis for sodium and potassium MRI of the human heart at 1.5 T. *Magn Reson Med*, 38(4):653–661, 1997.

Pisharady, P, Sotiropoulos, S, Sapiro, G, and Lenglet, C. A sparse bayesian learning algorithm for white matter parameter estimation from compressed multi-shell diffusion MRI. *Med Image Comput Comput Assist Interv*, 2017.

Piven, J, Bailey, J, Ranson, B, and Arndt, S. An MRI study of the corpus callosum in autism. *Am J Psychiat.*, 154:1051–1056., 1997.

Pizurica, A, Wink, A. M, Vansteenkiste, E, Philips, W, and Roerdink, B. J. A review of wavelet denoising in MRI and ultrasound brain imaging. *Current Medical Imaging Reviews*, 2(2):247–260, 2006.

Poot, D and Klein, S. Detecting statistically significant differences in quantitative MRI experiments, applied to diffusion tensor imaging. *IEEE Transactions on Medical Imaging*, 34(5), 2015.

Poser, B, Versluis, M, Hoogduin, J, and Norris, D. BOLD contrast sensitivity enhancement and artifact reduction with multiecho EPI: parallel-acquired inhomogeneity-desensitized fMRI. *Magn Reson Med*, 55(6):1227–1235, 2006.

Posse, S, Wiese, S, Gembris, D, Mathiak, K, Kessler, C, Grosse-Ruyken, M, Elghahwagi, B, Richards, T, Dager, S, and Kiselev, V. Enhancement of BOLD-contrast sensitivity by single-shot multi-echo functional MR imaging. *Magn Reson Med*, 42(1):87–97, 1999.

Puckett, A, Bollmann, S, Poser, B, Palmer, J, Barth, M, and Cunnington, R. Using multi-echo simultaneous multi-slice (SMS) EPI to improve functional MRI of the subcortical nuclei of the basal ganglia at ultra-high field (7T). *NeuroImage*, 2017.

Raab, P, Hattingen, E, Franz, K, Zanella, F, and Lanfermann, H. Cerebral gliomas: diffusional kurtosis imaging analysis of microstructural differences. *Radiology*, 254:876–881, 2010.

Raffelt, D, Tournier, J, Rose, S, Ridgway, G. R, Henderson, R, Crozier, S, Salvado, O, and Connelly, A. Apparent fibre density: A novel measure for the analysis

of diffusion-weighted magnetic resonance images. *NeuroImage*, 59:3976–3994, 2012.

Ramani, A, Jensen, J, and Szulc, K. Assessment of abnormalities in the cerebral microstructure of schizophrenia patients: a diffusional kurtosis imaging study. *Proc 15th Ann Mtg ISMRM Berlin, Germany*, 2007.

Redpath, T. W. Signal-to-noise ratio in MRI. *The British Journal of Radiology*, 71(847):704–707, 1998.

Reetz, K, Romanzetti, S, Dogan, I, Saß, C, Werner, C. J, Schiefer, J, Schulz, J. B, and Shah, N. J. Increased brain tissue sodium concentration in Huntington's Diseasea sodium imaging study at 4 T. *NeuroImage*, 63(1):517–524, 2012.

Ritchie, J. On the relation between fibre diameter and conduction velocity in myelinated nerve fibres. *Proceedings of the Royal Society of London. Series B, Biological Sciences*, 217:29–35, 1982.

Robertson, B. Spin-echo decay of spins diffusing in a bounded region. *Physical Review*, 151(1):273, 1966.

Rose, A and Valdes, R. Understanding the sodium pump and its relevance to disease. *Clinical Chemistry*, 40(9):1674–1685, 1994.

Rosen, Y and Lenkinski, R. E. Sodium MRI of a human transplanted kidney. *Academic Radiology*, 16(7):886–889, 2009.

Rovira, À, Wattjes, M. P, Tintoré, M, Tur, C, Yousry, T. A, Sormani, M. P, De Stefano, N, Filippi, M, Auger, C, Rocca, M. A, et al. Evidence-based guidelines: MAGNIMS consensus guidelines on the use of MRI in multiple sclerosisclinical implementation in the diagnostic process. *Nature Reviews Neurology*, 11(8):471, 2015.

Rüegg, U. Ouabaina link in the genesis of high blood pressure. *Experientia*, 48 (11-12):1102–1106, 1992.

Salinas, P. Retrograde signalling at the synapse: a role for Wnt proteins. *Biochem Soc Trans*, 33:1295–1298, 2005.

Sati, P, van Gelderen, P, Silva, A. C, Reich, D. S, Merkle, H, De Zwart, J. A, and Duyn, J. H. Micro-compartment specific T_2 relaxation in the brain. *NeuroImage*, 77:268–278, 2013.

Scherrer, B, Taquet, M, and Warfield, S. Reliable selection of the number of fascicles in diffusion images by estimation of the generalization error. *Inf Process Med Imaging*, 23:742–753, 2013.

Scherrer, B, Schwartzman, A, Taquet, M, Sahin, M, Prabhu, S, and Warfield, S. Characterizing brain tissue by assessment of the distribution of anisotropic microstructural environments in diffusion-compartment imaging (DIAMOND). *Magn Reson Med*, 977:963–977, 2016.

Schmid, F, Höltke, C, Parker, D, and Faber, C. Boosting ^{19}F MRI SNR efficient detection of paramagnetic contrast agents using ultrafast sequences. *Magn Reson Med*, 69(4):1056–1062, 2013.

Schmid, M. R, Pfirrmann, C. W, Koch, P, Zanetti, M, Kuehn, B, and Hodler, J. Imaging of patellar cartilage with a 2d multiple-echo data image combination sequence. *American Journal of Roentgenology*, 184(6):1744–1748, 2005.

Schmidt, T, Allen, P, Colucci, W, Marsh, J, and Kjeldsen, K. No adaptation to digitalization as evaluated by digitalis receptor (Na, K-ATPase) quantification in explanted hearts from donors without heart disease and from digitalized recipients with end-stage heart failure. *The American Journal of Cardiology*, 71 (1):110–114, 1993.

Schmiedeskamp, H, Newbould, R, Pisani, L, Skare, S, Glover, G, Pruessmann, K, and Bammer, R. Improvements in parallel imaging accelerated functional MRI using multiecho echo-planar imaging. *Magn Reson Med*, 63(4):959–969, 2010.

Schwarz, G. Estimating the dimension of a model. *Ann. Statist.*, 6(2):461–464, 1978.

Seth, A. K, Barrett, A. B, and Barnett, L. Granger causality analysis in neuroscience and neuroimaging. *The Journal of Neuroscience*, 35(8):3293–3297, 2015.

Sharief, A. A and Johnson, G. A. Enhanced T_2 contrast for MR histology of the mouse brain. *Magn Reson Med*, 56(4):717–725, 2006.

Shenton, M. E, Dickey, C. C, Frumin, M, and McCarley, R. W. A review of MRI findings in schizophrenia. *Schizophrenia Research*, 49(1):1–52, 2001.

Sheskin, D. J. *Handbook of parametric and nonparametric statistical procedures*. CRC Press, 2003.

Sid, F, Abed-Meraim, K, Harba, R, and Oulebsir-Boumghar, F. Performance bounds analysis in multichannel diffusion-MRI. In *2015 23rd European Signal Processing Conference, EUSIPCO 2015*, 2015.

Sijbers, J and Den Dekker, A. J. Maximum Likelihood Estimation of Signal Amplitude and Noise Variance from MR Data. *Magn Reson Med*, 51(3):586–594, 2004.

Sijbers, J, den Dekker, A, Scheunders, P, and Dyck, D. V. Maximum-likelihood estimation of rician distribution parameters. *IEEE Transactions on Medical Imaging*, 17(3):357–361, 1998.

Sled, J. G, Zijdenbos, A. P, and Evans, A. C. A nonparametric method for automatic correction of intensity nonuniformity in MRI data. *IEEE Transactions on Medical Imaging*, 17(1):87–97, 1998.

Slichter, C. P. *Principles of magnetic resonance*, volume 1. Springer Science & Business Media, 2013.

Smith, H, Janz, T, and Erker, M. Digoxin toxicity presenting as altered mental status in a patient with severe chronic obstructive lung disease. *Heart & lung: the journal of Critical Care*, 21(1):78–80, 1992.

Smith, J, Gheorghiade, M, and Goldstein, S. The current role of digoxin in the treatment of heart failure. *Coronary Artery Disease*, 4(1):16–26, 1993.

Song, Z, Awate, S. P, Licht, D. J, and Gee, J. C. Clinical neonatal brain MRI segmentation using adaptive nonparametric data models and intensity-based Markov priors. In *International Conference on Medical Image Computing and Computer-Assisted Intervention*, pages 883–890, 2007.

Sood, S, Urriola, J, Reutens, D, OBrien, K, Bollmann, S, Barth, M, and Vegh, V. Echo time-dependent quantitative susceptibility mapping contains information on tissue properties. *Magn Reson Med*, 77(5):1946–1958, 2017.

Stanisz, G. J, Wright, G. A, Henkelman, R. M, and Szafer, A. An analytical model of restricted diffusion in bovine optic nerve. *Magn Reson Med*, 37(1):103–111, 1997.

Stanisz, G. J, Odrobina, E. E, Pun, J, Escaravage, M, Graham, S. J, Bronskill, M. J, and Henkelman, R. M. T_1, T_2 relaxation and magnetization transfer in tissue at 3T. *Magn Reson Med*, 54(3):507–512, 2005.

Stejskal, E. O and Tanner, J. E. Spin diffusion measurements: spin echoes in the presence of a time-dependent field gradient. *The journal of chemical physics*, 42(1):288–292, 1965.

Stenger, V. A, Boada, F. E, and Noll, D. C. Three-dimensional tailored RF pulses for the reduction of susceptibility artifacts in T_2^*-weighted functional MRI. *Magn Reson Med*, 44(4):525–531, 2000.

Sukstanskii, A. L and Yablonskiy, D. A. On the role of neuronal magnetic susceptibility and structure symmetry on gradient echo mr signal formation. *Magn Reson Med*, 71(1):345–353, 2014.

Sun, P, Wang, Y, and Lu, J. Sensitivity-enhanced chemical exchange saturation transfer (CEST) MRI with least squares optimization of Carr Purcell Meiboom Gill multi-echo echo planar imaging. *Contrast Media & Molecular Imaging*, 9 (2):177–181, 2014.

Syeda, W, Ng, A, Wright, D, Tolcos, M, and Johnston, L. Analysis of ADC model robustness in diffusion-weighted MRI. In *2017 IEEE 14th International Symposium on Biomedical Imaging (ISBI 2017)*, pages 966–969, April 2017.

Takahashi, T, Wang, F, and Quarles, C. C. Current MRI techniques for the assessment of renal disease. *Current Opinion in Nephrology and Hypertension*, 24(3):217, 2015.

Tasaki, I, Ishii, K, and Ito, H. On the relation between the conduction-rate, the fiber-diameter and the internodal distance of the medullated nerve fiber. *Jpn J Med Sci III, Biophysics*, 9(1):189–99, 1943.

Thomas, J and Cover, M. *Elements of Information Theory*. New York: Wiley, 1991.

Tikhonov, A. N, Goncharsky, A, Stepanov, V, and Yagola, A. G. *Numerical methods for the solution of ill-posed problems*, volume 328. Springer Science & Business Media, 2013.

Torrey, H. C. Bloch equations with diffusion terms. *Physical review*, 104(3):563, 1956.

Trees, H. V. *Detection, Estimation and Modulatin Theory*. New York: Wiley, 1968.

Trees, H. V and Bell, K. Bayesian bounds for parameter estimation and nonlinear filtering/tracking. *AMC*, 10:12, 2007.

Tsang, A, Stobbe, R. W, Asdaghi, N, Hussain, M. S, Bhagat, Y. A, Beaulieu, C, Emery, D, and Butcher, K. S. Relationship between sodium intensity and perfusion deficits in acute ischemic stroke. *Journal of Magnetic Resonance Imaging*, 33(1):41–47, 2011.

Tu, T, Budde, M, Xie, M, Chen, Y, Wang, Q, Quirk, J, and Song, S. Phase-aligned multiple spin-echo averaging: a simple way to improve signal-to-noise ratio of in vivo mouse spinal cord diffusion tensor image. *Magnetic Resonance Imaging*, 32(10):1335–1343, 2014.

Twieg, D. B. The k-trajectory formulation of the NMR imaging process with applications in analysis and synthesis of imaging methods. *Medical Physics*, 10 (5):610–621, 1983.

Van Gelderen, P, De Zwart, J. A, Lee, J, Sati, P, Reich, D. S, and Duyn, J. H. Nonexponential T_2^* decay in white matter. *Magn Reson Med*, 67(1):110–117, 2012.

Veestraeten, D. The conditional probability density function for a reflected brownian motion. *Computational Economics*, 24(2):185–207, 2004.

Wang, J, Lin, W, and Lu, C. Parkinson disease: diagnostic utility of diffusion kurtosis imaging. *Radiology*, 261:210–217, 2011.

Wang, L, Caprihan, A, and Fukushima, E. The narrow-pulse criterion for pulsed-gradient spin-echo diffusion measurements. *Journal of Magnetic Resonance, Series A*, 117(2):209–219, 1995.

Waxman, S. G. Determinants of conduction velocity in myelinated nerve fibers. *Muscle & nerve*, 3(2):141–150, 1980.

Weiskopf, N, Suckling, J, Williams, G, Correia, M. M, Inkster, B, Tait, R, Ooi, C, Bullmore, E. T, and Lutti, A. Quantitative multi-parameter mapping of R_1, PD^*, MT, and R_2^* at 3T: a multi-center validation. *Frontiers in Neuroscience*, 7:95, 2013.

Wenjin, Hall, M, and Laidlaw, D. Inferring microstructural properties using angular double pulsed gradient spin echo NMR in orientationally unknown tissue. In *Computational Diffusion MRI (CDMRI) Workshop at International Conference on Medical Image Computing and Computer-Assisted Intervention - MICCAI*, 2010.

Wheaton, A. J, Borthakur, A, Shapiro, E. M, Regatte, R. R, Akella, S. V, Kneeland, J. B, and Reddy, R. Proteoglycan loss in human knee cartilage: quantitation with sodium MR imagingfeasibility study. *Radiology*, 231(3):900–905, 2004.

Whittall, K. P and MacKay, A. L. Quantitative interpretation of NMR relaxation data. *Journal of Magnetic Resonance (1969)*, 84(1):134 – 152, 1989.

Wink, A. M and Roerdink, J. B. Denoising functional MR images: a comparison of wavelet denoising and Gaussian smoothing. *IEEE Transactions on Medical Imaging*, 23(3):374–387, 2004.

Wood, J. C and Johnson, K. M. Wavelet packet denoising of magnetic resonance images: importance of Rician noise at low SNR. *Magn Reson Med*, 41(3):631–635, 1999.

Wu, B, Li, W, Avram, A. V, Gho, S.-M, and Liu, C. Fast and tissue-optimized mapping of magnetic susceptibility and T_2^* with multi-echo and multi-shot spirals. *NeuroImage*, 59(1):297–305, 2012.

Wu, Z, He, H, Sun, Y, Du, Y, and Zhong, J. High resolution myelin water imaging incorporating local tissue susceptibility analysis. *Magnetic Resonance Imaging*, 42:107–113, 2017.

Xie, L, Dibb, R, Cofer, G. P, Li, W, Nicholls, P. J, Johnson, G. A, and Liu, C. Susceptibility tensor imaging of the kidney and its microstructural underpinnings. *Magn Reson Med*, 73(3):1270–1281, 2015.

Yablonskiy, D, Bretthorst, G, and Ackerman, J. Statistical model for diffusion attenuated MR signal. *Magn Reson Med*, 50(4):664–669, 2003.

Yamada, K, Shinmoto, H, Oshio, K, Ito, S, Kumagai, H, and Kaji, T. Diffusion-weighted MR imaging for the assessment of renal function: Analysis using statistical models based on truncated gaussian and gamma distributions. *Mags Reson Med Sci*, 15(2):237–245, 2016.

Yang, Q, Demeure, R, Dardzinski, B, Arnold, B, and Smith, M. Multiple echo frequency-domain image contrast: Improved signal-to-noise ratio and T_2 (T_2^*) weighting. *Magn Reson Med*, 41(2):423–428, 1999.

Yeh, C and et al., J. T. The effect of finite diffusion gradient pulse duration on fibre orientation estimation in diffusion MRI. *NeuroImage*, 51(2):743–751, 2010.

Zaaraoui, W, Konstandin, S, Audoin, B, Nagel, A. M, Rico, A, Malikova, I, Soulier, E, Viout, P, Confort-Gouny, S, Cozzone, P. J, et al. Distribution of brain sodium accumulation correlates with disability in multiple sclerosis: a cross-sectional ^{23}Na MR imaging study. *Radiology*, 264(3):859–867, 2012.

Zhang, H, Hubbard, P. L, Parker, G. J, and Alexander, D. C. Axon diameter mapping in the presence of orientation dispersion with diffusion MRI. *NeuroImage*, 56(3):1301–1315, 2011.

Zhang, H, Schneider, T, Wheeler-Kingshott, C, and Alexander, D. NODDI: Practical in vivo neurite orientation dispersion and density imaging of the human brain. *NeuroImage*, 61(4):1000–1016, 2012.

Zheng, S and Xia, Y. On the measurement of multi-component T_2 relaxation in cartilage by MR spectroscopy and imaging. *Magnetic Resonance Imaging*, 28 (4):537–545, 2010.